UNIVERSITY OF SOUTHAMPTON

Faculty of Science

Department of Physics and Astronomy

The Development of a CsI(Tl)-photodiode Array for Remote Geochemical Analysis

by

Robert James Evans

A Thesis submitted for the degree of Doctor of Philosophy

June 1999

UNIVERSITY OF SOUTHAMPTON

ABSTRACT

FACULTY OF SCIENCE

PHYSICS

Doctor of Philosophy

A CsI(Tl)-photodiode Array for Remote Geochemical Analysis

By Robert James Evans

To improve our understanding of the mechanism of the formation of the Solar System, information is needed on the global chemical composition of the planets outside of the Earth–Moon system. Thus, the measurement of the chemical composition of Mars and Mercury is a high priority for both the ESA and NASA space programmes. Remote geochemical analysis (RGA), by neutron activation gamma-ray spectroscopy, is a proven technique for remotely mapping the chemical composition of a planet with a thin or no atmosphere and as a result future missions to other terrestrial planets will probably include a gamma-ray spectrometer.

The spectrometer must have sufficient sensitivity to resolve the most important emission lines radiating from the planet, whilst remaining within the mass, power and budget limitations of the mission specification. Therefore, there is a requirement for a spectrometer that will provide sufficient sensitivity, to determine the ratio's of elements such as Fe, O, Si and the naturally occurring radionucides K, U and Th, without incurring the high costs of a cooled HPGe detector.

This work considers the factors that will determine the sensitivity of a scintillator gamma-ray spectrometer for RGA and demonstrates that a 61 element, pixelated, CsI(Tl)-phtodiode array will have a greater sensitivity than an, equivalent mass, NaI(Tl)-PMT or BGO-PMT detector. This is a result of the high mass ratio of sensitive material in the CsI(Tl)-photodiode array and the improved energy resolution, when compared to a NaI(Tl)-PMT detector, at energies above 2MeV. A prototype 7-element array has been designed, constructed and, tested at energies up to 4.44MeV, to demonstrate the potential performance of a larger 61-element array. The energy resolution of the 7 element array was found to be 2.93% FWHM at 4.44MeV, when operating in simple summation mode, which compares to 3.5% FWHM for a 2" NaI(Tl)-PMT detector.

Consideration is also given to the different methods of spectral analysis that may be utilised when using a pixelated CsI(Tl) array and the benefits that may be gained when applying a spectral deconvolution algorithm to the recorded spectra. The process has been used to deconvolve spectra recorded by a small 1cc CsI(Tl)-photodiode detector and the 7-element array. The deconvolution resulted in a pseudo energy resolution for the 1cc detector of 2.3% FWHM at 662keV and a pseudo energy resolution, for the 7 element array, of <2% FWHM at 4.44MeV.

Finally, a large CsI(Tl) array may have the potential to be used for terrestrial applications such as the remote inspection of cargo containers by neutron activation analysis. The design of a potential detector is presented and the performance calculated using Monte-Carlo simulations.

Contents

List of Figures

List of Figures

Acknowledgements

There are many people who have helped, guided and inspired me during the last three years, both on a professional and personal basis, that have made this period very memorable. To all those who I have worked with or known as friends I am grateful for the help which has culminated in the submission of this thesis.

Certain people have had a great influence on my life and hence deserve personal recognition. Firstly to Mum, Dad and Kathryn. You gave me the strength to keep going and the completion of this work would not have been possible without your love and support.

To David I am indebted for all your help, guidance and advise over the last three years. You have a talent for inspiring your students and your influence has changed my outlook on work and life. Thanks to Ian (Sid) and Grant for all the advise and the many hours spent discussing our latest windsurfing and cycling escapades, it certainly helped the time fly by. Also my thanks to Ling-Jian for the interesting discussions and help with the printing and submission of this work.

On a personal level, thank you to Andrew and Jo for all your support and friendship. The many weekends spent at Alton certainly helped me relax and forget about work for a while. Also thanks to Iain for the many evenings spent discussing the state of Welsh rugby. I am sure we will have many more!

Finally, I wish to thank my sponsors AEA Technology for their financial support during my period of study.

Chapter 1

1 The Formation of the Solar System

1.1 Introduction

For over 200 years, scientists and philosophers have tried to explain the origins of the Solar system and the mechanisms involved in its formation. In the last 100 years, studies of the motions of the planets, the geological processes occurring on Earth and the analysis of meteoritic material from Mars and the asteroid belt, have increased the volume of information available by several orders of magnitude. Yet there is no more certainty about the formation mechanism than there was a century ago. Part of the reason for this uncertainty may be the lack of observational data from extra-terrestrial planets such as Mars, Mercury and the asteroids. Several attempts have been made to map the chemical composition of Mars but unfortunately, all have ended in failure. Thus there is insufficient data to constrain the boundaries within which the formation of the inner planets must have taken place and, as a result, no theory can be categorically proven or refuted. Measurement of the chemical composition of Mars and Mercury is a high priority in the future for both the ESA and NASA space programmes, which should provide a wealth of information for planetary scientists to work with. This chapter aims to explain the three most popular theories proposed to explain the formation of the solar system and to discuss the observations that led to these conclusions. The chapter also aims to demonstrate how future missions to Mars and Mercury may provide the information required to formulate a solid theory for the formation of the Solar system [1][2].

1.2 The Popular Theories for the Evolution of the Inner Planets

In 1796, Laplace proposed his nebular hypothesis [3] which, by the end of the 19th century, had been widely accepted by many astronomers. However, there are several observations that cannot be explained by the nebula hypothesis such as the chemical composition of the giant gaseous planets. Furthermore, the mass of the proto-planetary disk would have to have had a mass similar to that of the Sun, which is considered unlikely, and the model does not account for the creation of asteroids, comets and moons [4]. In the last fifty years, there have been several favoured theories for the formation of the solar system. The reason there has not been a single coherent theory is probably due to two factors. Firstly, scientists have been working with limited information on the composition of non-terrestrial planets. The material that has been available for analysis has been brought to Earth by meteorites and therefore is of uncertain origin and history, which makes the analysis difficult and often inconclusive. The second reason for the changes in consensus is due to the lack of information regarding other solar systems against which to compare the theories. At present the only well observed planetary system is our own, although several Jovian-sized planets have been deduced from radial velocity observations of several nearby stars such as 51Peg, 47UMa, 70Vir [5], 16 Cygni B [6] and ρ Coronae Borealis [7]. Thus there are no other systems to test theories against and hence it is difficult to prove or disprove any one theory.

If the solar system is assumed to be a random sample from all the solar systems of the universe, then it should be possible to construct a model for planetary formation, that will predict the formation of a range of planetary systems including our own. Part of the problem may be that our solar system is not a random sample from the universe, but is a sample that will support living organisms that are able to ponder the question on the mechanism of the formation of the planets. Therefore the question still remains, “Would all solar systems form in the same way as our own?” Indeed, if our Solar system is an unusual one, there may be any number of explanations or theories that might explain the current properties of the system and we may never be certain of its history [8]. However, assuming that our solar system is the product of natural evolution, it must be possible to use our knowledge of the laws of physics and information from extraterrestrial objects, to place constraints on the formation mechanism of the solar system. A complete theory of the origin of the solar system must be able to explain facts such as the orbital motions, spacing, rotation, mass, bulk composition and isotopic composition of the planets [9]. In addition, it must also explain the presence and composition of satellites, comets and the asteroid belt. A model that succeeds in explaining all these observations must also be able to account for the solar system formation within a realistic time scale.

Over the last 50 years, scientific opinion has varied between a hot gas condensation and a cold accretion model for the formation of the solar system, with occasional regard to the dualistic approach of an interfering, passing star. Questions that remain uncertain include the mass of the pre-solar nebula; how the angular momentum was transferred from the Sun to the giant planets; how the giant gaseous planets formed and what was the temperature and mechanism for the condensation of the terrestrial planets [10]. The three principal contending theories for the formation of the solar system are described below. To date no conclusive evidence has been produced to support or refute any of the theories and the experience of the last 50 years has shown that the favoured theory may change.

1.2.1 Condensation of Hot Gases

According to the nebula hypothesis, the atmosphere of the Sun once extended throughout the space now occupied by the planetary orbits. It was a hot luminous, rotating cloud of gas, which contracted as it cooled so, to conserve angular momentum, the disk was required to spin more rapidly. The hypothesis treats the gas as a rigid body so the linear velocity would be greatest at the periphery. Eventually, the centrifugal force would overcome the gravitational force and the outer ring of gas would split away from the main body as the gas continued to contract. These rings of gas then formed giant gaseous protoplanets, via instabilities in the gas disk, in a manner analogous to star formation [10].

In the early 1960's evidence was presented that supported a high temperature stage in the theory of the formation of the terrestrial planets [11]. Measurements were made of the concentration of the volatile alkali metals in meteoritic chrondrules and compared to those of the Earth's crust. The measurements found that the Earth's crust is depleted in alkali metals compared to the meteoritic material. Accepting the theory that meteoritic chrondrules, are direct condensates from the solar nebula [12], then the Earth's mantle is depleted in alkali metals compared with the solar nebula, which suggests that some evaporation of the volatile metals had occurred during the Earth's formation [13]. Recently, the high temperature model has fallen out of favour for several reasons [4]. The principal objection is that all of the planets are substantially enhanced in dense material relative to the solar composition. Originally this was explained by stripping of the atmosphere after the formation of the protoplanetary core. However, this is very difficult to explain for Uranus and Neptune, which are a long way from the solar energy source and have H_2 and He abundance's <1% of hypothetical solar composition bodies with the same mass of high Z elements [14]. Other objections included that the separation of a heavy core and lighter gases would not occur prior to the atmosphere stripping. The mass of the gas disk would also have had to be equivalent to the mass of the Sun and the model cannot account for asteroids, comets, moons and other small bodies [15].

1.2.2 A Supernova Trigger

The lack of consensus for a theory on the method of formation of the solar system over the last 50 years has lead some scientists to hypothesise that the solar system was not created by the natural evolution of a dust or gas cloud. By the mid 1970's, several isotopic anomalies had been observed in meteorites which could not be explained by the popular theories. In 1976 Sabu and Manuel [16] proposed that the early Sun had formed a binary system with another star that exploded, irradiating the solar system and resulting in the material, which later formed the accompanying planets. In 1977, Cameron and Trurnan [17] proposed that a supernova had injected radioactivities in to a nearby interstellar cloud and possibly also caused the cloud to collapse thus resulting in new stars and planets. The claims that the Solar System was born from a supernova explosion were backed up by observations of supernova-induced star formation in Canis Major [18].

The supernova trigger theory gained huge support in the scientific press and throughout the scientific community and until 1984 it was widely believed that one or more supernova were responsible for the formation of the solar system. However, one of the crucial assumptions of most of the models was that the ^{26}Al, that decayed into the ^{26}Mg found in the Allende meteorite, must have been synthesised by the explosion of a Supernova. In the early 1980's several scientists questioned whether a supernova was the only explanation for the excess of ^{26}Al and several alternative explanations were put forward. The work of the scientists questioning the supernova trigger theory was given huge support when the High Energy Astronomical Observatory satellite (HEAO-3) revealed that large amounts of ^{26}Al were present throughout the galaxy [19]. This led to the conclusion that, the amount of ^{26}Al could not be synthesised only by a supernova and the concentration of ^{26}Al, inferred from the Allende meteorite, was the average interstellar value at the time [20]. Thus the supernova trigger theory had been seriously undermined and gradually lost popularity with the planetary science community.

1.2.3 Accretion of Small Particles

T.C.Chamberlin, first proposed the accretion of small particles as a method for planetary formation, in 1905 [21]. However, the theory was later disregarded due to doubts regarding whether dust or molecules could condense to visible grains or chrondulites from which the planets could form [22]. In the late 1950's, Nobel Prize winner, Harold Urey became interested in the formation of the Earth. He concentrated on trying to explain the chemical composition of meteorites and the presence of volatile elements in the Earth's surface. He came to the conclusion that the Earth could not have been formed at temperatures above 1200K due to the presence of iron sulphide and silicates mixed with the metallic iron phase. These compounds would be unstable in the presence of cosmic proportions of hydrogen above 600K and yet both are present in meteorites. However, diamonds are also found in meteorites and presumably cannot be formed without high temperature and pressure. It was therefore proposed that chrondritic matter is a mixture of two kinds of material of widely different chemical histories [23]. The cold accretion theory lost popularity in the early 1960's in favour of a high temperature model and then later the supernova trigger hypothesis. After 1984, when doubts were placed on the evidence for a supernova trigger, revised versions of the cold accretion or planetessimal hypothesis were revived, which tried to explain the presence of both iron sulphide and diamonds next to each other in meteorites.

The modern theory of cold accretion envisages the process of planetary growth generally being divided up into phases [8]. In the first stage, microscopic grains, which have condensed out of the gas disk, collide and grow via two body collisions until they are approximately 1km in diameter. Once the solid bodies have reached kilometre size, gravitational interactions between planetessimals dominate. The subsequent accumulation of the resulting protoplanets leads to a large degree of radial mixing in the terrestrial planet region and giant impacts are possible. It is this radial mixing that is assumed to give rise to the early solar system material consisting of materials from obviously different temperature backgrounds. This process has been treated in detail and it has been found that once the planetessimals have reached a diameter of approximately 1km, run-away growth occurs up to bodies in the size range of the moon and Mars. Growth of the planetessimals continues until the protoplanets become dynamically isolated from each other. Some planetessimals are never incorporated into planets and remain as asteroids and comets. If a planet becomes sufficiently massive, it may gravitationally accumulate substantial amounts of H_2 and He and form a gaseous giant planet such as Jupiter and Saturn.

However, the planetessimal theory is by no means complete. The process by which, very small planetessimals accumulate by two body interactions, is not well defined [8][24][25]. The principal problem is that, if planets formed from planetessimals, the process must have occurred over a wide range of thermal, physical and chemical conditions, especially if the satellite systems in the outer solar system are considered to be miniature planetary systems. To date, no theory or simulation has been able to demonstrate this mechanism of planetessimal coagulation, in anything but the most favourable conditions.

1.2.4 Future Observations

At present, the favoured model for the formation of the solar system is the cold accretion of planetessimals. However, as stated, the exact mechanism for this process is still not fully understood and more information is required in order to form a more complete theory. A key element in the arguments to determine the most likely model for the formation of the Solar System, is the temperature at which planetary formation took place. This question may be answered by an accurate determination of the chemical composition of Solar System bodies at varying distances from the Sun. Geochemical clues to the evolution of a planet include the supply of sulphur and metallic iron (the formation of FeS), the ratio of FeO/MnO (the oxidation of iron), the ratio of Tl/U (re-melting of the primordial condensates) and the ratio K/U (relative abundance of volatiles). Since many elements can be grouped according to their condensation and geochemical behaviour, chemical abundance data for only a few key elements are needed to determine the origin and evolution of a planet [26]. Therefore, if the chemical compositions of planetary bodies such as Mercury, Mars and the asteroids were known and combined with our current knowledge of the composition of the Earth and the Moon, a temperature profile for the inner Solar system, at the time of planetary formation, may be deduced.

Once the temperature of the inner Solar system is constrained, then it may be possible to deduce a comprehensive theory for the condensation and accretion of planetessimals to form the protoplanets. Also measuring the chemical composition of the inner Solar System would provide information of the ratio of the light to heavy elements and the variation in the naturally occurring radionuclides at the time of condensation and planetary formation. Thus, the examination of other Solar System bodies, such as meteors and comets, could result in a more accurate estimate for the time and place at which they were formed.

1.3 Observation of Mercury and Mars

Knowledge about the planet Mercury is incomplete and less is known about Mercury than any other terrestrial planet. Mercury is an end-member of the terrestrial planets in respect to its mass, density and heliocentric distance from the Sun and consequently is an important target of planetary research. The limited exploration of Mercury by the Mariner 10 spacecraft [27] has generated questions about its origin and hence the origin and evolution of all the terrestrial planets. A better understanding of Mercury, and its environment, is important in its own right but it also holds the key, through comparative studies, to several aspects of the formation, history, morphology and current geochemical and geophysical states of the other terrestrial planets [28]. To approach basic scientific questions on the origin and evolution of Mercury, data on its chemical composition is required [29]. Remote geochemical analysis by gamma-ray spectroscopy is the most effective method for determining the chemical composition of the crust of a planet and therefore could provide a significant contribution to understanding the formation of the Mercury and hence, the inner planets of the Solar System.

Mercury's diameter is 4878km and the planet has a mass of 3.301×10^{23}kg, which is 0.055 times that of the Earth. Thus it has a very high mean density of 5.44g/cm^3, second only to that of the Earth (5.52g/cm^3). Mercury is covered with a regolith consisting of fragmental material derived from the impact of meteoroids over billions of years and like the moon, it's surface is heavily cratered with smooth plains filling and surrounding large impact basins. The origin of Mercury and how it acquired such a large fraction of iron compared to the other terrestrial planets is not well determined. Recent models of the chemical equilibrium condensation for Mercury only yield a mean density of about 4.2g/cm^3 [30]. Furthermore, if Mercury formed entirely from objects originating from its present distance from the Sun, then there should be an almost complete absence of sulphur and other volatile elements, such as water, should be severely depleted [31].

Three hypotheses have been put forward to explain the difference between the predicted and the observed iron abundance on Mercury. Selective accretion involves the enrichment of iron due to mechanical and dynamical accretion processes whilst the other two (post accretion vaporisation and giant-impact) invoke the removal of a large fraction of the silicate mantle from a once large proto-Mercury. Discrimination between these models is difficult but may be possible from the chemical composition of the silicate mantle [32]. If the selective accretion model is correct, Mercury's silicate portion should contain 3.6 to 4.5% alumina, 1% alkali oxides and between 0.5 and 6% FeO. The post-accretion vaporisation model should lead to a very severe depletion of alkali oxides and FeO with an enrichment of refractory oxides (≈ 40%). If a giant impact stripped away the crust, then alkali oxides may be depleted (0.01 to 0.1%) with refractory oxides between 0.1 and 1% and FeO between 0.5 and 6%. Deciding between these models is not possible with our current knowledge about the chemical composition of Mercury. A Mercury orbiting spacecraft, equipped with a gamma-ray spectrometer could provide the data required to solve these problems.

There have been several successful missions to Mars, both orbiters and landers, resulting in detailed maps of the surface and a good understanding of the nature of the planet [33]. Unfortunately, there have been no successful missions carrying a gamma-ray spectrometer due to the failure of the US Mars Observer mission and the Russian Phobos and Mars 96 missions. Thus the overall chemical composition of Mars is still unknown and some vital questions, such as the ratio of K:U, remain unanswered.

Uranium provides an index for elements that are condensed from the solar nebular at high temperatures whilst potassium is an index for elements with lower condensation temperatures. Therefore the ratio of K/U coupled with other elemental ratios, provides a means of reconstructing the bulk composition of the planet. The content of these two elements in the crust also gives an indication of the degree of differentiation of the planet, estimates of the amount of volatiles that have outgassed from the planet and places constraints on thermal evolution models [34]. Other major questions that still need to be answered are the cause of the planet dichotomy into old cratered uplands and sparsely cratered plains. Determining the chemical composition of these regions could lead to a better understanding of the dichotomy, what caused it and when it occurred.

Remote geochemical analysis by gamma-ray spectrometry of both Mercury and Mars will provide information that could lead to a better understanding of the processes that lead to the formation of the inner planets of the Solar System. Missions to both these planets are being planned by ESA and NASA and hopefully, if gamma-ray spectrometers are included in the payload, will result in a chemical map of both planets.

1.4 The Origin of the Moon

In modern times there have been four theories to explain the origin of the moon. Capture theories assumed the moon was formed elsewhere in the solar system and later captured into orbit around the Earth. It was originally proposed at the start of the 20th century and was later revived in the 1960's [35]. This theory is no longer considered seriously due to the dynamical improbability of the Moon being captured by the Earth, even if it formed at the same heliocentric distance from the Sun. The co-accretion theory postulated that the Moon and the Earth formed at the same time, from the same disk of material [36]. However, this theory cannot explain the angular momentum of the Earth-Moon system. The fission theory claimed the moon was once part of the Earth but as it was forming, became unstable and as a result the moon separated from The Earth to become a separate body [37]. Again this theory is no longer considered to be viable due to dynamical calculations, which show that the proto-Earth could not be spun fast enough to cause fission to occur. Currently, the most popular theory is the giant impact theory, which was originally proposed in the mid-1970's. The theory postulates that a Mars sized planet impacted with the young Earth, resulting in the Moon being a mixture of the material from the Earth and the impacting planet [38].

The Apollo missions of the late 1960's, early 1970's, returned a wealth of data and samples from the lunar surface. The data was confined to the equatorial regions of the Moon but still enabled scientists to confirm that the mantle of the moon is “similar” to that of the Earth [39]. In 1998 NASA launched its first lunar mission for 25 years. The Lunar Prospector aims to map the bulk chemical composition of the Moon to help answer the question of its origin. For example, there have been suggestions from Apollo, Galileo and Clementine data that the Moon is enriched in refractory elements (Al, U and Th) and FeO compared to Earth. If so, then any lunar origin model that assumes that most of the moon's material came from the Earth's mantle would not be correct [40]. The Lunar Prospector will also study the variability of the lunar highlands, which in turn could give information about how the lunar crust evolved, the basaltic units in the maria and the composition of the ancient mare units found in the highlands.

1.5 The Technique of Remote Geochemical Analysis

The planetary bodies of the Solar System are constantly being bombarded by a high energy, cosmic ray flux. The principal sources of this flux are intergalactic cosmic rays (GCR's) and solar cosmic rays (SCR's), which can reach the surface of planets having little or no atmosphere, producing a cascade of secondary particles including neutrons. The neutron cascade, produced by the cosmic-rays, interact with the surface of the planet by inelastic scattering and capture reactions, resulting in excited nuclei, which decay with the emission of characteristic gamma-rays as illustrated in Figure 1.1.

Also contained within the surface of the planets are quantities of natural radionucleides, which decay with the emission of a gamma-ray. Natural radioactivity results from the decay of ^{40}K and the radioactive daughters of Thorium and Uranium. Important examples are the 1.46 MeV line emitted in the decay of ^{40}K to ^{40}Ar and the 2.62 Mev line of ^{208}Tl, a daughter of ^{232}Th [26]. Potassium is a relatively volatile element whilst Uranium and Thallium are refractory materials thus the temperature at which condensation would occur is vastly different. Thus the relative intensity of these natural isotopes such as potassium and uranium is particularly useful when trying to determine the temperature at which the planet formed and condensed.

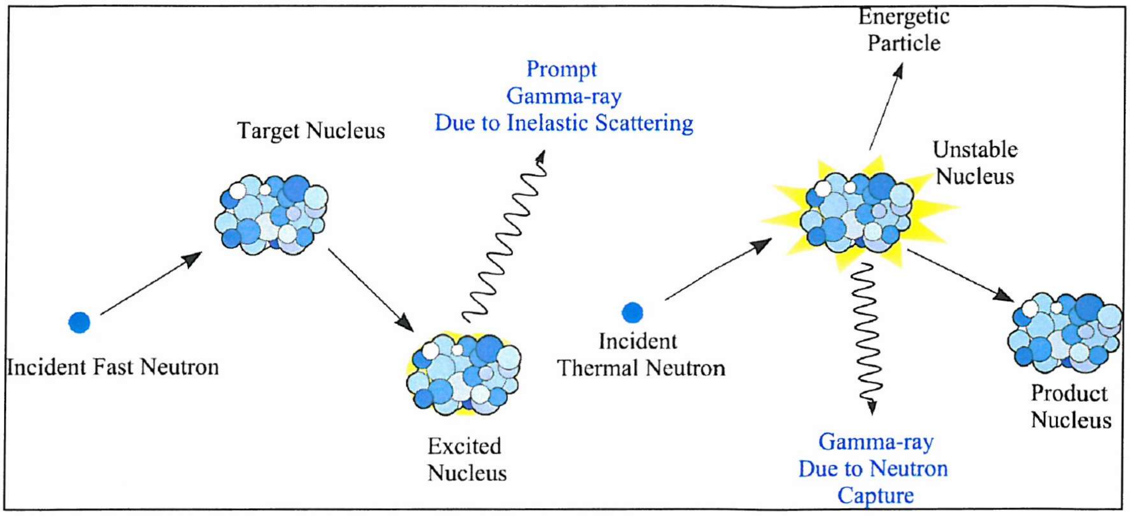

Figure 1.1 Illustration of the neutron capture and inelastic scattering process

The gamma-ray spectrum emerging from the surface of the planet is complex and consists of many gamma-ray lines superimposed on a continuum. The continuum is the result of gamma-rays that have Compton-scattered before emerging from the surface and the many lines represent the many elements present in the surface, some of which have more than one de-excitation mechanism. Despite the complexity of the spectrum, it still contains the quantitative and qualitative information, from which the chemical composition of the planets surface may be calculated.

The complex gamma-ray spectrum emerging from the surface of the planet spans the energy range from 0.1 to 10 MeV. Therefore a gamma-ray spectrometer mounted on an orbiting spacecraft must have a good stopping efficiency and a fine energy-resolution, over a large energy range, in order to resolve the individual gamma-ray emission lines. Natural radio nuclides such as K, U and Th emit gamma-rays below 2.5 MeV whilst activated elements such as oxygen and iron emit gamma rays in the region of 6 to 8 MeV. Accurately recording the relative intensities of both sets of lines is important when trying to determine the conditions at the point of formation of a planet. The successful Apollo 15 and 16 missions of the early 1970's used a NaI(Tl) crystal connected to a photomultiplier tube (PMT), to record the gamma-ray spectrum, from which 22% of the lunar surface was chemically mapped. Other detectors, which may now be considered, for this task include a cooled, high-purity germanium detector (HPGe), a BGO-PMT detector or a CsI(Tl)-photodiode array. Each type of detector has advantages when designing such a spectrometer for remote geochemical analysis, considerations include, energy resolution, stopping efficiency, mass of sensitive medium, mass of the complete detector, cost, development time and previous space-borne history.

1.6 Conclusions

By understanding the surface composition of a planetary body, particularly the ratio of volatile to refractory elements, it is possible to infer the overall composition and hence the likely temperature and mechanism of formation. Knowing these parameters for Mercury, the Earth and Mars, it may then be possible to conclude what mechanism resulted in the formation of the terrestrial planets. In addition, knowledge of the changes in chemical composition across a planetary surface may provide valuable information from which the geological history of the planet may be derived.

Remote geochemical analysis by neutron activation spectroscopy is a tested method by which the chemical composition of the surface of a planet may be measured globally. However, due to the many elements present in the surface of a planet, the emergent gamma ray spectrum is complex, consisting of many gamma ray emission lines superimposed on a continuum. The challenge is to design a spectrometer that is sufficiently sensitive, over a 10 MeV range, to allow the reconstruction of the radiating flux from relatively short observations of the planet. The following chapters present a review of previous work, on the designs and performance of gamma ray spectrometers, for remote planetary geochemistry and a detailed study of a new design of spectrometer that could provide a greater sensitivity than any other equivalent-mass scintillator spectrometer.

Chapter 2

2 Review of Past, Present and Future Missions

2.1 Introduction

To date, there have only been three successful missions to map the surface chemistry of another planet. The first two successful missions were Apollo 15 and 16 in 1971 and 1972, which mapped approximately 22% of the Lunar surface from equatorial orbits around the Moon [41]. Following these successes there then followed three unsuccessful attempts to map the surface chemical composition of Mars. In 1989 the Russian Phobos mission carrying a large CsI(Tl) scintillator coupled to a photomultiplier, failed after acquiring only limited data from the planet [42]. Then in 1993, the US launched the Mars Observer, carrying a cooled high purity germanium spectrometer (HPGe) [2]. The instrument performed to expectations during the cruise phase, but failed to map the elemental composition of Mars due to lost communication with the spacecraft just three days into Mars insertion orbit in August 1993. The most recent attempt to map the surface of Mars was the Russian Mars 96 mission. The spacecraft had several gamma-ray spectrometers (GRS's) onboard, including two CsI(Tl) scintillators, one surrounded by BGO, the other unshielded. Also included were two germanium detectors with passive cooling. [43]. The spacecraft crashed in the Pacific, soon after launch in November 1996. The third successful mission to date is the Lunar Prospector, which was launched in September 1997 and is currently in a polar orbit around the moon mapping the chemical composition of the entire planet. The Lunar Prospector gamma-ray spectrometer is a cooled BGO crystal with a large plastic anti-coincidence shield, both of which are coupled to photomultiplier tubes

[44]. Currently there is one other spacecraft in operation that is destined to perform planetary geochemistry, this is the Near Earth Asteroid Rendezvous (NEAR). This spacecraft was launched in February 1996 and will rendezvous with asteroid Eros in 1999. The GRS is a NaI(Tl)-photomultiplier detector, surrounded by a large BGO scintillation shield. Preliminary cruise phase tests have been performed with the spectrometer and there appear to be no problems [12].

2.2 Remote Geochemical Analysis of The Moon

The Apollo Gamma-ray Spectrometers

The Apollo gamma-ray spectrometers were the first successful missions to map the geochemistry of another planet and for 27 years were the only successful missions. Therefore the Apollo detectors have provided a benchmark against which any future detector may be compared. The gamma-ray spectrometers, flown on the Apollo 15 and 16 missions, were designed to measure gamma-ray energies in the range from 0.2 to 9MeV and consisted of ruggedised 7.0cm by 7.0 ϕ cm NaI(Tl) scintillator crystals, which were hermetically sealed in stainless steel containers and coupled to PMT's. To avoid crystal fracture or reflector displacement during the launch environment, bevel springs were used to preload the crystal with a force of 30kg. Powdered MgO served as a reflector and provided thermal and shock damping for the crystal. A 0.5cm thick boro-silicate glass optical window covered the crystal. Silicone grease was used to couple the crystal to the PMT, which had a nominal operating voltage of 850V.

To eliminate events due to charged particles a 0.8cm thick plastic scintillator surrounded the NaI(Tl) on all sides except the crystal-PMT interface. The plastic shield was connected to a 1.5" diameter PMT with an operating voltage of 1650V to maximise the sensitivity of the shield. Charged particles, which deposited more than 0.7MeV in the plastic were detected but the shield had a low interaction probability to gamma-rays. Coincident events from the plastic shield and the NaI(Tl) scintillator were rejected. To further reduce the background, due to charged particles and gamma-background from the spacecraft, the spectrometer was mounted on a 2m long boom. Mechanically the detector was divided into 3 parts: the Gamma-ray Detector (GRD), the Gamma-ray Electronics (GRE) and the thermal shields and support ring. The GRD weighed 3.3kg, the GRE 3.2kg and the entire instrument weighed 9.7kg. The total dimensions of the instrument were 48.0cm long by 24.8cm in diameter [45]. A diagram of the spectrometer is shown in and the performance of the spectrometers is summarised in Table 2.1.

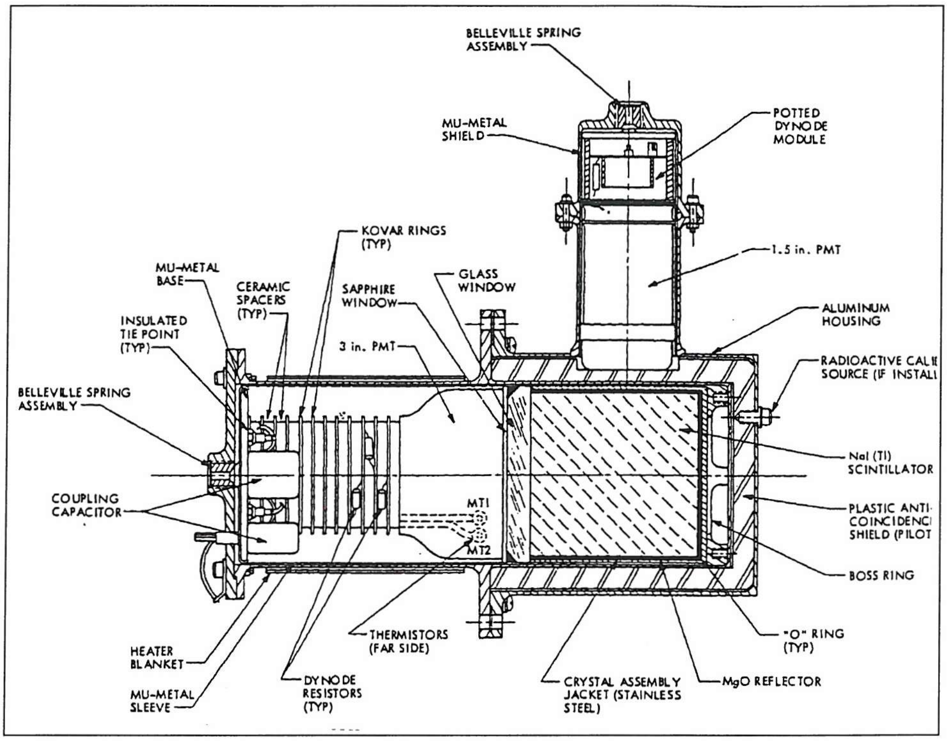

Figure 2.1 The Apollo gamma-ray spectrometer

	Apollo 15	Apollo16
Ground resolution at 0.66MeV	8.6%	7.5%
Ground resolution at 2.61MeV	4.5%	4.0%
Flight resolution at 2.61MeV	4.7%	4.2%

Table 2.1 The energy resolution of the Apollo 15 and Apollo 16 GRS

A total of 135 hours of observational data was taken, using the NaI(Tl) scintillation spectrometers, from which, the chemical composition of approximately 22% of the equatorial Lunar surface was mapped [48], the Apollo gamma-ray spectrometers provided no information regarding the surface chemistry of the lunar poles. Due to the limited energy resolution of the spectrometer and the relatively short lifetime of the mission, deconvolution of the complicated, lunar energy-loss spectrum, required sophisticated data deconvolution techniques and comparisons with ground truth data [41]. The spatial resolution of the Lunar mapping depended on the field of view, the time of observation, the intensity of response of a given element and the contrast with the surrounding area.

The Apollo GRS's were ground breaking experiments which, until the Lunar Prospector mission, were the only missions to provide real data, on the chemical composition of another planetary body, by the technique of remote planetary gamma-ray spectroscopy. However, the observation time was limited to 135 hours, which was spread over 22% of the equatorial lunar surface. Therefore the spatial resolution of the chemical composition map was limited by the statistical quality of the spectra and advanced data deconvolution techniques were applied to the data to resolve the major components of the spectrum. The lunar landings provided samples from selected regions of the Moon, which complemented the remote geochemical analysis of the lunar surface by the orbiting modules. Subsequent analysis of the returned samples provided valuable information for the calibration of the deconvolution techniques and increased the confidence in the lunar chemical composition map.

The model on which the data analysis was based was that of Reedy, Arnold and Trombka [41] and is discussed in detail in chapter 5. The initial results, from the analysis, were concentration maps for the elements Th, K, Fe, Mg and Ti, in 28 regions overflown by the Apollo 15 and 16 spacecraft [46]. Subsequently, more detailed analyses [47] and analyses using different methods of data deconvolution [48] were carried out and the results are also discussed in chapter 5.

The Lunar Prospector Gamma-ray Spectrometer

On 7th January 1998 NASA launched its first lunar mission for 25 years, The Lunar Prospector. The spacecraft was placed in orbit around the moon on the 16th January 1998 and is expected to end in July 1999 when the LP impacts on the Moon [49]. The Lunar

Prospector is a competitively selected mission in NASA's Discovery program. The primary goal of the mission is to obtain scientific data about the structure, composition and resources of the Moon. This will provide an insight into the lunar origin, evolution and the prospects for exploration. The LP was a very low cost spacecraft with minimal operational requirements. The instruments were chosen on the basis of :

- High science value
- Low data rate
- Small mass
- Low power requirement
- Omnidirectional field of view
- Proven capability based on heritage from previous missions

A BGO-PMT gamma-ray spectrometer was chosen to map the composition of the lunar surface. BGO-PMT detectors are not expensive, can be assembled into the spacecraft payload in a similar manner to the Apollo spectrometer and provide an improvement on the performance of the Apollo detector if the temperature of the BGO is kept below -28°C. Initial results have been presented on the elemental distribution of thorium and potassium plus limited information on the distribution of iron. However, the detailed detector modelling and spectral fitting procedures required to convert the gamma-ray spectra into absolute elemental abundance for all elements has not yet been carried out [50].

The Lunar Prospector will almost certainly provide a detailed chemical map of the Moon, with coverage of almost the entire surface, especially the poles. However, the selection of the Lunar Prospector GRS was almost certainly based on financial driving factors and the simplicity of acquiring and testing a BGO-PMT spectrometer. It therefore probably does not represent the optimum scintillator detector that may be used for this type of mission. The following chapters aim to demonstrate the benefits that may be achieved using a CsI(Tl)-photodiode array for remote geochemical analysis with no considerable increase in the cost of the detector.

2.3 Geochemical analysis of Mercury, Mars and Asteroids

The NEAR Gamma-ray Spectrometer.

The previous chapter has explained that modern models for the formation of the Solar System, favour the formation of the planets from planetessimals, which aggregated from the material that condensed from the solar nebular. Most of the primitive planetessimal material has now combined to form the planets, some however still remains intact and in a fragmented state in the form of the asteroids [8]. Asteroids are thought of as primitive remnants of the bodies from which the planets formed. However, the degree to which they have evolved from unaltered nebular condensates, varies greatly, ranging from CI carbonaceous chondrites, which closely match solar nebular elemental ratios, to highly differentiated bodies with basaltic crusts. Main belt asteroids are not readily accessible to study by spacecraft, but some asteroids lie in more accessible Earth-approaching or Earth-crossing orbits and are called Near Earth Asteroids (NEA's). The asteroid Eros is one such object and will be studied by the Near Earth Asteroid Rendezvous spacecraft (NEAR) in 1999. The composition of Eros is unclear and the mission aims to provide the answers to questions such as the relationship Eros has to known meteor types, whether the body is chemically primitive or differentiated, the important geological processes in its evolution and if it is a fragment of a larger body or an aggregate of fragments from one or more parent bodies.

NEAR was launched in February 17th, 1996 as one of the first of NASA's Discovery missions under the slogan "better, faster, cheaper" and a total budget of $150M. The mission was the first discovery mission to be launched and was chosen due to high priority objectives set by the science community [51]. NEAR will orbit the asteroid for approximately one year from February 1999 to February 2000, at a minimum altitude of 15km. The aim of the mission is to make the first comprehensive scientific measurements of an asteroids surface composition, geology, physical properties, and internal structure Onboard the spacecraft are 6 instruments including an X-ray/gamma-ray spectrometer for mapping the global chemical composition of the asteroids in the top 10 to 20cm from the surface [52]. Gamma-ray emissions in the energy range from 0.1 to 10MeV will be used to measure the cosmic-ray excited elements O, Si, Fe, H and the naturally radioactive elements K, Th and U.

Restrictions on mass, cost and mission duration precluded the use of a cryogenically cooled Ge detector such as that used on the Mars Observer mission. The gamma-ray spectrometer consists of a NaI(Tl) scintillator situated within a thick bismuth germanate cup (BGO). The BGO cup is an active scintillator and thus is used to reduce the Compton and pair production contributions to the spectrum, as well as providing passive shielding from the locally induced gamma environment. Coincidence techniques may be applied that allow the recovery of single and double escape events from the central detector, this technique is discussed further in chapter 4. The design eliminated the need for a massive and costly boom, allowing the instrument to be mounted to the body of the spacecraft. Figure 2.2 shows an outline of the detector assembly and the detector cross-section. EMR Photoelectric, a division of Schlumberger designed the gamma-ray detector, and the central rugged NaI(Tl) unit is based on those used for oil logging operations. The NaI(Tl) detector is a 2.54cm × 7.62cm right circular cylinder coupled to a 3.17cm PMT. The BGO crystal has an outer diameter of 8.9cm × 14cm and is coupled to a 7.6cm diameter PMT. The mass of the detector is 6kg, over 90% of which is accounted for by the BGO shield. The NaI(Tl) and BGO detectors achieve an energy resolution of 8.7% and 14% FWHM at 0.662MeV respectively and have a full energy range of 0.1 to 10MeV [53].

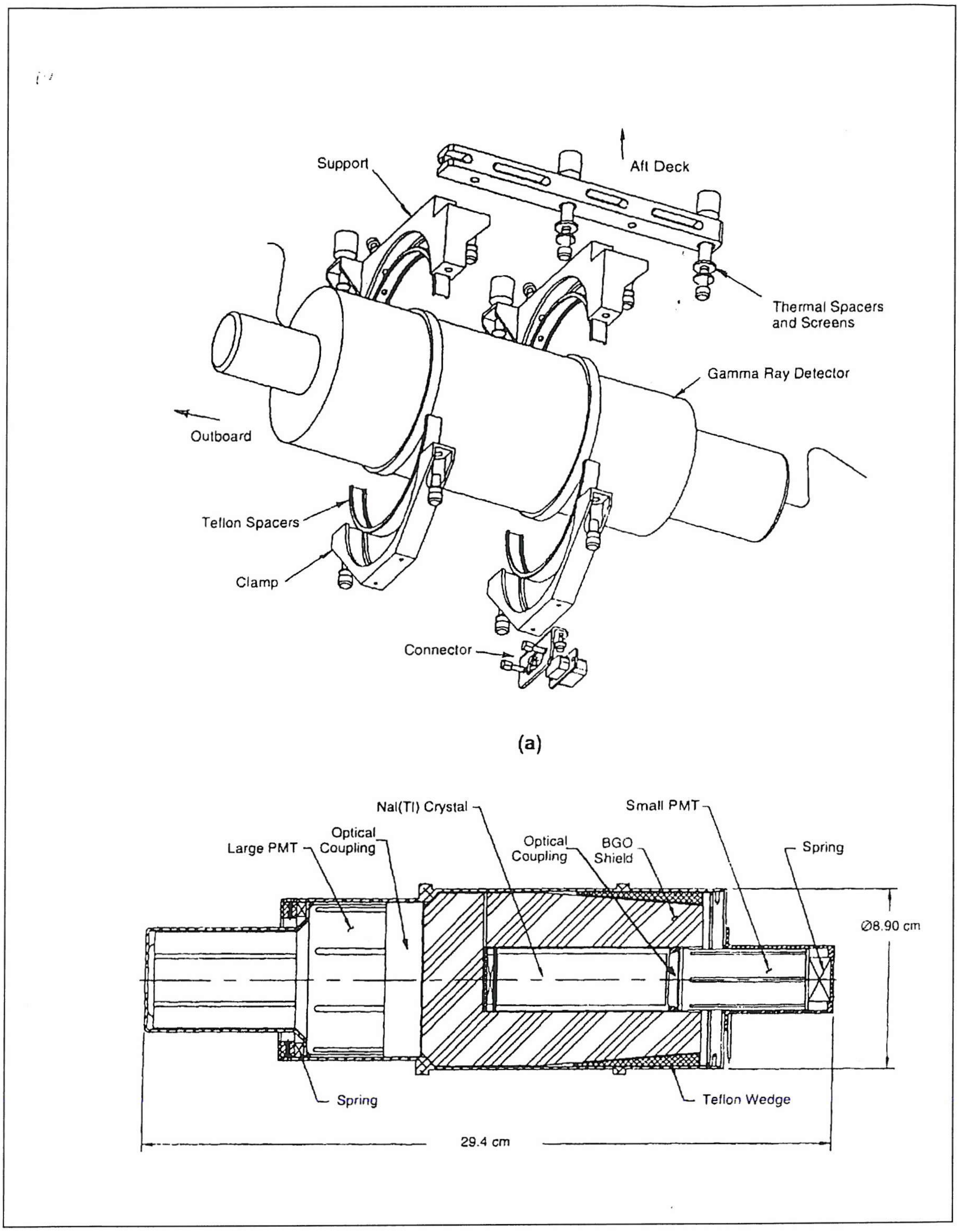

Figure 2.2 The NEAR GRS

During the cruise phase of the mission, many days of BGO and NaI(Tl) background spectra, have been obtained. The BGO background spectra have enabled the identification of several emission lines such as the 0.511MeV positron annihilation line, 0.844MeV from

Al^{27}, 1.809MeV from Mg^{26}, 2.223MeV from hydrogen, 4.438MeV from oxygen and 6.129MeV from oxygen. Four NaI(Tl) calibration spectra from a $Pu^{13}C$ source are shown in Figure 2.3. The four spectra are the raw spectrum, in anti-coincidence with BGO, in coincidence with the 0.511MeV line in the BGO and in coincidence with the 1.022MeV in the BGO. It may be seen that partial energy-loss events and the escape peaks from the 6.129 MeV emission line dominate the raw spectrum. The anti-coincidence spectrum shows a dramatic reduction in the partial energy-loss events due to the BGO shield being comparatively thick and hence detecting most secondary photons. It may be noted that the 0.511keV coincidence spectrum removes the second escape peak from the 6.129MeV line and the 1.022keV coincidence spectrum removes both the first and second escape peaks, in addition to the Compton continuum.

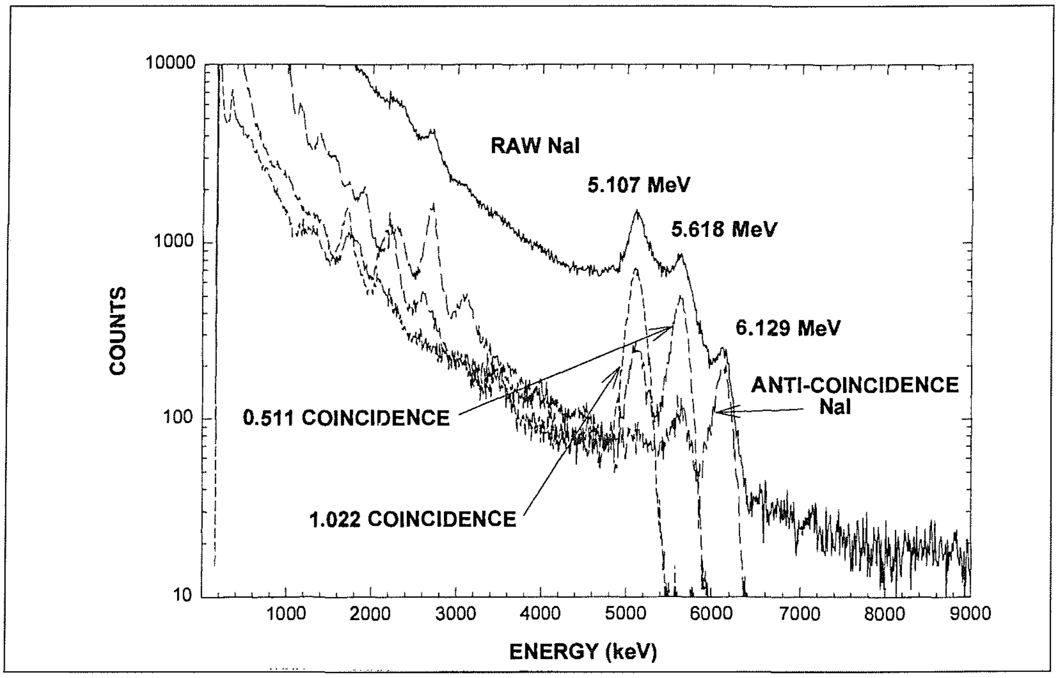

Figure 2.3 The NEAR spectrometer energy-loss spectrum from a $Pu^{13}C$ *source*

Due to the lack of a boom and therefore the need to shield the detector from cosmic-ray/spacecraft induced background the low resolution BGO shield contains 90% of the mass of the detector. Thus the sensitivity of the detector will be relatively low when compared to that of the Apollo spectrometers. However the benefits of a long observation time and the ability to perform pair production analysis should provide the necessary information required to determine the elemental composition of 433 Eros and hence provide new clues pertaining to the origin and formation mechanism of the Solar System.

Missions to Mars

The Mars Observer space craft was due to begin mapping the atmosphere, surface and interior of Mars in August 1993. Unfortunately communication with the spacecraft, was lost three days into the Mars orbit insertion phase. One of the objectives of the mission was to determine the elemental and mineralogical character of the surface materials and to do this the spacecraft carried a cooled high purity germanium spectrometer. The spectrometer was designed to return a spectrum from Mars every 20 seconds allowing a map of the surface to be made. The Mars Observer GRS consisted of a sensor head and a central electronics assembly, which were separated from each other by a 6m long boom as shown in Figure 2.4 [2].

The solid state detector was a large crystal of n-type ultra high-purity, approximately 5.5cm in diameter by 5.5cm long, with semiconductor electrodes implanted or diffused such that the crystal becomes a diode. The diode would have been operated in reverse bias mode with a potential of 3000V and a leakage current of less than 1nA. To maintain this low leakage current the detector had to be maintained at less than 130K. In a laboratory the ideal temperature would be that of liquid nitrogen. However this temperature was unattainable on the Mars Observer and therefore the detector was designed to operate at a higher temperature. The higher temperature would not have effected the energy resolution of the detector until after 1 year of exposure to radiation in space, to extend the life beyond 1 year the detector would need to be operated below 100K [54]. To overcome the effect of radiation damage and hence radiation degradation it was proposed to anneal the germanium at 370K for several days using the onboard heaters. This process would take place approximately once a year.

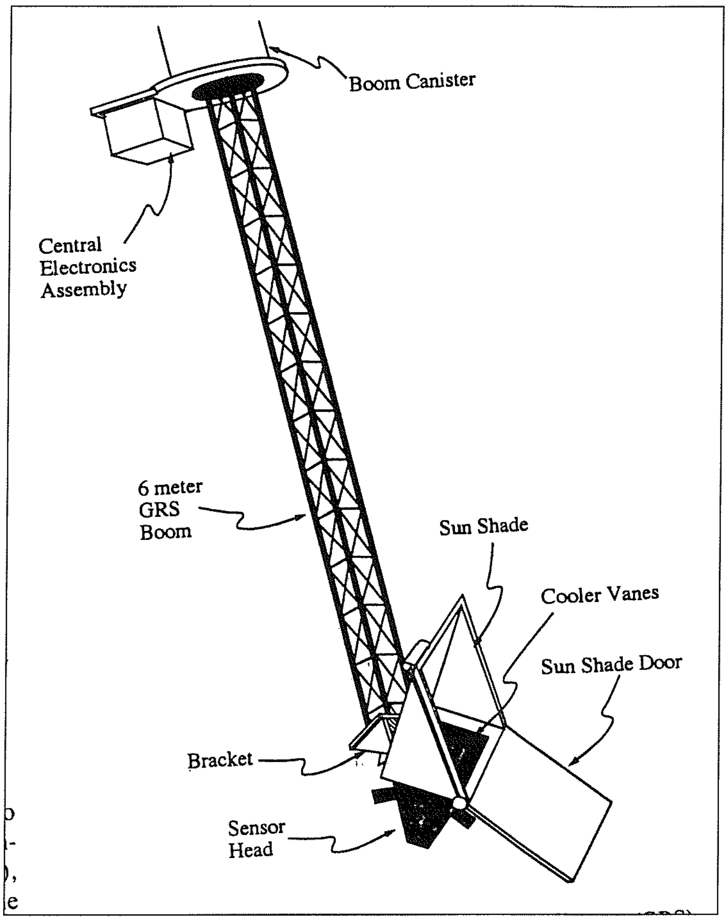

Figure 2.4 The Mars observer GRS boom

The HPGe detector was shielded from high energy particle events by an anticoincidence shield. The shield consisted of a scintillator, which was read out by two PMT's. Any high energy particles incident on the detector would deposit energy in both the HPGe and the shield and hence could be rejected from the recorded spectrum. In addition the anticoincidence shield was designed to act as a neutron detector designed to map the concentration of light elements on the surface such as hydrogen. The whole detector head is shown in Figure 2.5.

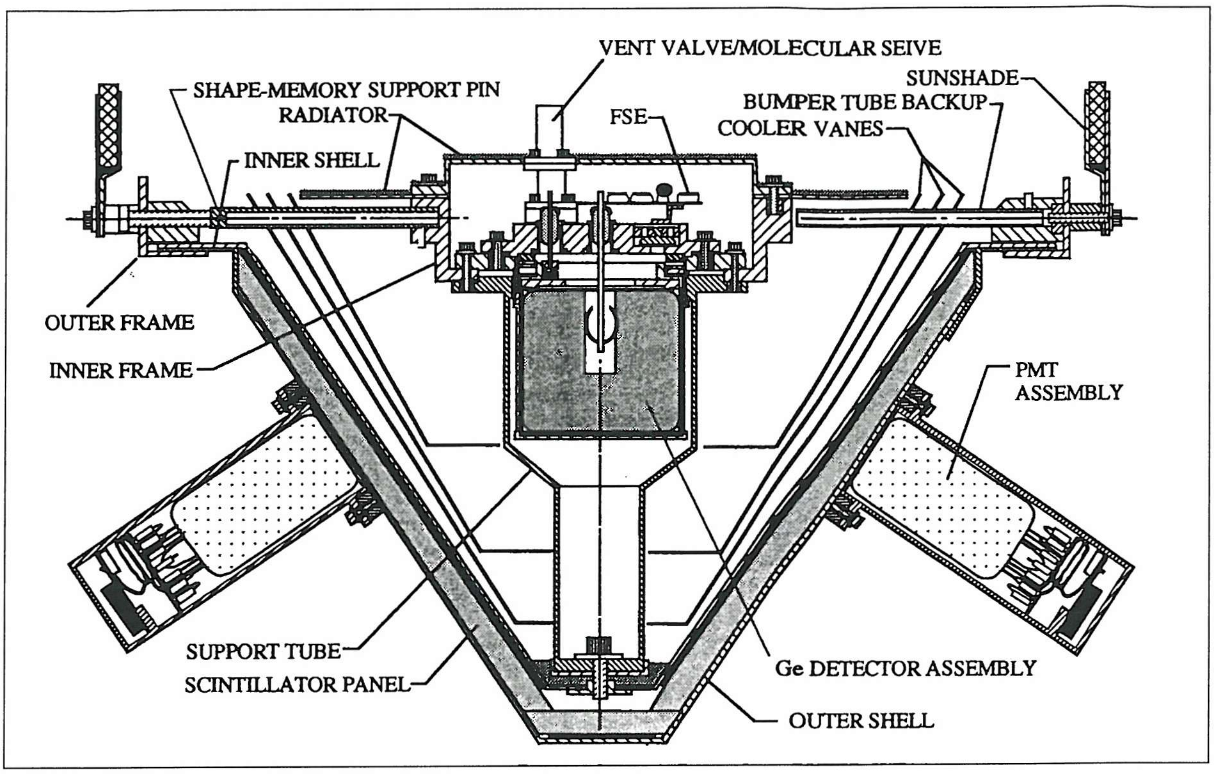

Figure 2.5 The head of the Mars observer GRS

The Mars Observer mission is not the only geochemical mapping mission to Mars that has failed. In 1989 one of the two Phobos spacecraft reached Mars with a large CsI(Tl)-PMT scintillator on board. Before the spacecraft was lost, spectra with low statistics were recorded from which some extremely limited composition results have been obtained. [55], [42].

The most recent mission to map the chemical composition of Mars was the ambitious Russian Mars 96 mission, which had several GRS's onboard, including two CsI(Tl) scintillators and germanium detector with passive cooling [43]. Unfortunately the spacecraft crashed in the Pacific, soon after launch in November 1996. One of the spectrometers, called the PHOTON consisted of two detection units, both using CsI(Tl) scintillators. One crystal was placed inside a bismuth germanate collimator to perform high spatial resolution measurements, whilst the other remained unshielded to get better counting statistics from the Martian surface. The high precision gamma-ray spectrometer (PGS) consisted of two HPGe crystals, which would have a lower efficiency than the scintillators but would provide very-high energy resolution of approximately 3keV at

1.3MeV. The PGS was constructed in collaboration with the US and each crystal was designed to be very similar to the HPGe crystal of the ill-fated Mars Observer GRS.

To date there have been no successful missions to remotely map the surface chemistry of Mars by neutron activation analysis. ESA and NASA are both planning missions to go to Mars in the next century and eventually it is hoped that a remote geochemical mission to Mars will succeed and return a gamma-ray map for the planet. The spectra from Mars will however need additional considerations when determining the chemical composition of the surface. This is because the depth of the Martian atmosphere is of the order of the photon interaction length for the low-energy photons which are of interest when performing neutron activation analysis [56]. Therefore significant corrections would be needed to interpret the recorded data from an orbiting spectrometer.

A Future Mission to Mercury

To approach the basic scientific questions on the formation and evolution of Mercury one needs data on its chemical composition. The gamma-ray flux emerging from the surface of the planet contains qualitative and quantitative information about the surface chemistry and Monte Carlo simulations have shown that it will be possible to distinguish between the different theories, for the formation of the planet, by observation of the gamma-ray spectrum [1]. Different surface compositions were assumed for the calculations and the calculated gamma-ray spectra allow clear distinction between the three types of surface composition. The simulated spectrum from the “preferred” Mercury composition is shown in Figure 2.6.

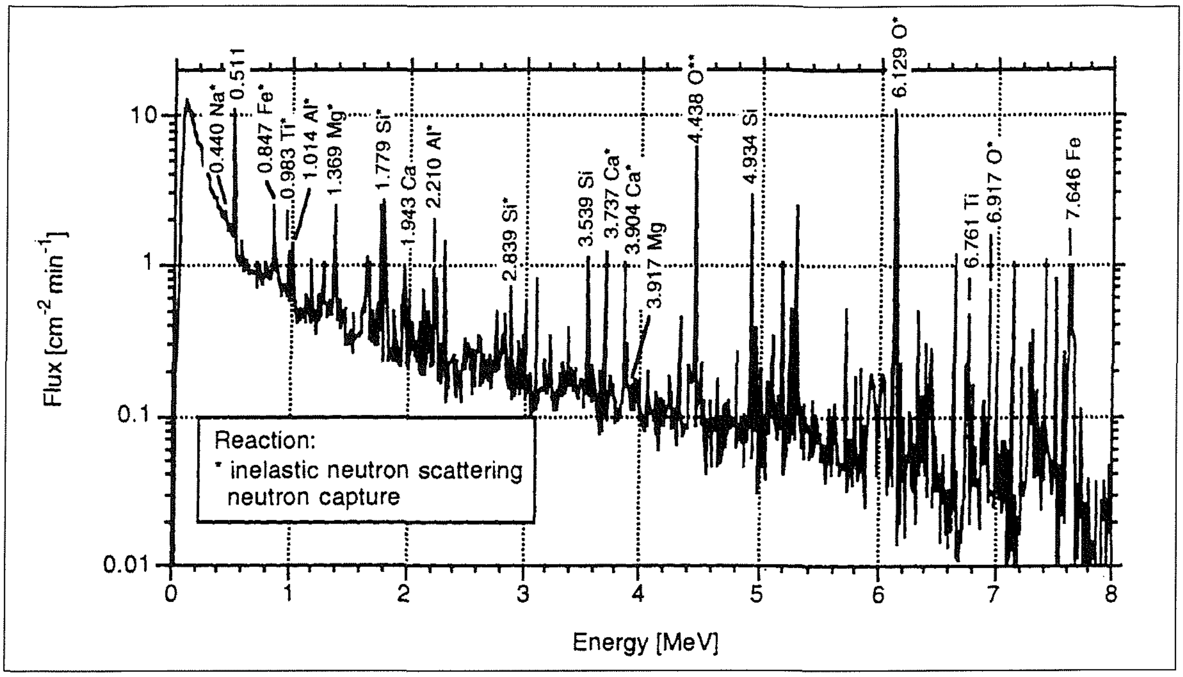

Figure 2.6 The predicted preferred Mercury emission spectrum

A mission to Mercury and the inner solar system has been accepted as one of the three cornerstones of ESA's "Horizon 2000+" programme and as such could be launched before 2010, arriving at Mercury 3 years later. Included in the primary model payload is a gamma-ray spectrometer for mapping the chemical composition of the surface [57]. A spacecraft orbiting Mercury would be subject to extreme thermal conditions due to the proximity of Mercury to the Sun and the extreme changes in surface temperature between night and day. A HPGe detector must be cooled to below 120K for normal operation and below 90K for continuous use in a high radiation environment. This will only be possible using active cooling devices such as Stirling coolers which are currently too heavy and require too much power to be considered for the mission [29]. Therefore an alternative room-temperature scintillator detector is required to map the gamma-ray spectrum emerging from the surface of the planet. Options for a scintillation detector include the NaI(Tl)-PMT and BGO-PMT detector such as those on the NEAR and Lunar Prospector spacecraft or an array of CsI(Tl)-photodiode crystals.

2.4 Conclusions

This chapter has given an overview of the history of planetary gamma-ray spectrometry, described the missions that are currently in operation and highlighted at least one future mission that will require a gamma-ray spectrometer. It may be seen that the early spectrometers such as those used for the Apollo missions were NaI(Tl)-PMT detectors. In the 1970's the technology for manufacturing large HPGe crystals was perfected and subsequent high profile missions attempted to use these detectors to map the surface of Mars. Unfortunately, a cooled HPGe detector has never succeeded in mapping a planetary surface and thus the true benefit of such a detector remains untested. The two most recent missions, the Lunar Prospector and the NEAR missions, have reverted back to the scintillator-PMT design of spectrometer due to the simplistic nature of the detector and the low cost associated with buying such a detector from an industrial manufacturer. This has been a symptom of NASA's policy to increase the number of Discovery class missions, which can do meaningful science for less than \$150M. The Lunar Prospector has been a success to date and should result in a comprehensive map of the lunar surface. The NEAR mission is set to rendezvous with the asteroid 433 Eros in February 1999 and has had no problems during the cruise phase. There will probably be several planetary missions in the next twenty years, some of which will include a gamma-ray spectrometer. The Mercury orbiter mission is one such mission destined for launch around 2010. This thesis aims to demonstrate that CsI(Tl)-photodiode arrays are a viable alternative to scintillator-PMT detectors and will have a greater sensitivity to a planetary emission spectrum, due to an increased mass of sensitive material per mass of detector and a finer energy resolution at gamma-ray energies above 2MeV. Thus, when the mass, power or financial constraints on a mission preclude the use of cooled HPGe, a CsI(Tl)-photodiode array spectrometer should be the choice of detector for remote planetary geochemical analysis.

Chapter 3

3 The Design of Gamma-ray Scintillation Spectrometers for Remote Geochemical Analysis

3.1 Overview

Previous planetary missions have included gamma-ray spectrometers that have used scintillator crystals and HPGe detectors. The most recent planetary missions have used scintillator-PMT spectrometers and some possible future missions, such as the Mercury Orbiter, may require a scintillator gamma-ray spectrometer to perform remote geochemical analysis of the surface. This chapter determines the factors that dominate the sensitivity of a scintillator detector and considers the impact of each of the factors when performing remote geochemical analysis. The responses of a NaI(Tl)-PMT detector, a BGO-PMT detector and a CsI(Tl)-phtodiode array, to the lunar spectrum, have been simulated to demonstrate that a CsI(Tl) array may offer significant advantages over the PMT detectors for this application.

3.2 Introduction

The primary requirement of a gamma-ray spectrometer for a future mission, is the ability to resolve the features expected in the gamma-ray spectrum emerging from the surface of the planet. Thus the gamma-ray spectrometer must combine an adequate energy resolution with a high sensitivity, in order to provide a fine spatial resolution of the surface and quantification of the elemental abundances. The ideal spectrometer would have a sufficiently high stopping power, to absorb all of the incident photon energy, which could be as high as 10 MeV, implying the need for a large volume of high Z detector material. The detector also needs to be able to distinguish weak emission lines from the underlying background, which arises from the scattering of photons before emerging from the planet and activation of the body of the spacecraft. This requires a fine energy-resolution, across a broad spectrum of gamma-ray energies. Finally, the system should make modest power requirements and operate close to room temperature for ease of integration into a spacecraft payload. Unfortunately, at present such an ideal detector does not exist and therefore the choice of gamma ray spectrometer will be strongly influenced by the particular scientific goals of the mission and space-craft engineering constraints.

3.3 Factors Affecting the Performance of a Scintillator Gamma-ray Spectrometer

The sensitivity of a gamma-ray spectrometer, to a gamma-ray emission line, above a source of background, depends on the energy-resolution, the statistical quality and the photofraction. Therefore, to optimise the gamma-ray spectrometer, consideration must be given to the properties of the scintillation crystal, the geometry of the detector and the response of the photodetector when incorporated with the scintillator crystal. All of these factors are considered in the following discussion to determine an optimum design of scintillator spectrometer.

3.3.1 Spectral Resolution

There are several factors that affect the energy resolution of a gamma-ray spectrometer:

- Statistical fluctuations in the number of charge-carriers produced in the photodetector for a given energy deposit.

- Quantum efficiency and non-uniformity of the photodetector.

- Intrinsic variations in the light output of the scintillator, due to the crystal structure, defects and doping variations.

- Variations in the light-collection efficiency, which is dependent on the position of interaction of the incident gamma-ray within the scintillator.
- Electronic noise.

The **statistical noise** arises from the fact that the charge (Q), generated within the photodetector, is not a continuous variable but represents a discrete number of charge carriers. The number of carriers is subject to random fluctuations from event to event, even though exactly the same amount of energy may be deposited in the detector. Assuming that the formation of each charge carrier is a Poissonian process, giving rise to a total number of N charge carriers, a standard deviation of $\sqrt{N}$ would be expected. Since N is typically a large number, the response function should have a Gaussian shape. Here G(H) is the amplitude of the function at position H, A is the area under the Gaussian and H_0 is the position of the centroid or mean of the distribution. The standard deviation σ determines the FWHM through the relationship FWHM=2.35σ.

$$G(H) = \frac{A}{\sigma\sqrt{2\pi}} e^{\left(-\frac{(H-H_0)^2}{2\sigma^2}\right)}$$ *Equation 3.1*

Therefore we can calculate a limiting resolution R due to only statistical fluctuations in the number of charge carriers as:

$$R = \frac{FWHM}{H_0} = \frac{2.35\sqrt{N}}{N} = \frac{2.35}{\sqrt{N}}$$ *Equation 3.2*

Note that as N increases the limiting resolution decreases. Thus when counting statistics dominate the source of energy-resolution broadening, the detector that provides the greatest number of charge carriers, per unit energy deposited in the scintillator, will have the finest energy resolution. CsI(Tl)-has the highest light yield of all the scintillator crystals and when combined with a photodiode having a quantum efficiency of approximately 80%, can provide, if well designed, a better statistical energy resolution than NaI(Tl) or BGO-PMT detectors.

From Table 3.1 it may be seen that the alkil-halides, NaI(Tl) and CsI(Tl), have an excellent scintillation efficiency, with CsI(Tl) having the highest light output of all the scintillator materials. There are also some exotic glass scintillators, such as LSO that have similar scintillation efficiencies to the alkili-halides at room temperature and in general the glass scintillators have a higher linear attenuation coefficient than the alkili-halides. However they also have a higher density which means that, for a given mass of scintillator, there will be less volume of these materials. LSO also has the disadvantage of being naturally radioactive.

Scintillator Material	Peak Emission [nm]	Density [g/cm^3]	Light Yield [photons/MeV]
NaI(Tl)	415	3.67	38000
CsI(Tl)	550	4.51	52000
BGO	490	7.13	8200
LSO	420	7.4	30000

Table 3.1 A summary of the properties of 4 scintillators. All values are for room temperature operation

In order to quantify the scintillation light emerging from the scintillating crystal the photodetector must have the best possible **quantum efficiency** at the wavelength of emission. It may be seen from Table 3.1 that the wavelength at which the light output peaks, varies for each type of scintillator. The light from a scintillator may be measured by using a photomultiplier tube or a photodiode. Figure 3.1 shows the spectral response and quantum efficiency of several PMT's and a photodiode. Also shown for reference is the emission spectrum from a CsI(Tl) scintillator.

As may be seen the spectral response of a photodiode increases with increasing wavelength and hence is most suited to the emission of CsI(Tl) which has the longest wavelength of the scintillator crystals. Other crystals may be used with photodiodes but the conversion efficiency will be lower and hence the number of charge carriers will be reduced and the energy resolution will be broader. Crystals such as NaI(Tl) and BGO are usually used in conjunction with a PMT due to it having a low noise characteristic. For remote geochemical analysis it would not generally be feasible to use a NaI(Tl) or BGO crystal with a photodiode because it would result in the energy resolution being dominated by the electronic noise from the dark current over most of the energy range of interest.

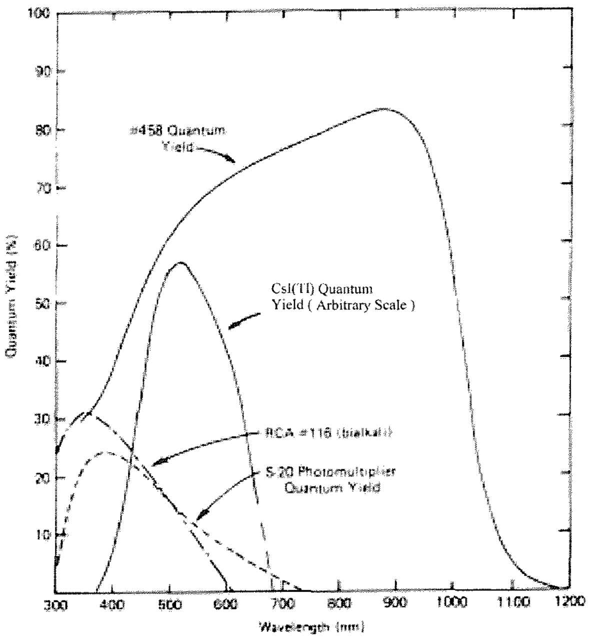

Figure 3.1 A comparison of the quantum efficiency of a silicon photodiode (labelled #458) with representative bialkali and S-20 photocathode quantum efficiencies. The emission spectrum from a CsI(Tl) scintillator is shown for reference.

Typically, CsI(Tl) has a light yield of 52000 photons/MeV. Assuming a light collection efficiency of 90%, a quantum efficiency of 80% and a band gap of 3 to 4eV in the silicon of the photodiode, the theoretical number of electron-hole pairs created per MeV is approximately 37400 [58]. If the energy resolution of a detector were due to photon counting statistics alone, the energy resolution would be better than is actually observed. The difference between these values is due to electronic noise, the transfer variance and the intrinsic resolution of the detector.

The **intrinsic resolution** of a scintillator detector can be attributed to two factors [59][60]:

- The non-proportional response (R_{np}) of the scintillator
- The inhomogeneity of the crystal (R_{inh})

The non-proportional broadening is principally due to the non-proportional light yield of the scintillator. When an electron interacts with matter, it is known that the ionisation density in the track increases with decreasing primary electron energy. This phenomenon was used by Murray et al [61] to explain the non-proportional response observed for NaI(Tl^+) and CsI(Tl^+). They proposed that a free electron and a free hole, from the ionisation track, first need to form an excitation like state, this excitation is then trapped by a Tl^+ site. The probability, of forming the exciton-state, increases with the concentration of free electrons and holes, i.e. with the ionisation density track as shown in Figure 3.2. As a result, the light yield per unit electron energy increases with a decrease of electron energy.

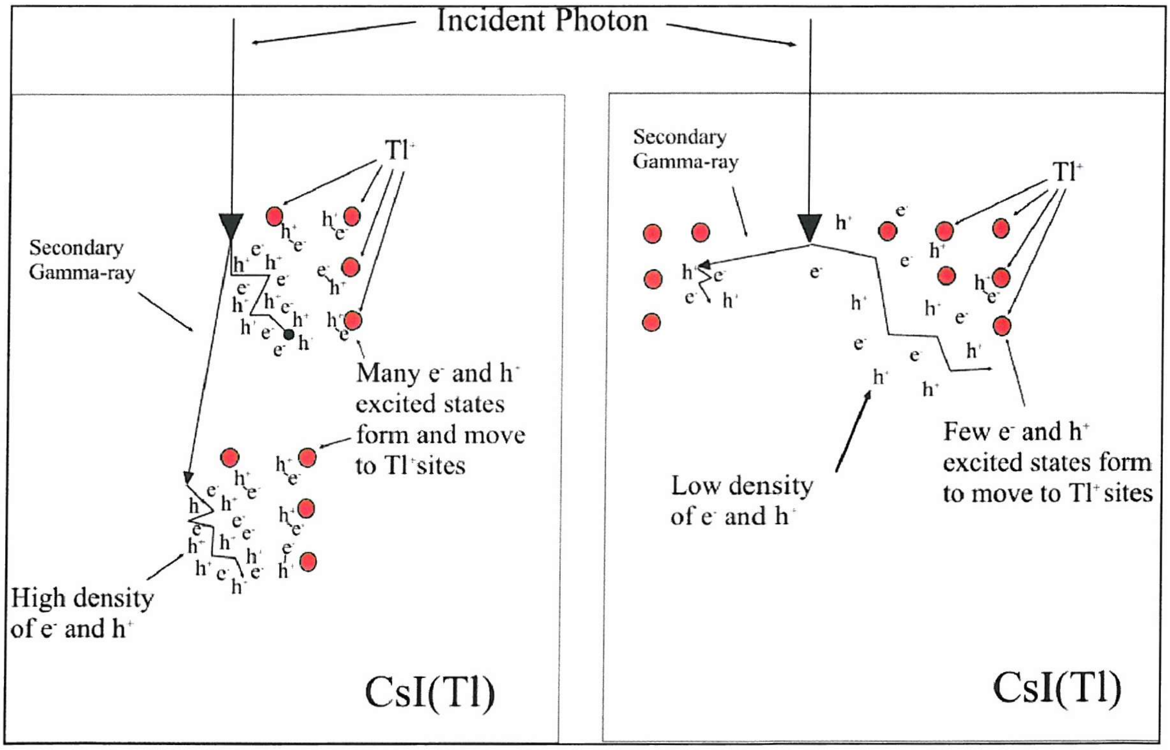

Figure 3.2 Compton Interactions Resulting in Different Light Outputs for the Same Incident Energy

It is also possible to speculate that, if the density of the excited states is sufficiently high, one can imagine that some of the free electrons and holes will recombine before reaching a luminescence centre and will be lost to the scintillation process. In this case, a decrease in light yield per unit electron energy will result from decreasing electron energy. Thus there will be a peak in the light-yield per unit energy, which corresponds to the maximum electron-hole density that can be efficiently transferred to the Tl^+ sites. Figure 3.3 shows the light output from CsI(Tl) and BGO as a function of electron energy [62]. It may be seen that, the light output per unit electron energy from the CsI(Tl) crystal peaks at 10keV. This may be explained by assuming that the electron-hole pair density, for electrons below 10keV, is too high for all the pairs to migrate to a Tl+ site, where de-excitation will occur. Above 10keV, the formation of the electron-hole pairs, are less dense and as a result are less likely to form an excited state, which can migrate to the thallium sites. The BGO crystal does not exhibit a peak, which indicates that there is no saturation point or that the mechanism for the transfer of energy, to the activation sites, is different.

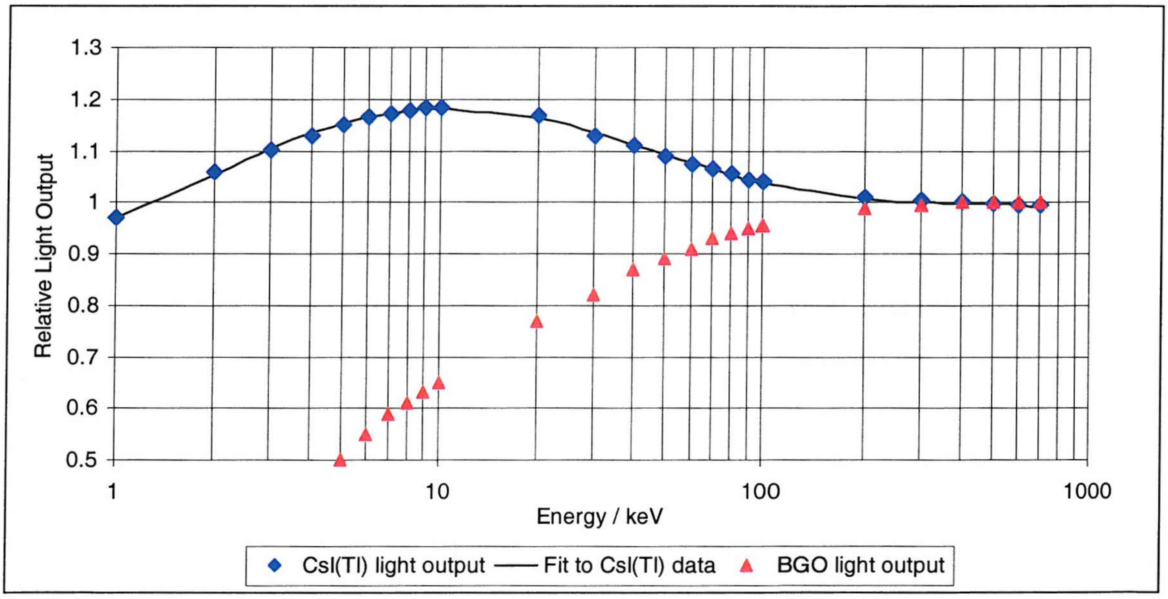

Figure 3.3 The relative light output verses electron energy for BGO and CsI(Tl). The response curves are normalised to the light output at 442keV [62]

An experiment was carried out to determine what proportion of the observed intrinsic resolution, of a CsI(Tl) crystal, could be accounted for by the non-proportional response. A GEANT Monte-Carlo simulation was performed to determine the range of energy of the electrons that are generated by a 662keV photon interacting with an infinitely large CsI(Tl) crystal. The combination of electron energies generated is not a continuous distribution and may be grouped into five categories, each of which would result in a slightly different number of optical photons being generated in the scintillator.

The relative number of photons generated in the scintillator can be calculated by multiplying each electron energy by the electron response curve. This was performed for 1×10^5 photons and the relative distribution is shown in Figure 3.4. There are many features in the simulated light output spectrum, which may be explained by analysis of the individual photons resulting in each peak. It may be noted that the peak of the simulation is 666keV instead of 662keV. This is due to the majority of the electron response curve being above the normalised value at 442keV.

- Region "a" is due to a photoelectric interaction, resulting in 2 electrons, one of which is the result of the photoelectric effect whilst the other is a K-shell electron from Iodine.
- Region "b" is due to a single Compton-scattering event followed by the scattered photon depositing its energy by the photoelectric effect. This results in two electrons of roughly equivalent energy.
- Region "c" is due to a photoelectric interaction which results in a photoelectron that induces a K-shell and an L-shell X-ray from an Iodine or Caesium atom. The K-shell X-ray is of the order of 30keV and the L-shell X-ray is of the order of 5keV.
- Region "d" is the result of 2 Compton scatter interactions followed by the photoelectric effect, resulting in 3 photoelectrons.

Interactions where more than three energy deposits take place have less distinct features, due to the increase in the number of combinations that may take place, resulting in 4 or 5 photoelectrons.

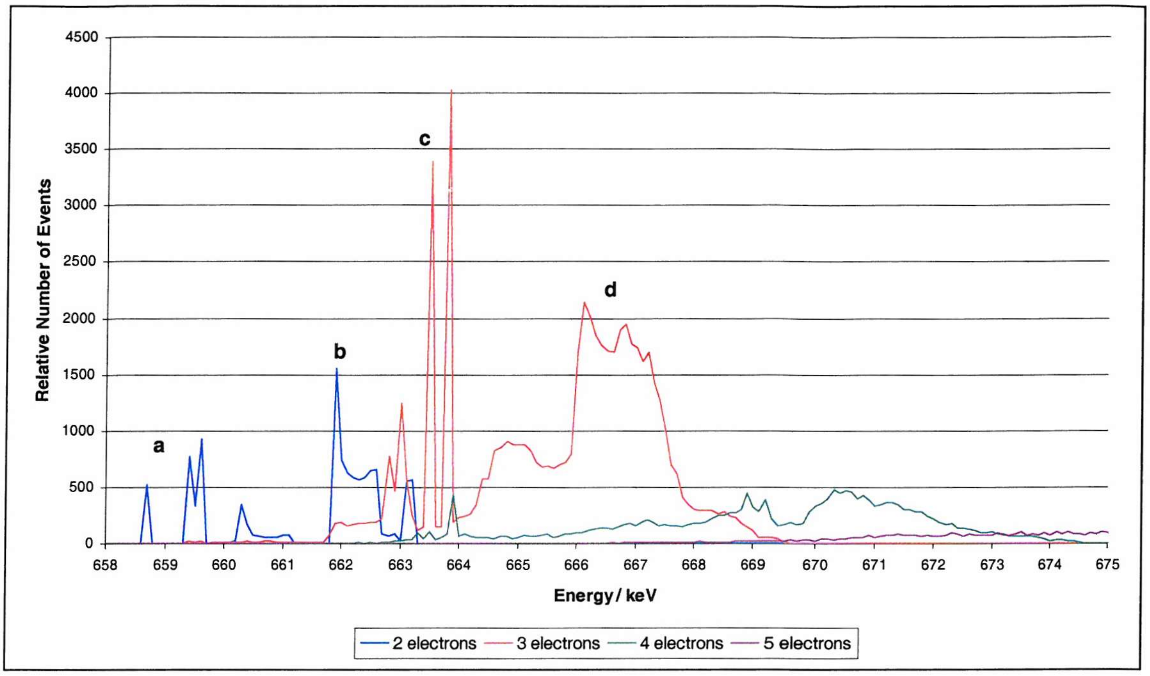

Figure 3.4 The simulated relative scintillation light produced by each type of energy-loss interaction when a CsI(Tl) crystal is irradiated with 662keV photons. The number of photons/MeV is normalised to the light produced by a 442keV electron.

The spectrum shown in Figure 3.4 is the ratio of each combination of electrons and shows the relative mean energy resulting from that combination of electrons. However, when a gamma-ray interaction takes place, there will be a statistical variation in the number of photons resulting from the energy deposit. Figure 3.5 shows the simulated shape of the scintillation–light from a CsI(Tl) crystal at 662keV with the statistical variation applied.

When statistical variations are applied to the spectrum shown in Figure 3.4, it may be seen that the features resulting from the different types of interaction are blurred into a continuous distribution, as shown in Figure 3.5. The distribution is approximately Gaussian but includes a high energy tail, which is a result of gamma-ray energy deposits that result in many photo-electrons. The FWHM of the light produced is approximately 11keV or 1.65%.

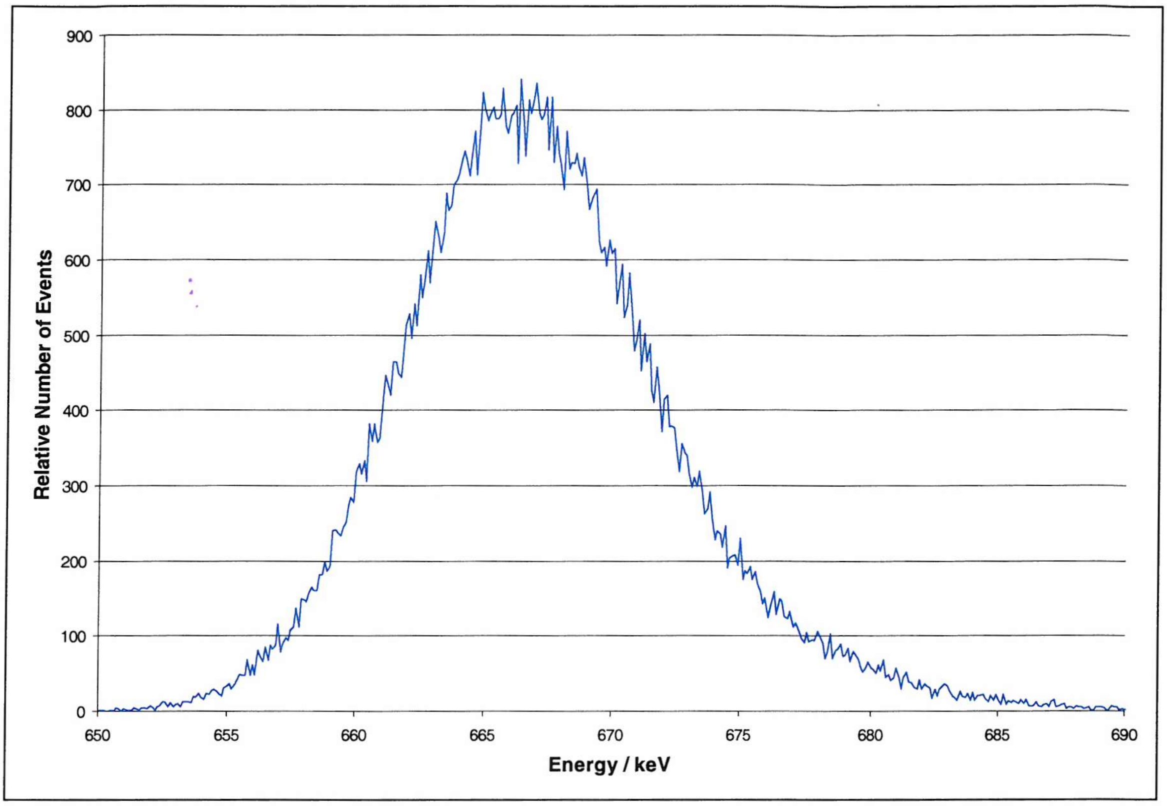

Figure 3.5 The simulated scintillation-light produced in a CsI(Tl) crystal irradiated by 662keV photons relative to the light produced due to a 442keV electron. The spectrum includes the effect of statistical variations in the light produced.

The energy resolution of a CsI(Tl) crystal has been measured using a hybrid photodiode. The advantage of a hybrid photodiodes is that it has a negligible electronic noise contribution to the resolution of the detector and it is possible to count the number of photons produced by each interaction [63]. The measured energy resolution at 662keV is 8% FWHM. The resolution due to charge carrier statistics has been calculated to be 5.5%. Therefore, when combining the errors in quadrature, the non-statistical contribution must be of the order of 5.8%. The simulated contribution due to the non-proportional response of the crystal is 1.65% FWHM and therefore does not account for all of the difference between the measured resolution and the resolution due to photon statistics. Therefore other non-statistical effects must be contributing to the overall energy resolution.

The second source of intrinsic resolution is the inhomogeneity within a crystal. This may cause local variations in the concentration of luminescent centres, which will result in local variations in the scintillation light output. The number of scintillation photons is then dependant on the point in the crystal at which the scintillation pulse is created and hence will result in a broadening of the energy resolution. For CsI(Tl) crystals it has been shown that variations in the concentration of thallium have little effect on the light output provided the concentration lies between 600 and 1300 ppm [58] and therefore this source of resolution degradation will not contribute significantly for well manufactured crystals.

The intrinsic resolution of a gamma-ray spectrometer becomes particularly important when measuring gamma-rays at energies of several MeV where the statistical counting effects and noise degradation are reduced to levels of less than 1 or 2% FWHM. The intrinsic energy resolution of the alkili-halide scintillators NaI(Tl) and CsI(Tl) have been measured up to 1.33MeV and were found to be of the order of 1% FWHM, for energies over 1MeV [60]. However, direct measurement has not been performed above this energy. The same measurements have been performed for other crystals such as BGO and LSO and the intrinsic energy resolution has been found to be significantly better than the alkili-halides [59]. Therefore, when comparing different crystals for use in a spectrometer for remote geochemical analysis, this would suggest that using BGO as the sensitive medium would be an advantage. However the light output of BGO is only 8000 photons/MeV which means that the energy resolution will remain significantly worse than is achievable using CsI(Tl) or NaI(Tl) unless the energy deposit is of the order of 10MeV.

The **transfer variance** is the difference in the light collection efficiency for a gamma ray interaction, depending on the position within the crystal at which the energy deposit occurred. Intuitively, it can be imagined that light produced further away from the photodetector, will have a greater probability of interacting with the walls of the crystal, than light produced close to the sensitive surface, and hence will have a greater probability of being absorbed. However, light produced further away from the photosensitive surface will, in general, have a lesser angle of incidence to the vertical when it reaches the photosensitive surface. Therefore, a greater proportion of the light will be absorbed by the photodiode and as a result a larger signal may be generated by the photodetector [64] as shown in Figure 3.6. Scientists, working with calorimeters, for particle physics experiments often observe this phenomenon. The crystals used in such applications are of the order of 40cm long and as a result the variations in signal due to transfer broadening are very significant. The exact variation throughout the volume of a crystal is dependent on both the above factors and the dominant factor will depend entirely on the crystal geometry, surface preparation and quality of contact between the photodetector and crystal. The crystals being considered for use in remote geochemical analysis will not exceed 10 cm long and, provided the ratio of the cross-sectional width to the length does not exceed 3 or 4 then the transfer variance should not contribute significantly to the total energy resolution of the detector [58].

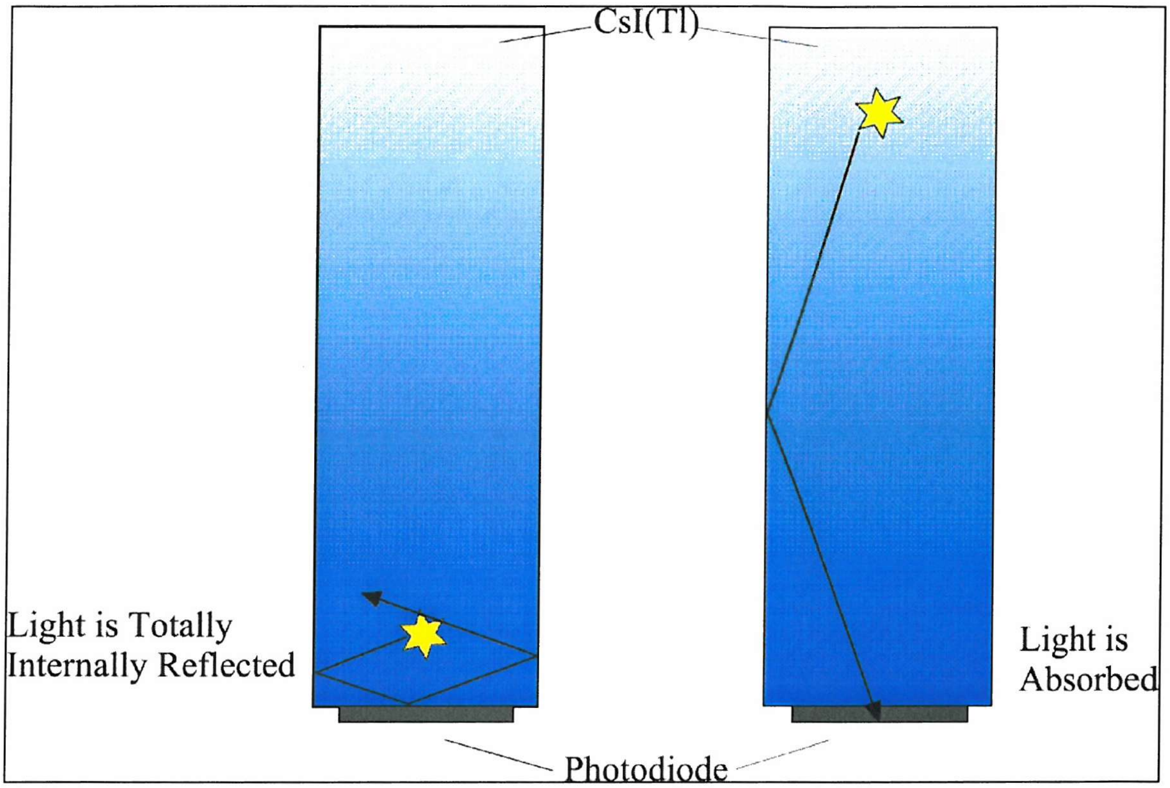

Figure 3.6 Light transfer within a CsI(Tl) crystal

The **electronic noise** is important when the number of charge carriers generated at the photodetector are of a similar magnitude to the random electronic fluctuations. Therefore, electronic noise is an important consideration when measuring gamma-rays with energies in the 0 to 1MeV region of the spectrum. The most significant source of random electronic noise from a photomultiplier tube results from the thermionic electrons, which are spontaneously emitted from the photocathode. The pulses that arise from this process usually correspond to a single photoelectron, so their amplitude is limited. Since most scintillation counting is done under conditions in which a scintillation pulse corresponds to many photoelectrons, the thermal noise is not significant when analysing the emission spectra from a planetary surface.

Conventional photodiodes have no internal gain and operate by directly converting optical photons, from the scintillator, to electron-hole pairs that are collected. Scintillation crystals produce several tens of thousand optical photons per MeV and the charge pulse is limited to no more than the same number of electronic charges. Because of the small signal amplitude, noise from fluctuations in thermally generated charge carriers (the dark current) can be a problem, especially for large area detectors and low energy radiation. In general photodiode detectors will have a much higher noise contribution than standard photomultiplier tubes and therefore are not suited to scintillators that have a poor light yield or for measurements below 50keV. Photodiode detectors are better suited to high light yield scintillators, such as CsI(Tl), for measurements at energies above 100keV. Clearly this does not pose a problem when performing remote geochemical analysis, in which case the energy region of interest is between 0.5 and 10MeV.

The effect of all the above mentioned terms are described mathematically Equation 3.3.

$$\sigma_{total}^{2} = \sigma_{e^-}^{2} + \sigma_{\text{int}}^{2} + \sigma_{trans}^{2} + \sigma_{noise}^{2} \qquad \textit{Equation 3.3}$$

Where:

- σ_{total} is the total standard deviation due to all resolution broadening effects
- $\sigma_{\text{e-}}$ is the standard deviation due to statistical variations in the number of charge carriers
- σ_{int} is the standard deviation due to intrinsic variations of the crystal
- σ_{trans} is the standard deviation due to transfer variations
- σ_{noise} is the standard deviation due to noise variations

Expanding the terms for noise variation and charge counting statistics Equation 3.4.

$$\sigma_{total}^{2} = \left[\frac{\left(N_{noise}^{2} + E \times N_{e^-}\right)}{\left(E \times N_{e^-}\right)^{2}} + \sigma_{trans}^{2} + \sigma_{\mathrm{int}}^{2} \right] \qquad \textit{Equation 3.4}$$

Where :

- N_{noise} is the rms of the variation of the number of charge carriers produced by the leakage current from the photodetector.
- N_{e-} is the number of charge carriers produced in the photodetector per unit energy deposited in the scintillator.
- E is the energy deposited in the scintillator.

From Equation 3.4 it may be seen that the ideal detector would have a low noise, high light yield from the scintillator, a high conversion efficiency of optical photons into charge carriers, a low transfer variance and low intrinsic variations. Low noise detectors include those that use photomultiplier tubes or hybrid photodiodes which have a high gain, however the highest charge-carrier yield is achieved when using CsI(Tl) with a photodiode readout, due to the high light yield of the scintillator and quantum efficiency of the photodiode. Therefore, 2" or 3" NaI(Tl)-PMT detectors are more suitable for measurements below 1.5MeV where the noise characteristics dominate the energy resolution. However, above 2 or 3 MeV the high charge carrier yield of a CsI(Tl)-photodiode detector results in a finer resolution than is achievable with a conventional 2" NaI(Tl)-PMT detector. This effect is has been measured in the laboratory and the results are presented in chapter 4.

3.3.2 Gamma-ray Detection Efficiency

The number of energy-loss events recorded by a spectrometer will be proportional to the intensity of the flux, the time of observation and the stopping efficiency of the detector. For planetary remote geochemistry the observation time will be fixed by the choice of orbit and mission lifetime. Also, providing the planet fills the field of view of the detector, the intensity of the gamma-ray flux on the detector, will be fairly constant and will be independent of the altitude of the spacecraft. Therefore, to maximise the number of recorded energy-loss events and hence the detector efficiency, it is necessary to maximise the interaction probability of the sensitive medium of the detector. This will depend on the linear attenuation coefficient of the detector and the path length through the detector, along which the incident gamma rays travel.

To observe the full-energy of an incident gamma ray, it is necessary to prevent any of the secondary electrons or photons escaping the detector. At low energy, where the photoelectric effect dominates, this means preventing the photoelectron from escaping the sensitive material. Compton-scattering dominates above a few hundred keV, which gives rise to a secondary photon. If this secondary photon escapes from the crystal, the energy-loss will contribute to the Compton continuum and not the photopeak. Clearly, the larger the sensitive volume of the material, the less likely the Compton photon is to escape and the photofraction is increased. In addition, the Compton-scattered photons are not distributed isotropically but have a distribution, which is predicted by the Klein-Nishina formula [65]. A plot of the Klein-Nishina formula is shown in Figure 3.7 for a range of gamma rays energies and it may be seen that that at high energy, the Compton photon is more likely to be projected in the forward direction. Therefore, a thin, large area detector, is not likely to detect many of those photons that interact in this manner.

At energies above 5 or 6 MeV, pair production dominates the gamma ray interaction process, and gives rise to an electron and a positron, which will share the photon energy, minus the rest-mass energy of 1.022 MeV. Assuming the electron and positron do not escape from the crystal, they will deposit their energy by Coulomb interactions until the positron annihilates with an electron thus releasing two 0.511 MeV photons. If one or both of these photons escape the detector they will give rise to an event in the single or double escape peak which will be of 0.511 or 1.022 MeV lower energy than the photopeak.

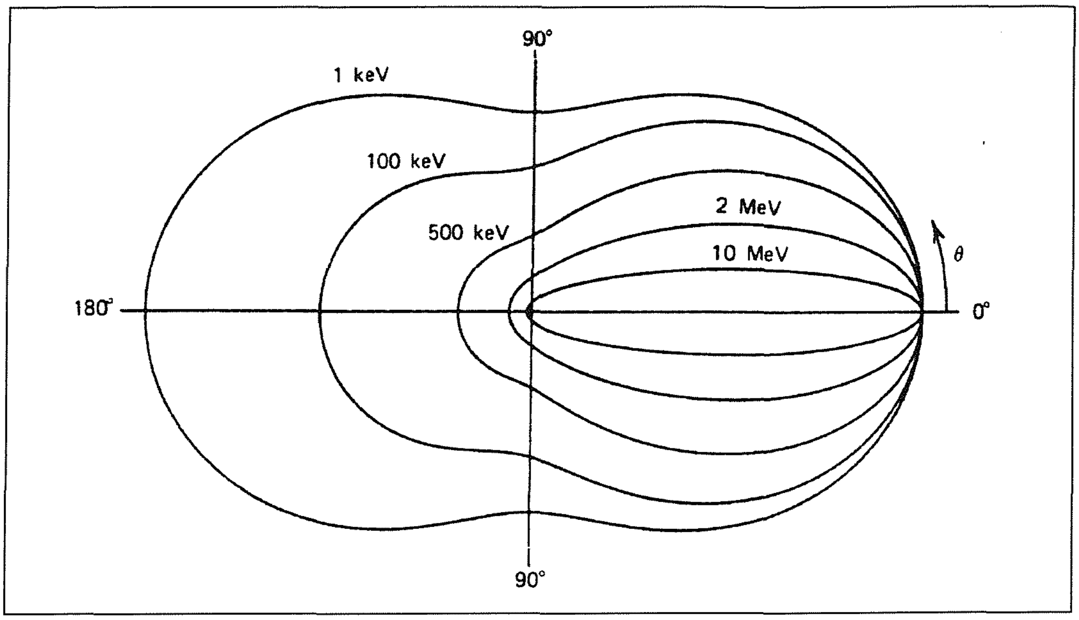

Figure 3.7 A polar plot of the number of photons (incident from the left) Compton scattered into a unit solid angle at the scattering angle θ. The curves are shown for the indicated initial energies.

When observing a planetary surface with an uncollimated detector, the gamma rays, incident on the detector, are not perpendicular to the front face of the detector but have a distribution which is shown graphically in Figure 3.8. The path length for each gamma-ray is therefore different for each angle of incidence and the position at which the gamma ray interacts on the detector. Therefore defining the interaction probability is not a simple problem and is best determined using a Monte-Carlo simulation. A broad flat detector will detect more photons than the same mass of scintillator having a smaller area and greater depth. However, a thin detector is less likely to observe the, forward-scattered, Compton photons and hence the photofraction will be smaller. The pulse-height spectrum from three differently dimensioned cylinders of CsI(Tl) have been calculated using the GEANT Monte-Carlo simulation package and are shown in Figure 3.9. The mass of CsI(Tl) is the same for each cylinder.

The number of photons in the full-energy peak of the 7cm deep detector is 3.7% greater than the number in the full-energy peak of the 5cm array and 36.6% greater than the number in the 3cm array. Therefore, without applying any spectral deconvolution, the 7cm deep detector can be said to be the most sensitive of the three geometries to a 5MeV gamma ray line. However, the number of energy-loss events in the spectrum from the 3cm deep crystal is 6.9% greater than in the 5cm spectrum and 14.8% greater than in the 7cm spectrum which, in theory, could improve the reconstruction of the incident energy-loss spectrum, when using a spectral deconvolution technique. A more detailed consideration of this effect is discussed in chapter 6.

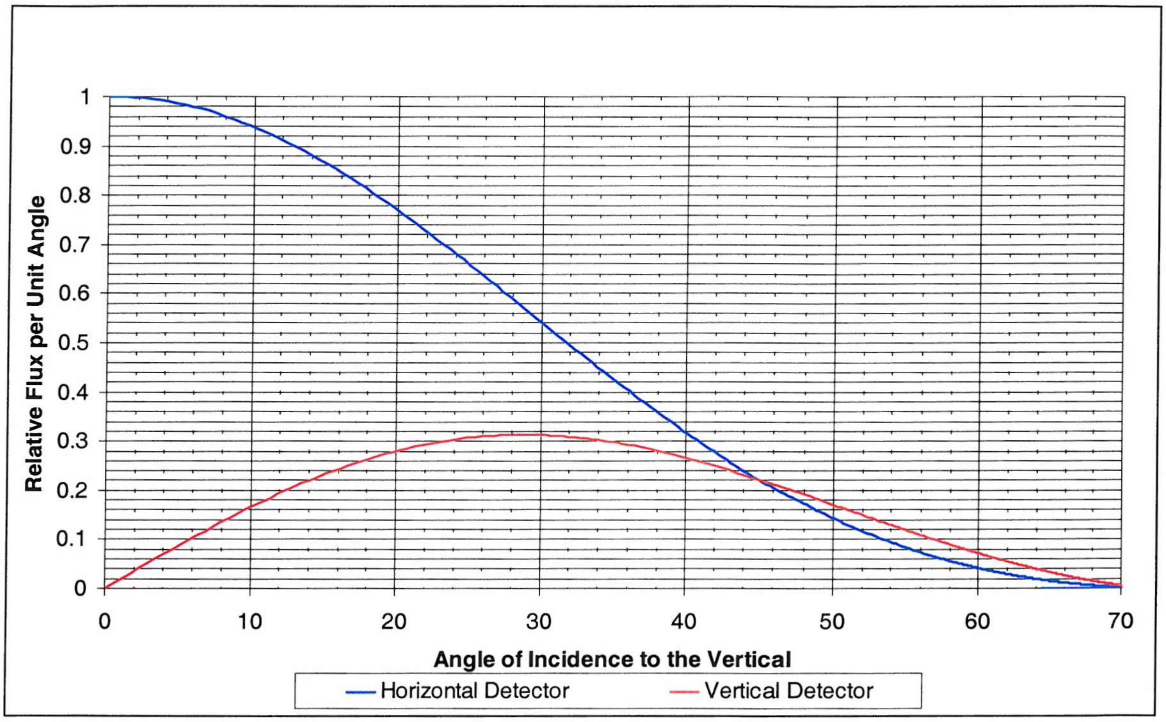

Figure 3.8 Flux distribution as a Function of Angle to the Horizontal at the detector

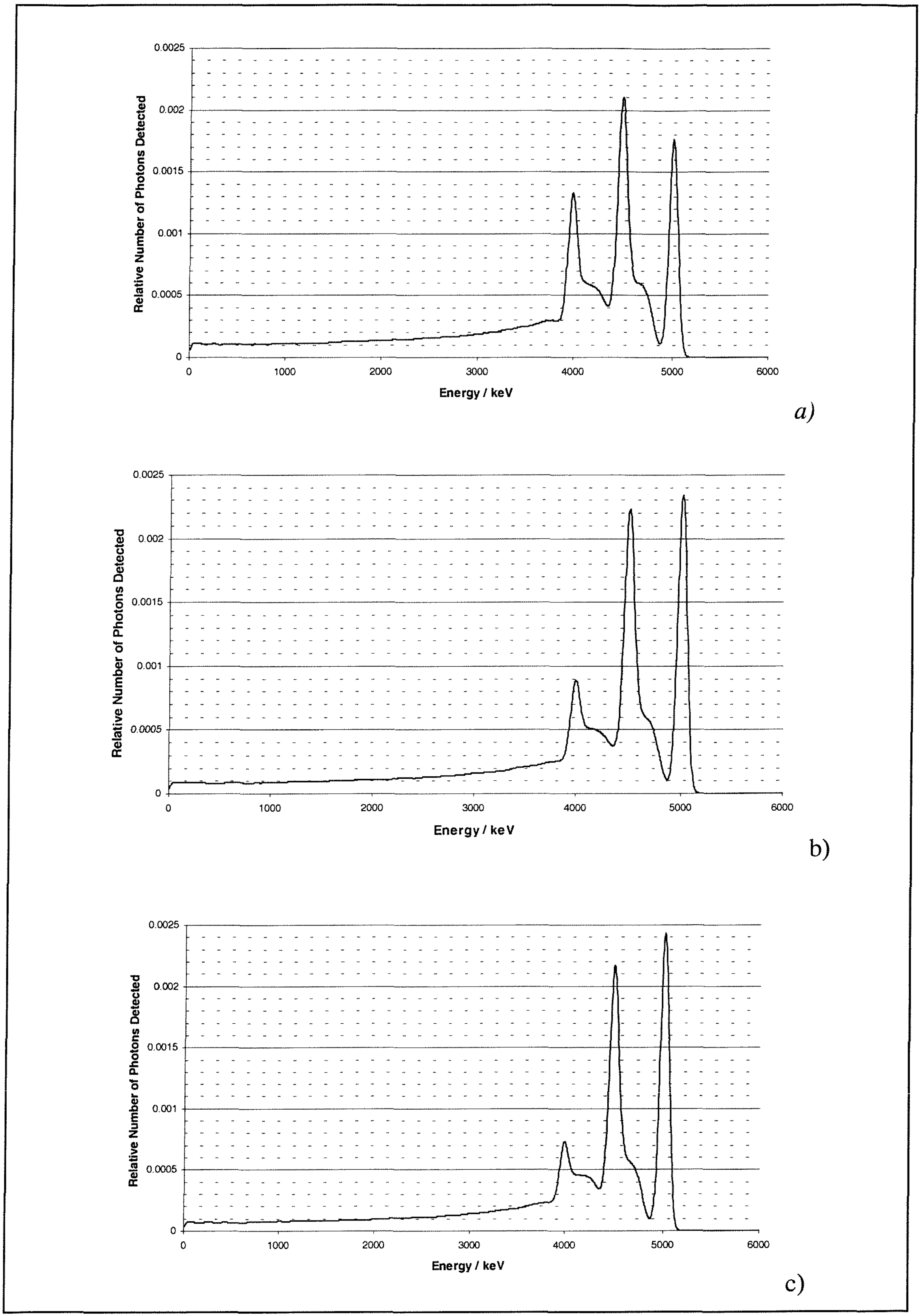

Figure 3.9 The energy-loss spectrum from a) 10.3 by 3cm, b) 7.97 by 5cm and c) 6.74 by 7cm cylinders of CsI(Tl), irradiated with 5MeV photons with a spatial distribution similar to that of an orbiting spectrometer

3.3.3 The Detector Sensitivity

The sensitivity of a gamma-ray spectrometer, to a gamma-ray emission line, above a background, will depend on the number of energy-absorption events, the photofraction and the energy resolution of the detector. Figure 3.10 shows the 1.174MeV emission line from a Co^{60} laboratory source recorded by a 1cc CsI(Tl)-photodiode detector. Such a detector would not be used for remote geochemical analysis but serves to illustrate the sensitivity of a gamma-ray spectrometer. The underlying background is due to partial energy-loss events from the 1.332MeV emission line of Co^{60}. It may be seen that this particular region of the energy-loss spectrum is well approximated by fitting a linear background superimposed with a Gaussian photopeak. The significance of the peak may be defined as the number of events in the photopeak above the background and is usually expressed in terms of the variance of the background as shown in Equation 3.5.

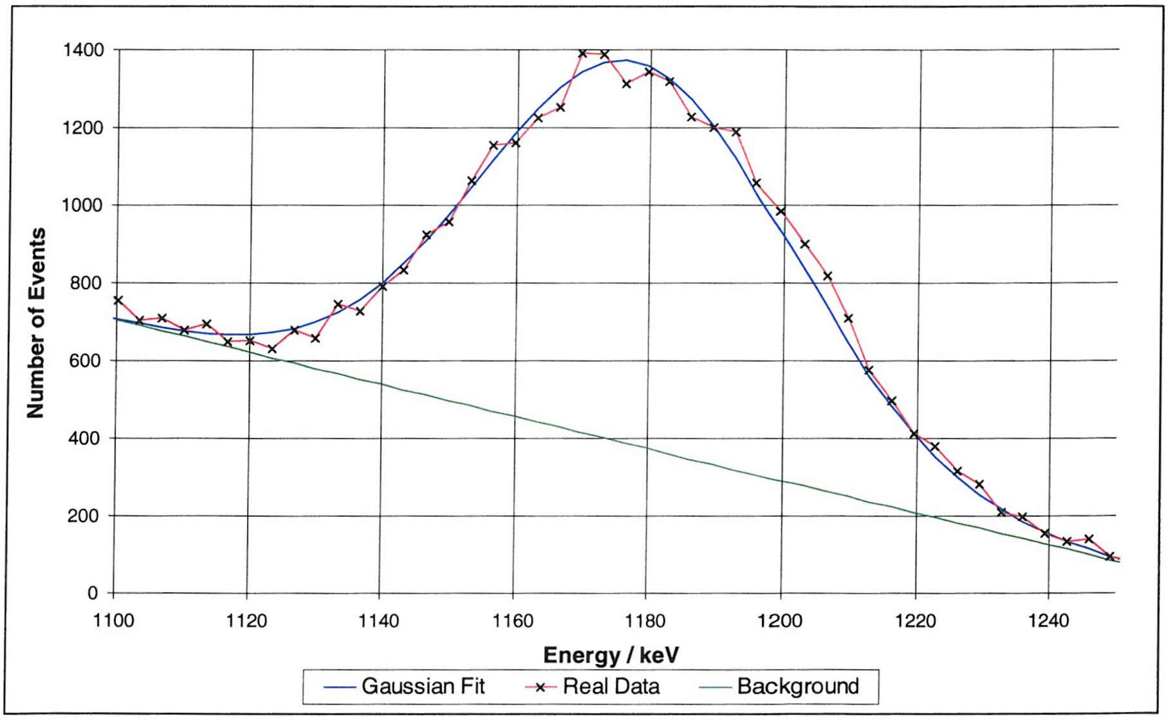

Figure 3.10 The 1.174MeV emission line from Co^{60} laboratory source

$$S = \frac{\sum_{E_1}^{E_2} N_{P(E)} - N_{B(E)}}{\sqrt{\sum_{E_1}^{E_2} N_{P(E)}}} \qquad \textit{Equation 3.5}$$

S is the significance of the photopeak expressed in terms of the standard deviation of the background.

- $N_{P(E)}$ is the number of events in the photopeak at each energy channel
- $N_{B(E)}$ is the number of events in the background at each energy channel
- E_1 and E_2 are the limits of the photopeak

Equation 3.5 is an approximation and does not take into account the shape of the photopeak. Thus the significance will change depending on the limits over which it is calculated. However it may be seen that if the number of photopeak events increases then the significance will increase. Likewise, a greater photofraction will result in a larger number of events above the background and again the significance will be increased. The energy resolution of the detector will determine the number of energy channels over which, the photopeak is distributed. A finer energy resolution will result in the photopeak being spread over a narrower range and hence there will be a smaller contribution due to background noise [66]. Figure 3.11 shows part of a simulated Lunar energy-loss spectrum, for a CsI(Tl) array for which different energy resolutions have been assumed. As may be seen, the features in the spectrum rapidly become blurred and confused as the energy-resolution is degraded. In addition the statistical significance of each emission peak is reduced since the energy-loss peaks are spread over a greater energy range, that is there is a greater background statistical variation associated with the less well defined energy-loss peaks. It may be concluded that an energy resolution of at least 3% at 5MeV, would be very desirable in order to preserve the key features of the lunar emission spectrum.

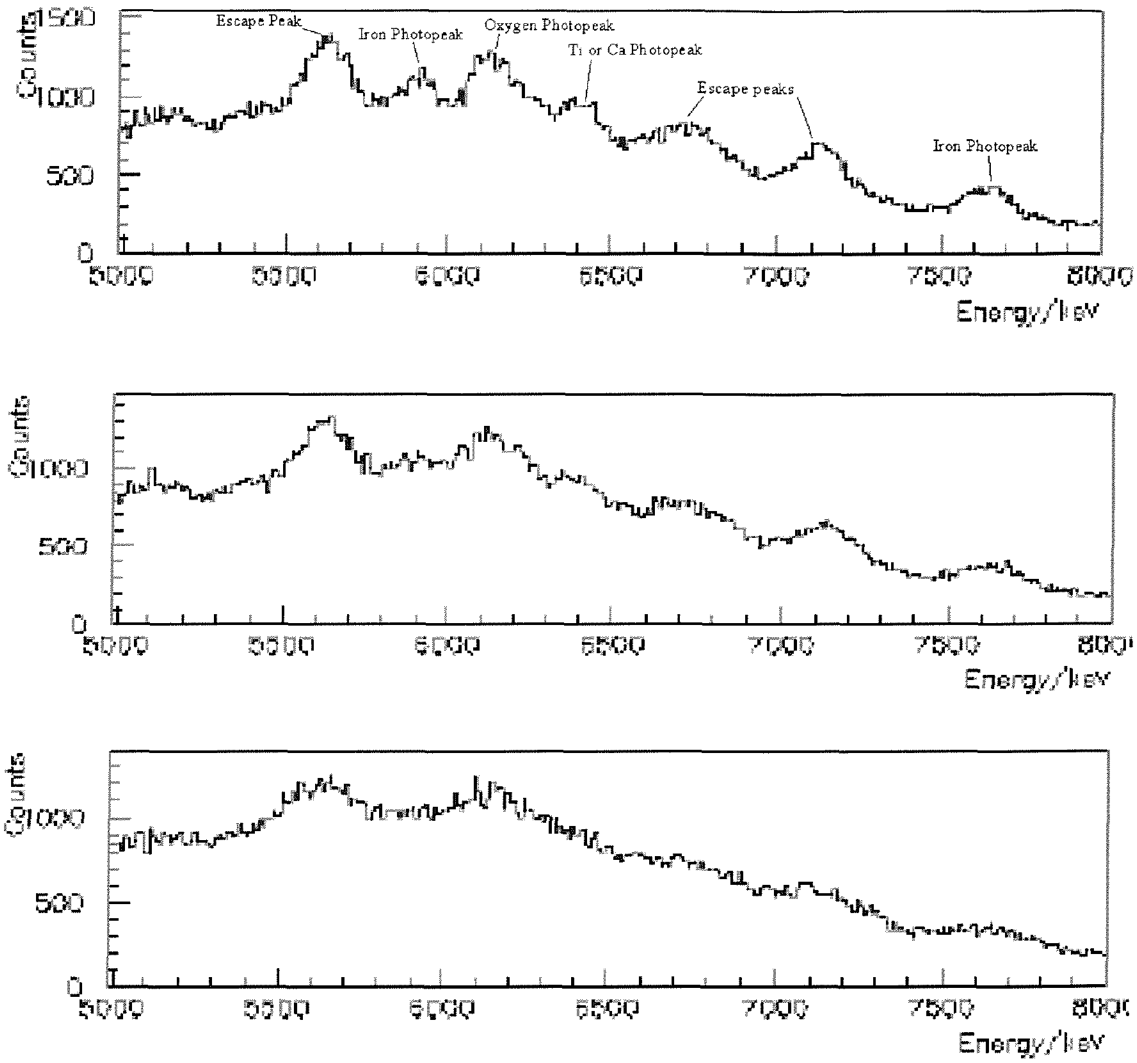

Figure 3.11 Part of the simulated response of a CsI(Tl) array to the Lunar emission spectrum. In descending order the energy resolution is 2.5%, 3% and 4% FWHM at 5MeV

3.4 Comparing the Performance of NaI(Tl)-PMT, BGO-PMT and CsI(Tl)-photodiode Detectors

3.4.1 The calculated gamma-ray Flux

The gamma ray flux emerging from the moon has been calculated by Reedy [26], for each element identified in lunar samples brought back by the Apollo missions. These results were used to derive a simple model for the expected emergent spectrum as shown in Figure 3.12. It may be seen that the lunar spectrum consists of many emission lines from 0 to 10MeV, superimposed on a continuum, which is due to the Compton scattering of photons emerging from depths of up to 0.5m in the crust. It will not be possible for a scintillator spectrometer to resolve every emission line, however, in the energy range from 5 to 10 MeV the lines are more widely spaced and could be resolved using a spectrometer with an energy resolution of less than 3%FWHM at 5MeV. The gamma ray lines in this region include silicon, oxygen and iron, which are important when evaluating the composition of a planetary surface.

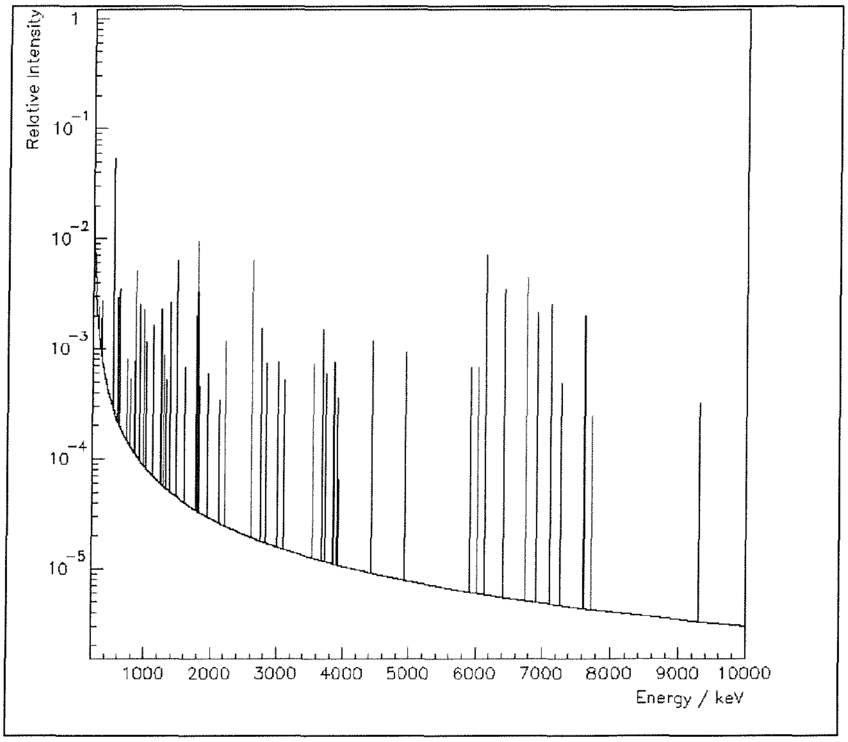

Figure 3.12 The Derived Lunar Spectrum Used to Determine the Response of the CsI(Tl)-photodiode array

3.4.2 Comparison of NaI(Tl)-PMT, BGO-PMT and CsI(Tl)-phtodiode spectrometers

Due to the strict mass budgets imposed on instruments designed for recent planetary missions, a future GRS should have a mass of less than ~10kg, consume less than a few watts of power and have dimensions that can be easily incorporated onto the spacecraft. The Apollo spectrometer had a total mass budget of 9.7kg of which, the GRS itself weighed only 3.3kg. Two thirds of the mass budget consisted of a thermal shield weighing 3.3kg and the secondary electronics and power supply weighing 3.2kg [45]. The total mass of NaI(Tl) in the GRS was only 1.2kg the remaining 2kg being taken up by an anti-coincidence shield, photomultipliers and front-end electronics. The recent Lunar Prospector spectrometer had a mass budget of 8.6 kg of which the total mass of the BGO crystal was 2.1kg [67]. Again, an appreciable proportion of the instrument mass is “lost” due to the need for an anti-coincidence shield and photomultiplier tubes.

To make a comparison between the performance of a possible CsI(Tl) GRS with the Lunar Prospector GRS and a similar mass NaI(Tl) detector, it is necessary to estimate the available mass of CsI(Tl) that may be used and stay within the 8.6kg mass allowance. The exact detector mass availability is impossible to calculate without doing a full design for an orbiting spectrometer. However, it is possible to make an estimate of the available mass and hence make a general comparison between the performance of a CsI(Tl) spectrometer, a NaI(Tl)-PMT detector and a BGO-PMT detector.

A CsI(Tl) array does not require any PMT's and may also not require an anti-coincidence shield as will be explained in chapter 4, therefore a greater proportion of the instrument mass could be in the crystal. If it is determined that an anti-coincidence shield is in fact needed for the spectrometer, it should be possible to construct a veto counter with a mass of approximately 0.75kg. It is therefore fair to assume that a future CsI(Tl) spectrometer with a total mass of 9kg would have more than 4kg of CsI(Tl) crystal. The simulated response from 4kg of CsI(Tl) with photodiode readout, 2.15kg of cooled BGO and 2.15kg NaI(Tl) both with PMT readout is shown in Figure 3.13. A representative energy resolution has been applied to each simulated spectrum.

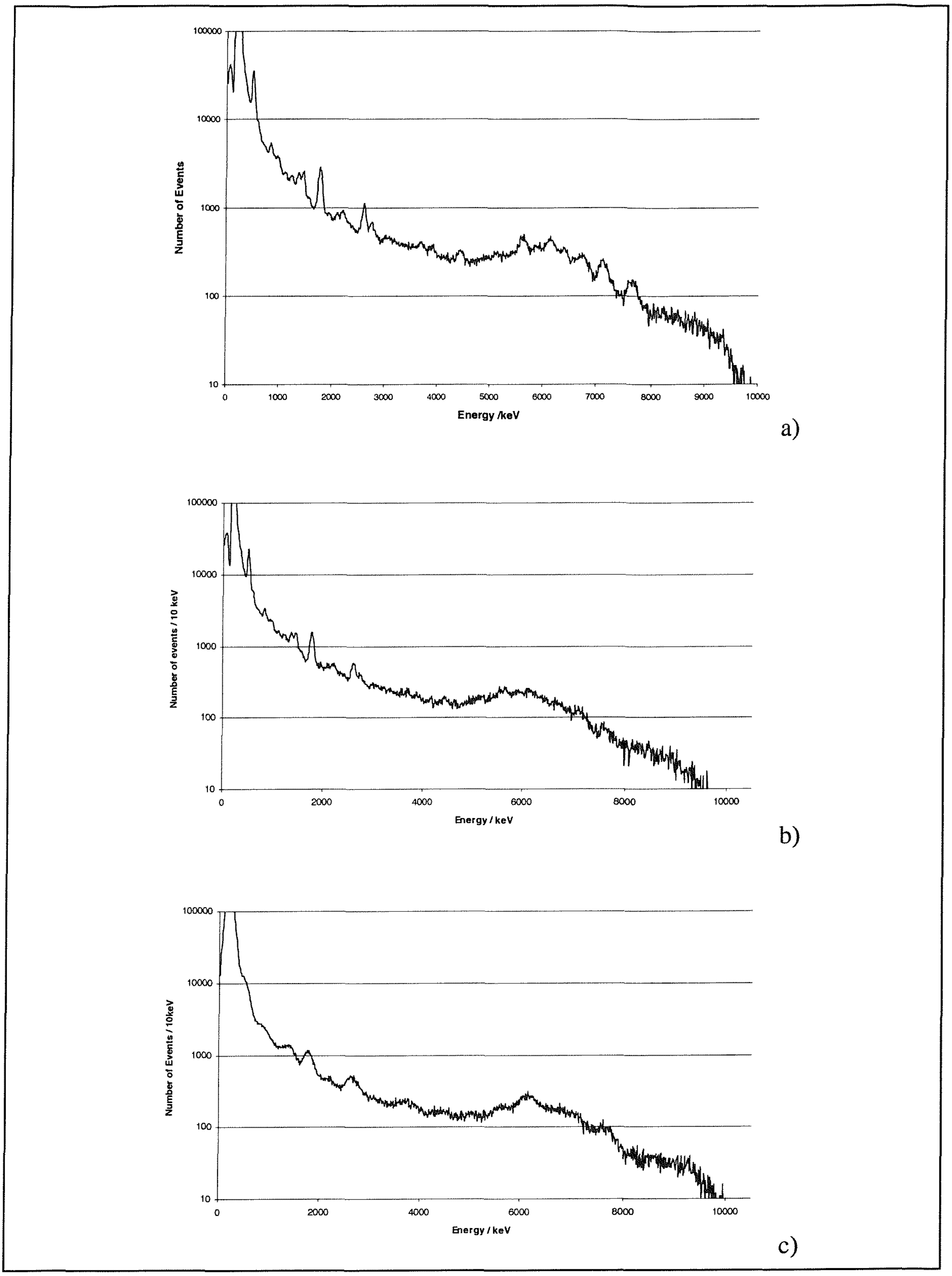

Figure 3.13 The simulated response of a) 4kg of CsI(Tl), b)2.15kg of NaI(Tl) and c)2.15kg of cooled BGO, to the lunar spectrum.

It may be seen that the features related to the principal emission lines are more clearly visible in the CsI(Tl) energy-loss spectrum. This can be attributed to the better energy-resolution achievable with a CsI(Tl) array combined with the additional mass of sensitive material. These spectra do not include the effect of background sources such as spacecraft activation or high-energy particles. However, it may be said that for a similar spacecraft configuration, the CsI(Tl) detector will have a greater sensitivity for the detection of lunar emission lines.

3.5 Conclusion

When considering the choice of scintillator gamma-ray spectrometer for remote geochemical analysis it has been shown that CsI(Tl)-photodiode arrays have the potential to provide a greater sensitivity than other currently available scintillator detectors with an equivalent payload mass. The high scintillation efficiency of CsI(Tl) combined with the high quantum efficiency of the photodiodes gives CsI(Tl) a significantly better energy-resolution in the energy region above 2MeV. Also, CsI(Tl) spectrometers are able to provide a larger ratio of the mass of the detector in the sensitive medium, compared to equivalent payload mass NaI(Tl) detectors, since the CsI(Tl) detector uses photodiodes to detect the scintillation light, instead of photomultiplier tubes. Thus an 8.6kg CsI(Tl) spectrometer would give significant improvements in the sensitivity of an orbiting spectrometer for remote geochemical analysis. A CsI(Tl) array also has the advantage of being pixelated which will allow the use of observation techniques such as pair spectrometry and may also help in the reduction of background due to activation of the spacecraft. Finally, CsI(Tl) arrays only require a low voltage and power supply to operate, which is preferential when considering such a detector for inclusion as part of the payload of an orbiting spacecraft.

Chapter4

4 Design, Construction and Testing of a CsI(Tl)-photodiode Array

4.1 Introduction

A 7 element, prototype, CsI(Tl)-phtodiode array has been constructed for testing in the laboratory to demonstrate the advantages that may be gained using such a design, compared with a NaI(Tl) or BGO spectrometer. This chapter describes the design, construction and laboratory testing of the array and compares the performance of the array with that of a 2" NaI(Tl)-PMT detector. Finally, the performance of a 61-element array is simulated, based on the results from the prototype array, and the various methods of analysis are discussed.

4.2 The Design of a 7-Element CsI(Tl)-photodiode Detector

When designing a CsI(Tl) array, it is important to optimise the length and across flats dimensions of the crystals to get the greatest sensitivity from the detector. For a given mass of scintillator, the volume of the sensitive medium will be constant but the geometry can be altered, to maximise the photofraction and hence increase the sensitivity. Considerations include the length of crystal required to attenuate 1 to 10MeV photons, the pixelation of the crystals to provide information about the energy and position of the interactions for data analysis, and the ratio of length to across flats dimension that can be accommodated whilst maintaining a sufficient energy resolution. The energy resolution is the dominant factor affecting the signal to noise ratio and therefore it is important that a sufficient resolution be maintained in all designs. The optimisation of a gamma ray spectrometer is not a simple problem and therefore GEANT Monte-Carlo computer simulations have been used to aid in the design of the detector.

The flux incident on an orbiting gamma-ray spectrometer is assumed to originate from an infinite plane and the detector is assumed to be observing the surface from a three axis stabilised spacecraft so the length of the detector crystals are always aligned perpendicular to the surface of the planet. Therefore the altitude of the detector above this plane does not affect the flux incident on the detector but will change the area on the surface from which the recorded flux originates. This will result in a flux distribution, incident on the detector as shown previously in Figure 3.8.

The response of 3 CsI(Tl) detector configurations, each having a mass of 4kg, but with a different diameter to depth ratio, were simulated using mono-energetic gamma rays at 4.44 and 6.129MeV, which are two of the emission lines from Oxygen. The relative number of detected photons and the photofractions for the three detectors is shown in Figure 4.1, from which it may be seen that a thin detector having a large area will have a greater number of energy-loss events but a smaller photofraction. Thus the natural conclusion is that the detector must be as deep as possible, to maximise the photofraction and hence allow the identification and quantification of the emission lines, incident on the detector.

To characterise the age and temperature of formation of a planetary surface it is necessary to determine the ratio of the naturally occurring radionuclides K, U and Th and elements such as Fe, Si and O. The emission lines from K, U and Th lie in the energy range from 0 to 2.6MeV whilst the activation lines from Fe, Si and O have energies up to 8MeV. Therefore, a gamma-ray spectrometer must provide a sufficient sensitivity over a wide range of energy. At energies up to a few MeV, the energy resolution of a CsI(Tl) photodiode detector is dominated by the light-collection efficiency and hence, to improve the resolution, the light collection must be maximised without increasing the noise contribution form the photodiode, which is dependant on its area. To maximise the light collection efficiency of a CsI(Tl)-phtodiode detector requires the use of a modest aspect ratio, that is the length to cross-sectional width of the crystal. This conclusion is contrary to the requirement of maximising the detector photofraction, which requires the detector elements to be as long as possible. A compromise must therefore be reached for which the photofraction of the detector is sufficient whilst maintaining a good light-collection efficiency and hence energy-resolution. At 5MeV, a 3" NaI(Tl)-PMT spectrometer has an energy resolution of approximately 3.5% FWHM. Therefore this should be the minimum requirement for a CsI(Tl)-photodiode array and if possible the energy resolution should be less than 3%.

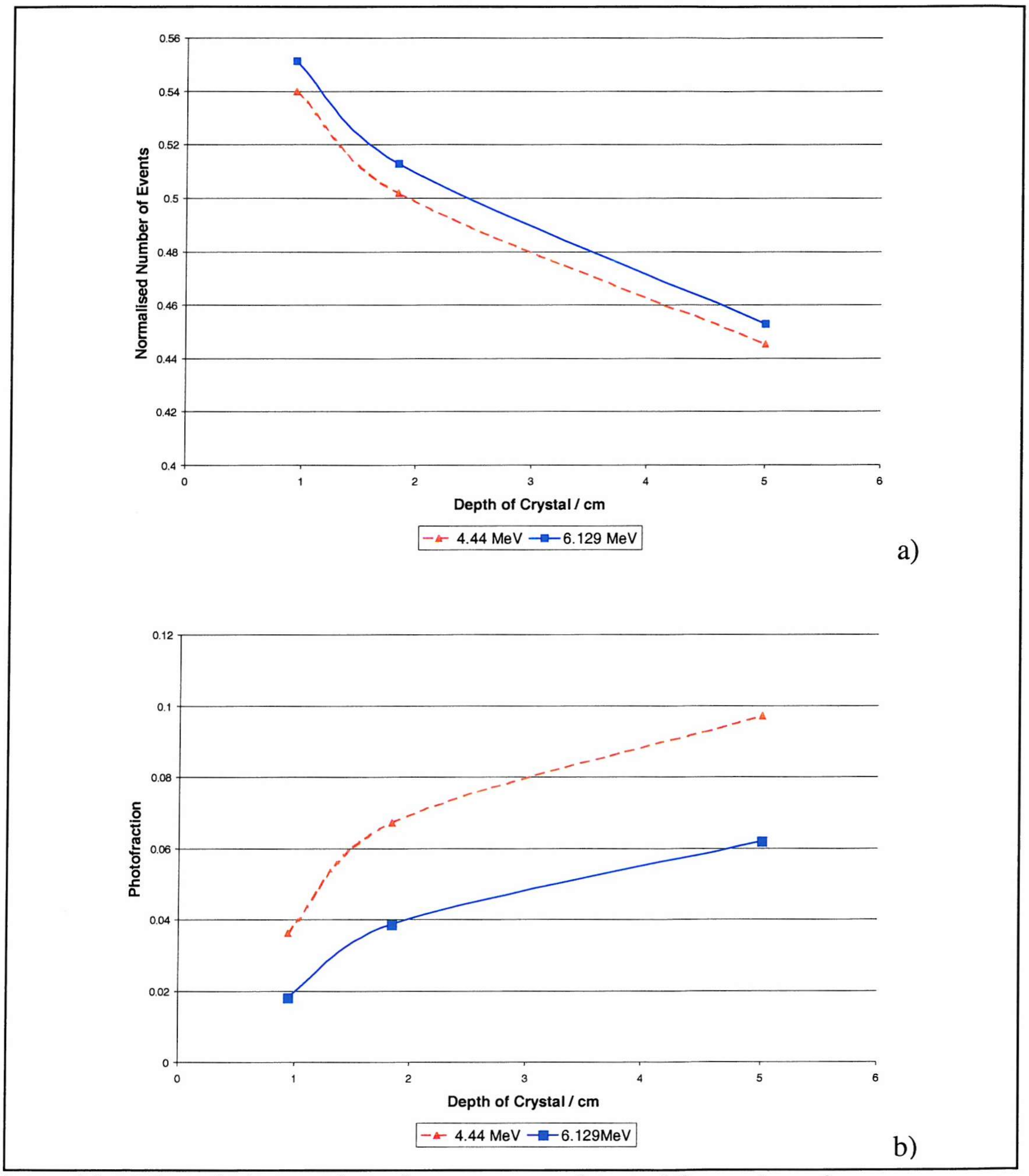

Figure 4.1 a)The relative number of gamma-rays detected for a given detector geometry. b)The photofraction for a given geometry

4.2.1 Designing the Detector for Triple Coincidence Spectrometry

At energies above 1.022MeV it is possible for a photon to interact with the coulomb field around an atom and convert from energy to matter in the process of pair production. The photon disappears creating a positron and electron which have he combined energy of the photon minus the rest mass of the particles which is 1.022MeV. The electron and positron deposit their kinetic energy, in the scintillator crystal, until the positron annihilates with another electron releasing the rest mass of 1.022MeV. The two gamma rays produced each have 0.511MeV and travel in opposite directions. If these photons escape the initial crystal of interaction and are captured in two of the surrounding crystals, the result is a fairly unique signature that is very unlikely to be due to Compton scattered events or partial energy loss. Thus pair spectrometry can be a powerful tool for reducing the Compton scattered component, due to the detector, for gamma-ray spectra above 1.022MeV. Pair spectrometry has been successfully used for mineral analysis by neutron activation spectroscopy using an array of 3"NaI(Tl) detectors [68]. However, a hexagonal array of CsI(Tl) elements may be more suitable for this type of analysis since each crystal is totally enclosed along the length by 6 other crystals and hence the 511keV photons are more likely to be detected.

The pair spectrometry technique records only those events in which there are three energy-loss events in coincidence, two of which are 511keV. This is illustrated in Figure 4.2. The advantage of recording only those events showing the triple coincidence signature is that it is very likely that the full energy of the incident gamma-ray has been recorded and it is highly unlikely that the event is due to a complex Compton-scattering interaction. Thus the Compton-scattered component of the energy-loss spectrum is virtually eliminated resulting in a spectrum that is more interpretable. The disadvantage of this method of analysis is the inefficiency of the process and the rejection of many full energy-loss events. Thus this method of analysis is suitable for clarifying energy-loss spectra when the counting statistics are particularly good. Figure 4.3 shows a simulated energy-loss spectrum from a 5MeV emission line with three different types of analysis. It may be seen that the triple coincidence spectrum has virtually no Compton or escape peak component but the photopeak is between 1 and 2 orders of magnitude smaller than that for the simple summation spectrum.

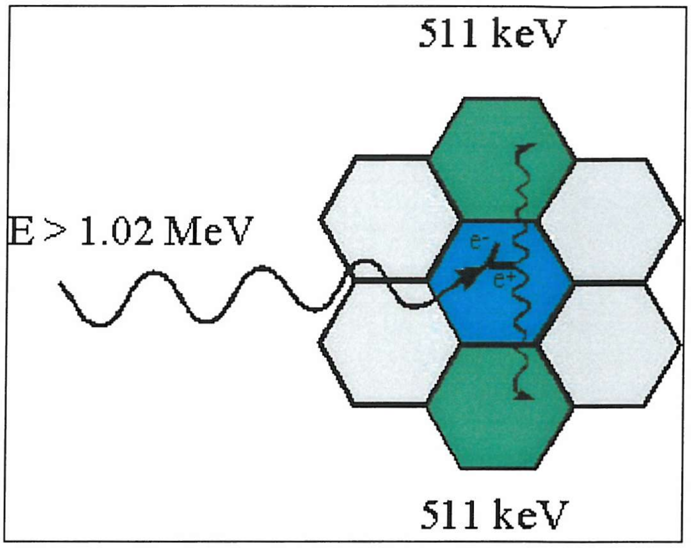

Figure 4.2 An example of a triple coincidence pair production event in a pixelated array

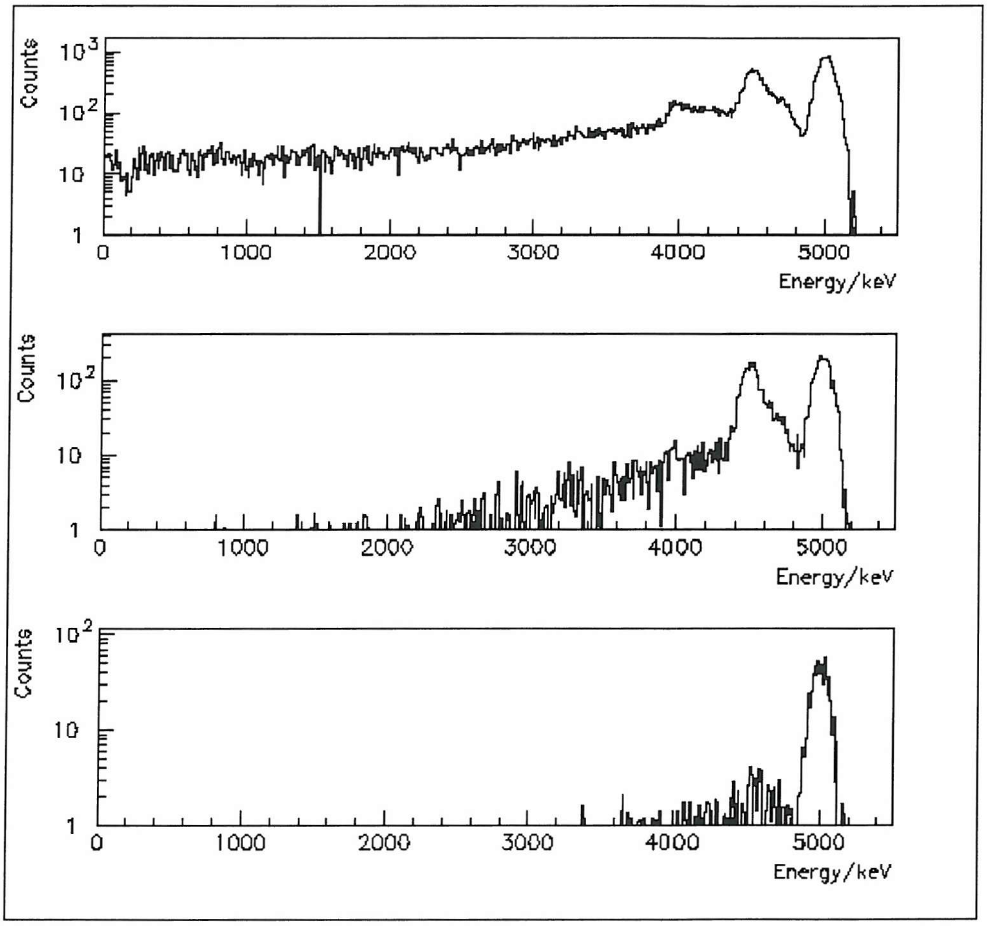

Figure 4.3 The simulated energy-loss spectra from a 5MeV emission line observed by a 2kg, 19 element CsI(Tl) array. a) The simple summation spectrum, b) the double coincidence spectrum, c) the triple coincidence spectrum.

To improve the efficiency of the pair spectrometry process it may be possible to use a technique called incident pixel reconstruction (IPR) [69]. This technique assumes that the largest energy deposit occurs in the incident pixel and all other deposits are due to secondary particles or photons. The accuracy of this assumption varies depending on the incident photon energy. For CsI(Tl) the assumption has been shown to be correct, over 90% of the time in the energy regions below 300keV and above 2MeV, and over 70% for the region between these energies. Using IPR instead of triple coincidence removes the restriction that two of the energy-loss events must have an energy of 511keV. Instead the largest energy deposit is subtracted from the total. If the remainder equals 1022keV then the event is included in the spectrum as shown in Figure 4.4. Therefore, events where the 511keV photons scatter between more than one crystal, can also be included in the spectrum, thus increasing the efficiency. However this method will result in a higher possibility of accidentally including partial energy-loss events.

For a triple coincidence event to be recorded:

- The incident photon must interact by pair production
- The subsequent electron and positron must deposit their KE in the same crystal
- The two gamma-rays produced when the positron decays must escape the incident crystal
- Both 511keV gamma rays must deposit their energy in the surrounding crystals.

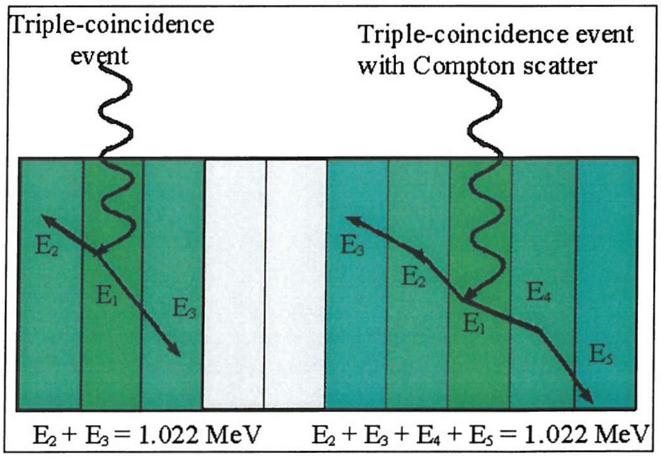

Figure 4.4 The types of interaction included when performing IPR pair spectrometry

To maximise the probability of the 511keV annihilation photons escaping the incident crystal, it is desirable to make the array as finely pixelated as possible, provided there is still a high probability of recording all of the electron and positron energy in the incident crystal. Unfortunately, making a very fine pitch array with a reasonable attenuation length has detrimental effects on the energy resolution, because of the high aspect ratio. In addition, a very fine pitch array would require more channels of electronics to accommodate the increase in the number of pixels. A compromise is therefore required in which the energy resolution is kept below 3% FWHM at 5Mev, whilst still maintaining a pair spectrometry capability.

4.3 Construction of a 7 Element Prototype Detector Array

CsI(Tl) is easily machined into complex shapes and is only slightly hygroscopic, which makes the material ideally suited to the construction of detector arrays. The typical structure of a CsI(Tl) photodiode-array is shown in Figure 4.5. It may be seen that the individual read-out elements (photodiode and preamplifier) form only a small fraction of the overall detector volume. Thus the detector can be made very compact and rugged which is important for a spacecraft mounted instrument. The IBIS gamma ray imaging detector, onboard the INTEGRAL gamma ray space telescope, due for launch in 2001, consists of a large CsI(Tl)-photodiode array in conjunction with a coded mask [70]. During the phase-A design study of the telescope, the methods of preparation and assembly of these elements were investigated, to optimise the light output from each element and hence improve the energy resolution and low energy threshold of the detector [71]. The light collection efficiency of hexagonal 1cm^2 cross-section bars, with lengths varying between 1 and 6cm were compared to that obtained using bars with square and circular cross-sections. The tests showed that, cylindrical bars offered a slight advantage over hexagonal bars, however, since it is not practical to make the array out of circular cross-section crystals, hexagonal cross-section elements were chosen.

In view of the points discussed in the previous section, the choice of the crystal dimension will be determined by a compromise between the energy resolution, the stopping efficiency and the pixelation of the detector. As stated, the energy resolution is the most important factor and therefore the choice of dimensions will be those that will not result in the energy resolution deteriorating below 3% FWHM at 5MeV. Preliminary tests were performed on individual CsI(Tl) crystals with a hexagonal cross-section of 2cm across-flats dimension and lengths of 5 and 7cm. It was found that using the 7cm long crystals it was difficult to achieve the required energy resolution and hence 5cm long crystals were chosen. The across-flats dimension of 2cm was chosen since this is approximately equivalent to the attenuation length of a 511keV photon in CsI(Tl). It may be possible to make the across flats dimension larger to allow a longer crystal to be constructed. However, this will be at the expense of the sensitivity of the spectrometer when operating in pair spectrometer mode.

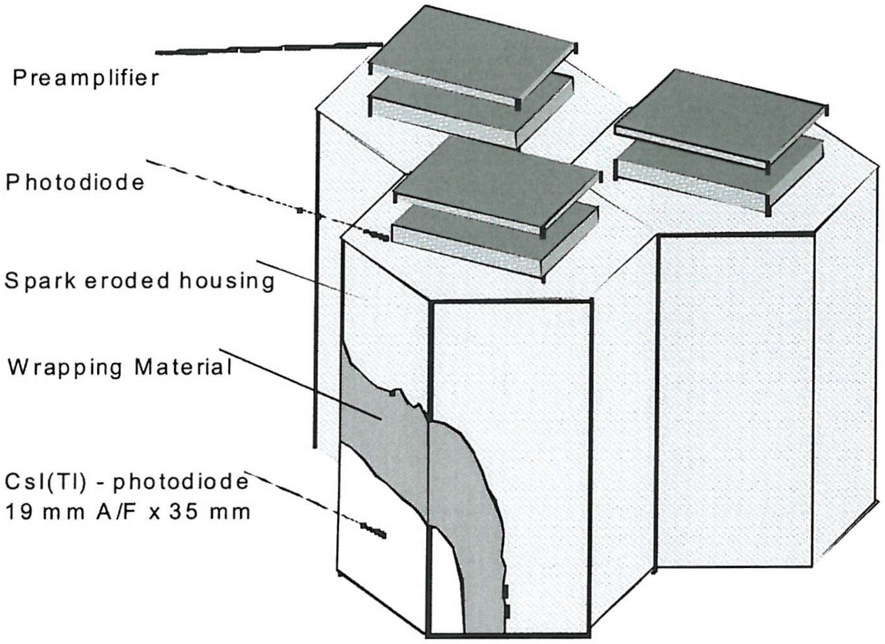

Figure 4.5 The design of a CsI(Tl)-photodiode element

The scintillator surface finish and optical wrapping materials used for the spectrometer are the same as those recommended for use in the INTEGRAL phase A laboratory crystals. All the surfaces are mirror polished to give specular reflection, except the end furthest from the photodiode, which is roughened to provide diffuse scattering. The crystals are wrapped with two layers of Tyvek® followed by several layers of P.T.F.E. tape. A Hamamatsu S3590-01 photodiode was optically bonded to the scintillator using Cargille melt mount, which has a melting point of 60°C and a refractive index of 1.704.

The photodiodes are connected to Amptek PAC L3 low noise charge amplifiers, which are also contained within the detector housing to reduce any induced noise on the signal. Using a low noise pre-amplifier means that the shaping time can be increased to 6μs which increases the light collection for a CsI(Tl) crystal without the leakage current increasing too dramatically. The 7-element prototype gamma-ray is shown schematically in Figure 4.6. Each channel had its own shaping amplifier and discriminator controlled by a logic circuit that enabled every channel to be read out when any one channel exceed the set discrimination level. The 7 channels were read into a 1MHz, 16 bit ADC card, which was triggered by a trigger channel from the logic circuit. Note a 16 bit ADC card is required to overcome the differential nonlinearity that is inherent in fast, successive approximation, ADC cards. All data processing and analysis was done offline using software routines to discriminate between different types of events. A spectrometer built for use onboard an orbiting spacecraft would almost certainly have some selection procedures built into the hardware to reduce the amount of data to be transmitted back to Earth.

The principal aim of the prototype detector is to quantify the realistically achievable energy resolution when using 5cm long by 2cm across flats hexagonal crystals. The prototype has been used to test the energy resolution of individual crystals, the energy resolution of the sum spectrum, data deconvolution techniques and different methods of analysis.

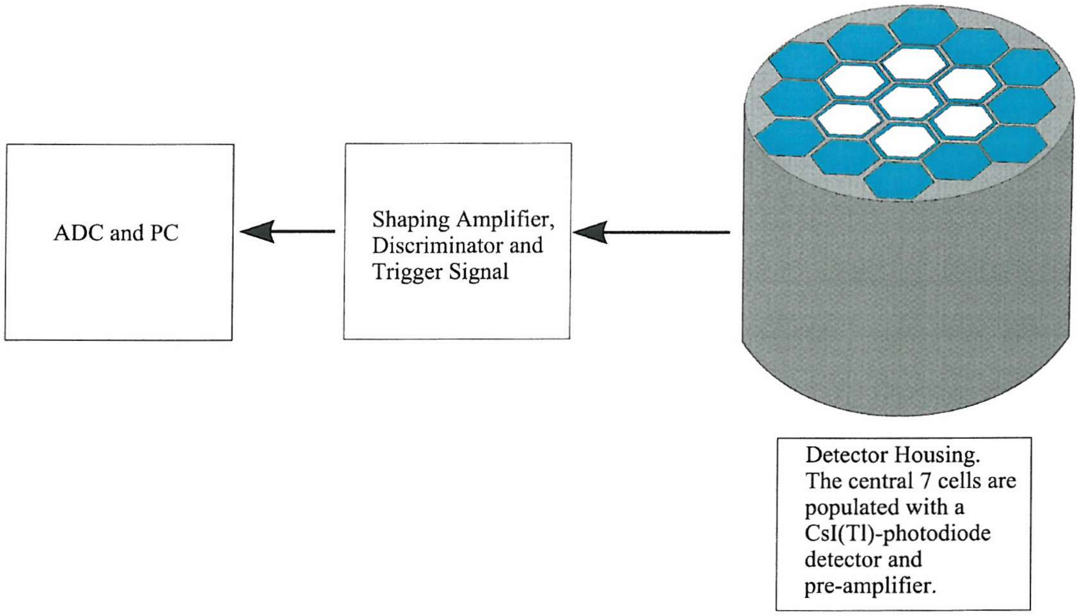

Figure 4.6 A schematic of the prototype 7 element array

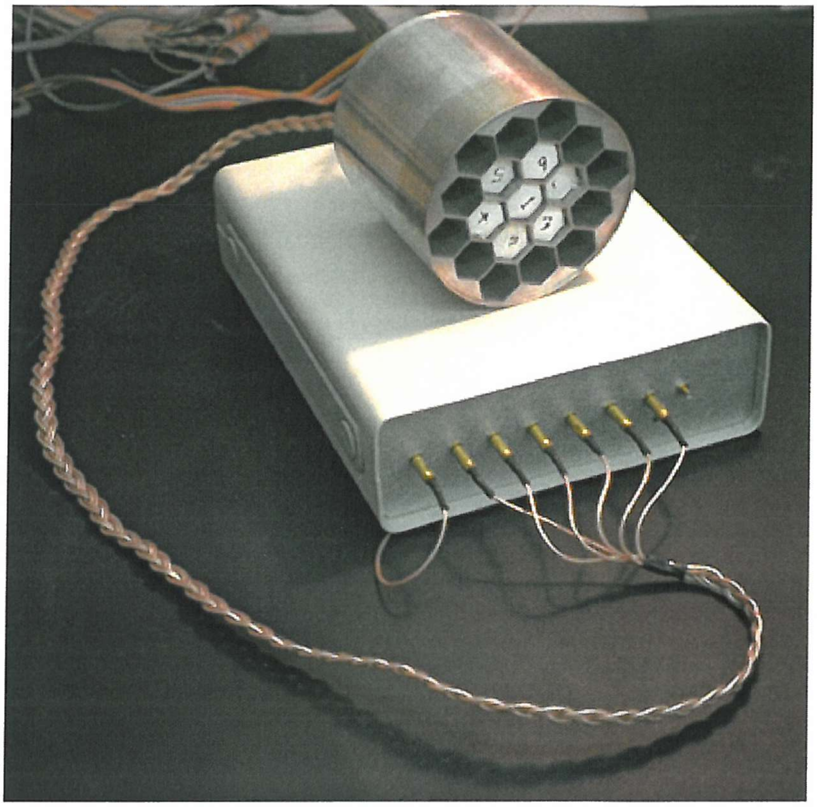

Figure 4.7 The prototype detector

4.4 Testing of the 7 Element Array

The energy resolution of each element in the detector array and the overall sum spectrum were measured using standard laboratory sources. The sources provide calibration points up to the 1.332MeV line of Co^{60} as shown in Table 4.1. There is a slight difference in the energy resolution of the individual elements due to slight variations in the crystals, variations in the construction or electronic effects. In reality it is not possible to produce a large number of optimised detectors with identical performance and therefore the energy resolution of the sum of all the crystals will be the sum of the squares of the energy resolution of the individual elements. The performance of the array is discussed in section 4.4.1.

An example of a simple sum energy-loss spectrum of a Na^{22} source is shown Figure 4.8. Note the low energy threshold was set just below 511keV since there is very little information to be gained from the spectrum below this energy when observing neutron activated materials.

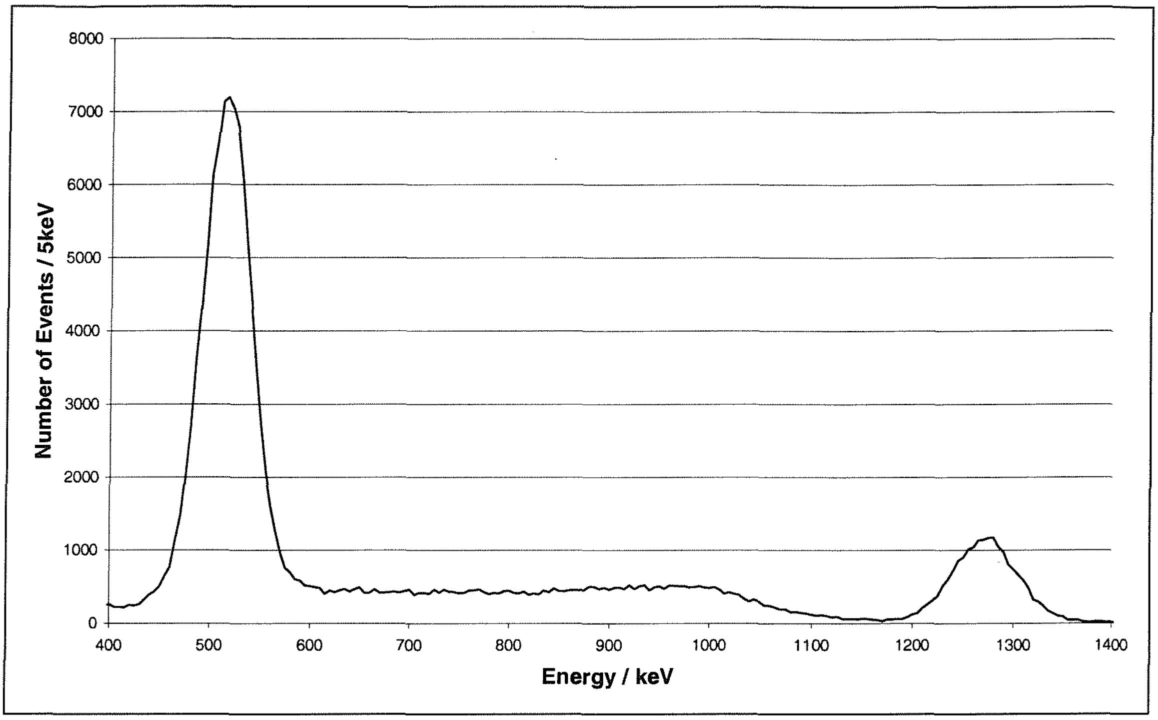

Figure 4.8 The calibrated spectrum from the 7 element array irradiated by a Na^{22} *source. All 7 channels are read-out when any channel rises above the threshold. For each triggered event the energy deposits in all 7 channels are calibrated, summed and added to the spectrum.*

4.4.1 Tests at High Energy using an Americium-Beryllium Neutron Source

The standard laboratory gamma ray sources can be used to calibrate the gamma ray detector up to 1.332MeV, which is one of the emission lines from Co^{60}. Yttrium will allow testing up to 1.84MeV but has a short half-life of 107 days and therefore is not commonly available. To measure the energy resolution at energies above 2MeV, an americium-beryllium neutron source was used, the reaction for which is shown in Equation 4.1.

$$ {}_{2}^{4}\alpha + {}_{4}^{9}Be = {}_{6}^{12}C^{*} + {}_{0}^{1}n \qquad \textit{Equation 4.1} $$

Alpha particles are emitted by the americium source, which collide with the beryllium target forming an excited C^{13} atom. The C^{13} atom decays by emitting a neutron, sharing the energy of the interaction between the daughter C^{12} nucleus and the neutron. The Q value of the reaction is 5.41MeV and the energy of the alpha particle at the point of emission from the americium is 5.6MeV, therefore the maximum neutron energy is 11MeV. Normally, the energy of the reaction is shared between the neutron and the carbon daughter atom resulting in the neutron spectrum shown in Figure 4.9. The carbon atom is in an excited state and will decay via the emission of a 4.44MeV gamma ray. In addition the neutron source is situated in a water tank so the neutrons are attenuated by elastic collisions with hydrogen atoms, thermalising within a few centimetres of the source. Eventually, the hydrogen atoms will capture the neutrons, which results in an excited atom that decays with the emission of a characteristic 2.22MeV gamma ray. The gamma ray spectrum emerging from the neutron tank, recorded by a cooled germanium spectrometer, is shown in Figure 4.10. Clearly visible are the 2.22 and 4.44MeV emission lines and their associated escape peaks superimposed on a continuum, which is due to Compton scattering of photons, before they emerge from the water tank and in the detector itself. It may be noted that the 4.44MeV emission line from the excited carbon atoms is Doppler broadened due to the total energy of the reaction being shared between the carbon atom and the resultant neutron. From the width of the 4.44MeV peak the velocity of the carbon atom can be calculated to be approximately 2.5% of the speed of light. The 2.22MeV and 4.44MeV gamma ray lines can be used to characterise the energy resolution of the gamma ray detector at energies not normally available in a laboratory situation, providing an allowance is made for the Doppler broadening of the 4.44MeV gamma ray line.

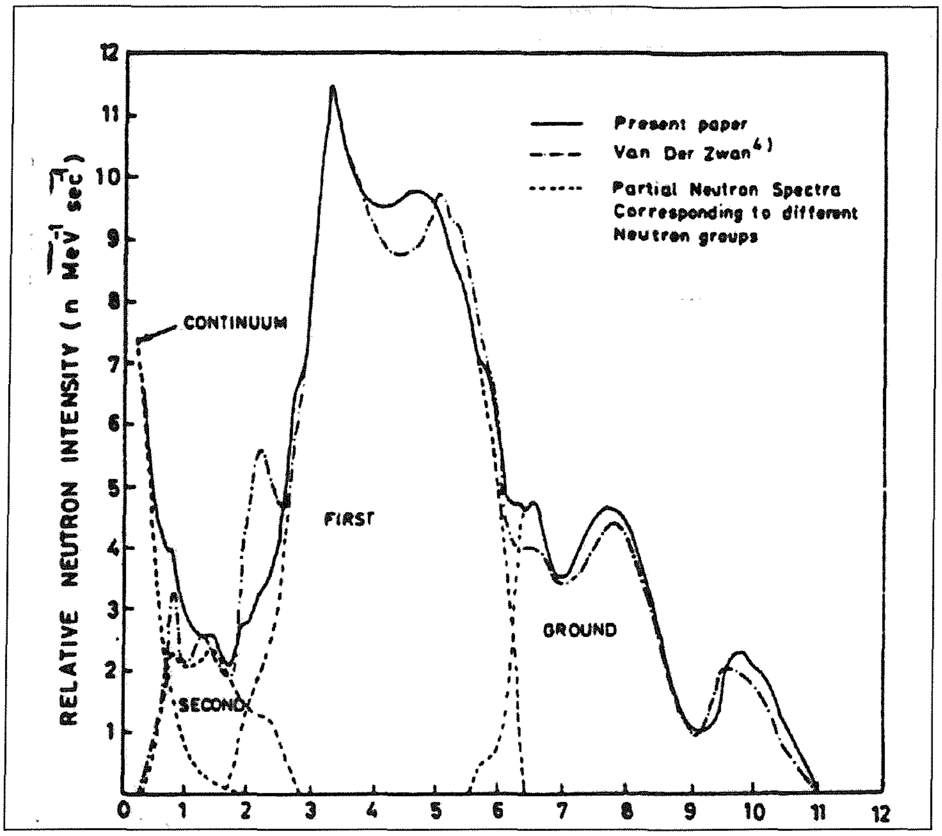

Figure 4.9 The Neutron spectrum from an Am-Be neutron source [72]

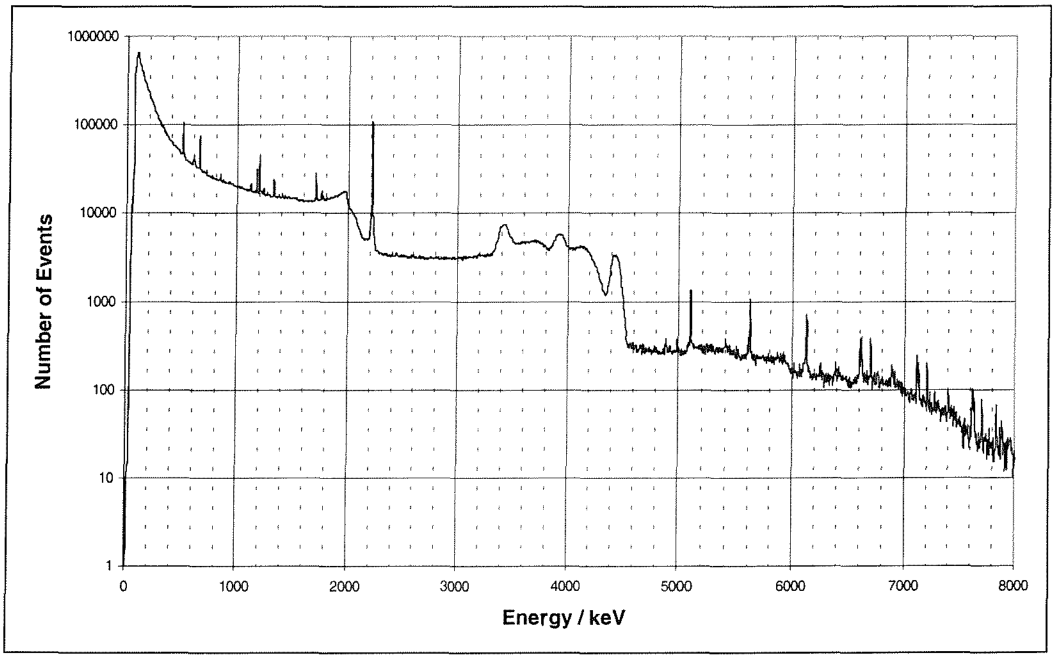

Figure 4.10 The energy-loss spectrum from a cooled germanium spectrometer observing the gamma spectrum radiating from the neutron source

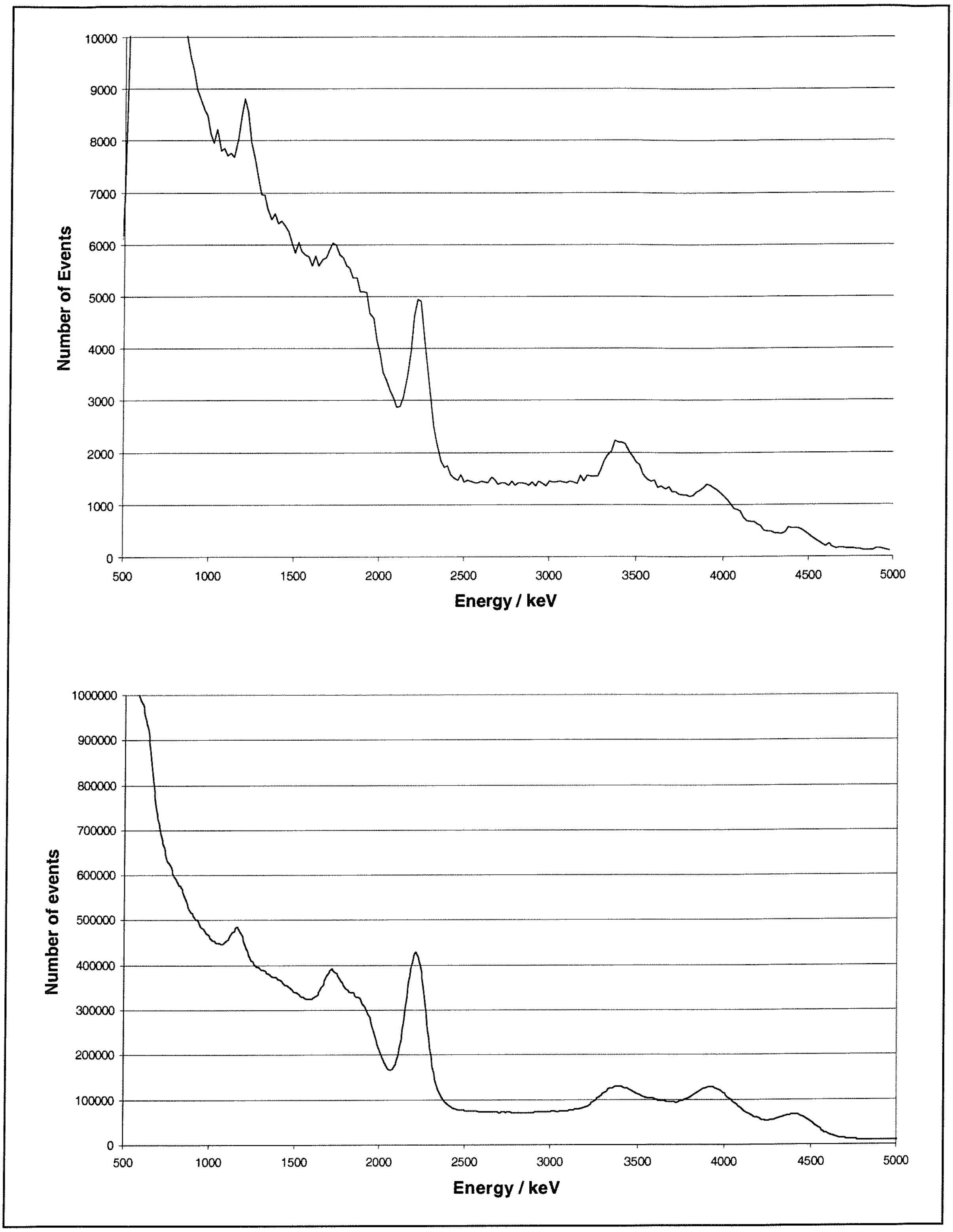

Figure 4.11 The energy-loss spectrum from a)The 7 element CsI(Tl) –photodiode array b) 2" NaI(Tl)-PMT spectrometer, being irradiated by the flux from an Am-Be neutron source in a water tank

The energy-loss spectrum from the 7-element array observing the flux radiating from the neutron source is shown in Figure 4.11. Clearly visible are the 2.22MeV and 4.44MeV lines and the associated escape peaks. Comparing the energy-loss spectrum from the 7 element array, with that of a 2" NaI(Tl)-PMT detector also shown in Figure 4.11, it may be seen that the CsI(Tl) detector has a better energy resolution at 3.418 and 4.44MeV. The FWHM has been calculated for the 2.22, 3.418 and 4.44MeV energy-loss peaks, for the 7 element array and for the NaI(Tl) detector, by using a constrained maximum-likelihood fitting routine. The program assumes the peak has a Gaussian shape and is sitting on a linear background with the shape y=mx+c. The FWHM for each peak is shown in Table 4.1.

Gamma-ray Energy (keV)	Single CsI(Tl) Pixel FWHM (%)	7 Element CsI(Tl) Array FWHM (%)	2” NaI(Tl)-PMT FWHM (%)
511	11.05	11.45	8.19
662	9.95	10.0	6.6
1174	6.09	6.2	5
1275	5.7	5.8	5
1332	5.56	5.6	5
2220	4.26	4.4	4.33
3418	2.98	3.2	3.6
3929	2.6	2.9	3.6
4440	2.4	2.9	3.5

Table 4.1 Energy resolution of a CsI(Tl) array and a 2"NaI(Tl)_PMT detector

The crystal used to populate the central pixel in the 7 element array was chosen to be the one that had the finest energy-resolution. The energy-resolution of the central crystal, the array when operating in simple summation mode and, for comparison, a standard 2” NaI(Tl)-PMT detector are shown in Table 4.1. It may be seen that the resolution of the CsI(Tl)-array sum spectrum is not as good as that of the central pixel due to the variation in the energy-resolution of the 7 crystals. At 511keV the energy resolution of 6 out of 7 of the pixels lay between 11.05 and 12.3% FWHM. The seventh crystal had a slightly poorer energy resolution of 13% FWHM. For larger arrays, the variation in the energy resolution will depend on the quality of manufacture of each pixel. Factors that will affect the performance are, the crystal uniformity, the quality of surface preparation, wrapping materials and bonding of the crystal to the photodiode. However, it would be expected that for an orbiting spacecraft instrument the energy resolution variation would be no worse than demonstrated for this array.

4.4.2 The Energy Resolution Calibration Curve

Measurements made with the 7-element array, shown in Table 4.1, provide the energy resolution of the detector over a 4MeV range of energy. However, in order to model the response of a larger 61 element array accurately, it is necessary to calculate the energy resolution of the detector at all energies in the range of observation. To do this, it was necessary to calculate a continuous function that best fits the measured energy-resolution and hence predicts the energy-resolution of the detector at all other energies.

Equation 3.4 can be used to predict the energy resolution of a gamma-ray spectrometer with three variable parameters: the electronic noise, the charge conversion efficiency and the intrinsic resolution. Figure 4.12 shows a maximum-likelihood fit applied to the measured energy-resolution data to predict the resolution of the 7-element array. For comparison, the energy resolution of a 2" NaI(Tl)-PMT detector is also shown. Clearly the CsI(Tl) detector offers an energy-resolution advantage over the NaI(Tl) detector, in the energy range above 2MeV. This is particularly significant when applied to complex spectra such as the lunar emission spectrum as demonstrated in Chapter 3

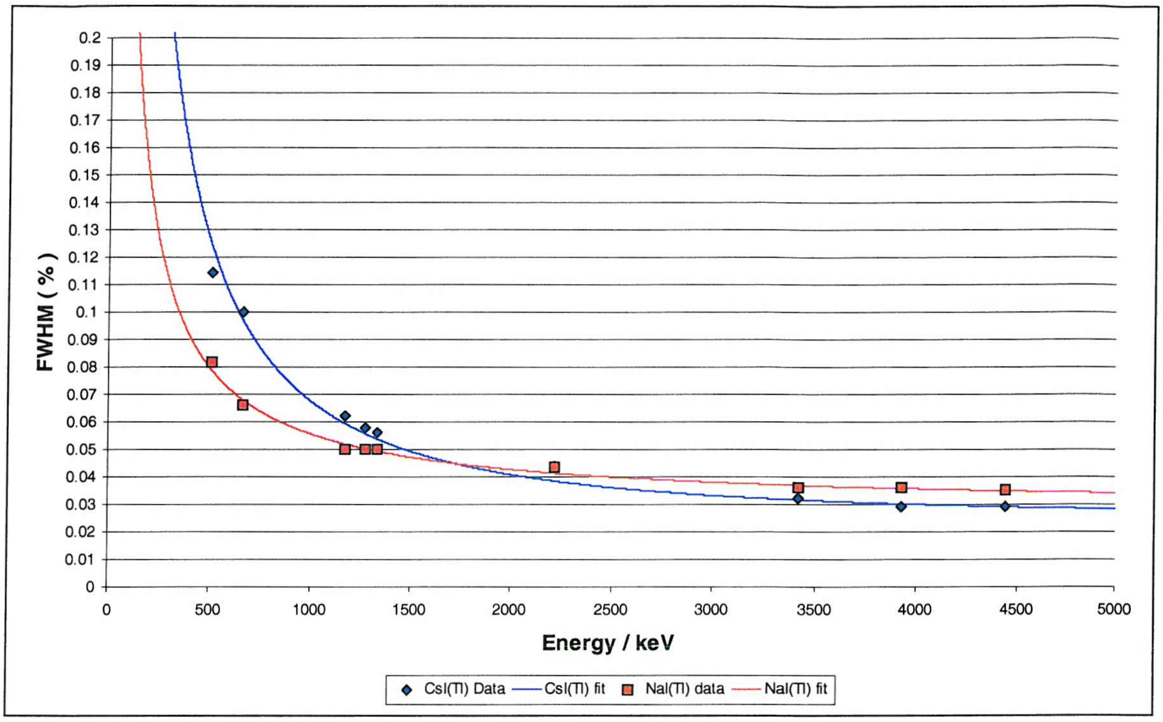

Figure 4.12 The measured energy resolution of the 7-element array and a 2" NaI(Tl) detector.

It may be seen that a NaI(Tl) detector has a better energy resolution, than the 7-element array, below 1.75MeV. This is due to the NaI(Tl)-PMT detector having very low noise characteristics compared to the CsI(Tl) detector. However, the superior light output of the CsI(Tl) crystal and the quantum efficiency of the photodiode results in the CsI(Tl) array having a finer energy resolution than the NaI(Tl) detector at energies above 1.75MeV. This has a significant effect in the application of remote geochemical analysis. It may be noted that for single 1cm^3 CsI(Tl)-photodiode detectors, it is possible to improve the energy resolution so that the crossover point is below 662keV [58]. These detectors are too small for consideration in the current application where a good detection efficiency is required up to 10MeV, but show that if necessary, smaller, finer energy-resolution detectors may be used.

4.5 The Simulated Response of a 61 Element Array

The design and construction of the 7-element array has proved that, using CsI(Tl) crystals 5cm long by 2cm across flats, it is possible to achieve an energy resolution, that is a significant improvement on the energy resolution that is achievable using a NaI(Tl)-PMT spectrometer. This section considers the mass of CsI(Tl) that may be reasonably incorporated into an 8.6kg GRS, which is the mass of the Lunar Prospector GRS, and calculates the response of a 61 element array. The array was modelled by combining the measured energy-resolution of the 7-element detector, with a GEANT Monte-Carlo simulation of the detector response to the complex lunar spectrum. In addition, the effectiveness of different modes of analysis of the energy-loss data, to improve the sensitivity of the detector, have been considered.

An important factor in determining the sensitivity of a CsI(Tl) array, placed on an orbiting spacecraft, is the mass of CsI(Tl) that may be incorporated into the instrument, whilst remaining within the mass limitations. Previous PMT based spectrometers have incorporated an anticoincidence shield to eliminate the charged particle background and perform coincidence spectrometry [73]. This was necessary for two reasons. Firstly, the primary detector was a single crystal and therefore analysis techniques could not be applied to eliminate the cosmic-ray charged particle and Compton-scattered background. Secondly, the size of the PMT is limited to 3" and therefore the dimensions of the primary crystal are limited, if a reasonable aspect ratio and hence energy-resolution is to be maintained. Therefore it is not possible to simply increase the size of the primary detector to utilise all the available mass. A CsI(Tl) array consists of many discrete detectors and therefore several data analysis techniques can be implemented to eliminate many of the charged particles and reduce the Compton and space craft induced background. In addition, the arrays can be scaled in size to accommodate the available payload mass without causing a significant degradation of the energy-resolution of the detector.

Cosmic rays are predominantly protons with energies up to several GeV [74]. Charged particles, interacting with the array, will deposit approximately 2MeV/gm/cm^2, which will result in an energy deposit in excess of the upper bounds of the region of interest unless the particle traverses the edge of the detector. Therefore, the effect of a cosmic-ray charged particle may be eliminated from all but the outermost crystals of the array by simply setting an upper energy-threshold.

A more serious problem may be experienced when the cosmic rays interact within the body of the spacecraft, resulting in a shower of particles including neutrons, which in turn, may activate the vehicle. The activated elements will then decay, often with the emission of a gamma-ray or an electron, thus leading to the spacecraft becoming a source of background radiation. The effect of the space-craft induced background may be estimated if the detector is placed on a 2m boom and has a constant position relative to the main body. The array elements closest to the body of the space craft will naturally act as shields for the elements further away. Therefore, by combining a Monte-Carlo mass-model [75] of the spacecraft-induced background with a detailed analysis of the variation of the energy-loss spectrum across the array, it should be possible to subtract the spacecraft-induced background. This technique could be applied when the spacecraft is in the cruise phase when no planet is in view.

The effect of the particle albedo radiating from the surface has been modelled by Dr F. Lei using the GEANT/GCALOR codes [76]. The effects of 10^5 proton impacts of 1 GeV, fired isotropically onto the top surface of a slab 1 metre thick, was simulated. The composition of the slab was similar to that of the lunar crust. The particles, in the energy range 1 to 10 MeV, escaping from the surface, were recorded and are shown in Table 4.2.

Particle Type	Electron β^-	Positron β^+	Proton P	Pion+ Π^+	Pion- Π^-	Others	Total	Gamma γ
Relative Number of Particles	327	1234	59	22	8	21	1671	37030

Table 4.2 Particles emerging from the surface of the lunar crust

The total number of albedo charged-particles, in the energy range from 1 to 10 MeV, is about 5% of the number of gamma-rays. However, the detector will have an almost a 100% efficiency for charged particles, whilst the average gamma-ray detection efficiency is approximately 50%. The background counting-rate due to the charged particles will therefore be approximately 10% of the total. Based on this figure alone, it appears that the inclusion of a charged particle veto in the design would only achieve a relatively small reduction in the background rate from the surface of the planet.

The above arguments would suggest that it would be prudent to place all the available active mass of the detector in the CsI(Tl) array and not use the active shield. However, for comparison of an NaI(Tl)-PMT detector a BGO-PMT detector and a CsI(Tl)-phtodiode array it has been assumed that the CsI(Tl) array will in fact need an active shield.

The active shield does not need to provide any energy information. It simply needs to register that an energy deposit has taken place so that any coincident events in the primary detector may be ignored. A possible mass efficient design, for an active shield, is shown in Figure 4.13. The shield consists of a cylinder of plastic scintillator with two end caps of the same material. The scintillation light produced by a charged particle is transferred by means of a wavelength shifting fibre ribbon from the scintillator to a small PMT. If we assume that the signal generated in the PMT will need to be of the order of 10 photo-electrons, to identify an event above the noise, then it is possible to estimate the thickness of plastic scintillator required to shield the detector.

Some of the energy deposited in the shield will be lost at each stage of the transfer of photons from the shield to the PMT. Therefore it is necessary to estimate these losses before calculating the thickness of shield required. It has been assumed that the light collection efficiency from the scintillator will be approximately 20%, the conversion in a 1mm wave length shifting fibre will be approximately 50%, the transfer efficiency of the fibre will be approximately 5% and the quantum efficiency of the PMT will be 20% [77]. Multiplication of these energy losses results in an efficiency of 0.075%. Therefore the signal in the scintillator will need to be of the order of 10^4 photons. Assuming the charged particle deposits approximately 2MeV/cm in the shield it should not require more than 0.5cm of material to provide the required signal. To shield a 61-element array the total mass of plastic scintillator required would be approximately 540 grams and therefore the entire shield, including PMT should not weigh more than 0.75kg.

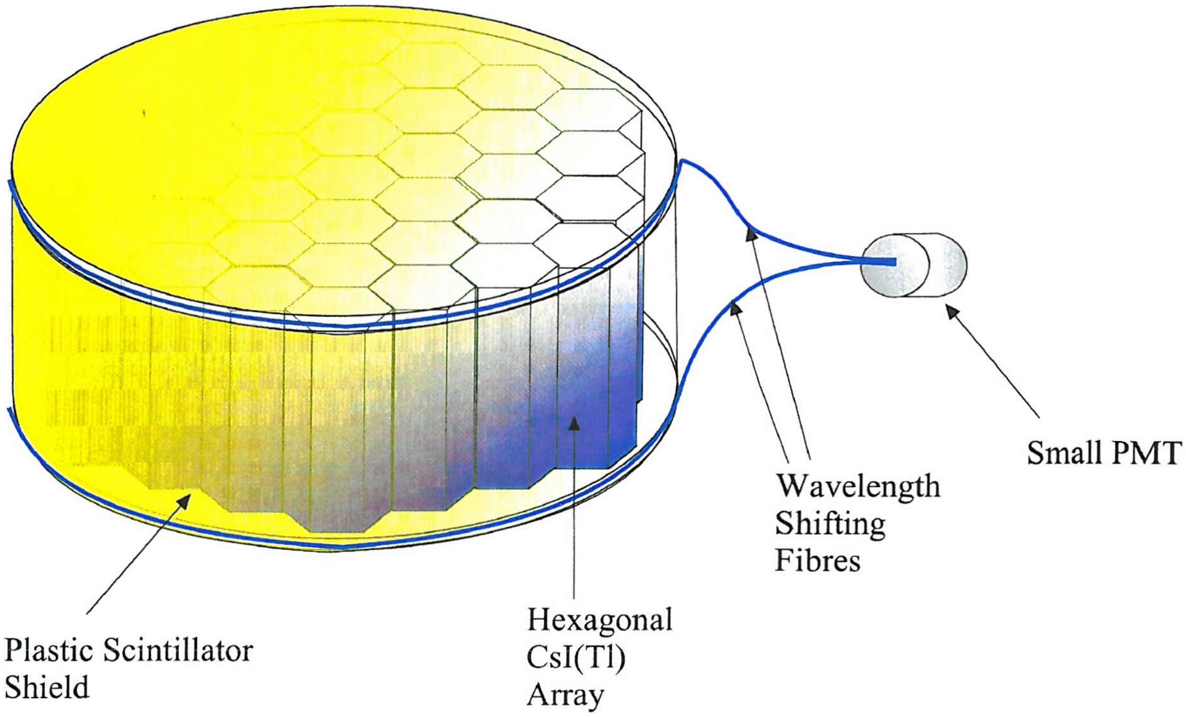

Figure 4.13 A CsI(Tl) array with a charged particle shield and fibre read-out

The mass of the two scintillator crystals and their associated PMT's, in the Lunar Prospector GRS, was approximately 5kg. The remaining 3.6kg being used for the housing, temperature control and electronics. Therefore, allowing 5kg for the CsI(Tl)-photodiode array, it seems fair to assume that the GRS will contain at least 4kg of CsI(Tl). This would correspond to a 61 element array, each crystal being 2cm AF and 5cm long.

The response of a 61 element array has been simulated by combining a GEANT Monte-Carlo simulation with the energy resolution calibration curve derived from the 7-element array test results. The spectra do not include the effect of the charged particle or spacecraft background and hence cannot be used to calculate the overall sensitivity of the detector. However, this analysis serves to demonstrate the benefits of each mode of analysis when recording complex emission spectra. The three modes of analysis considered are; simple summation, coincidence spectrometry and pair spectrometry.

4.5.1 Simple Summation

The simple summation spectrum consists of the sum of all energy deposits, which result from photoelectric, Compton and pair-production events. It includes all energy deposits regardless of whether the full energy of the incident photon was deposited in the detector. As a result, it is possible that certain features may become less significant due to an underlying background caused by partial energy-loss events.

The spectrum shown in Figure 4.14 represents the predicted response of the detector to 10^6 photons having a spatial and energy distribution that would be experienced by a Lunar-orbiting spectrometer. The average flux, incident on 4kg of CsI(Tl), in a spectrometer orbiting at an altitude of 100km, will be approximately 150 photons s^{-1} [26]. Thus the spectrum represents a 6600s of observation of the planet surface. The Lunar Prospector has a lifetime of approximately 1 Earth year and therefore, if a CsI(Tl) array were in orbit around the Moon for a similar time, the spectrum for the whole planet would contain 5000 times more photons than have been used for this simulation. However, for the purposes of imaging the surface, the time of observation would be much shorter and will vary greatly between polar regions and equatorial regions. The regions near the poles will be observed on every orbit whereas the regions near the equator will be observed much less frequently.

Some of the gamma-ray emission lines from the lunar surface are expected to be Doppler broadened, due to in-elastic neutron scattering, which is not included in the simulated spectra. However, the Doppler broadening is generally a less significant source of broadening than the effect of the energy-resolution of the detector and will not greatly affect the overall shape of the spectrum.

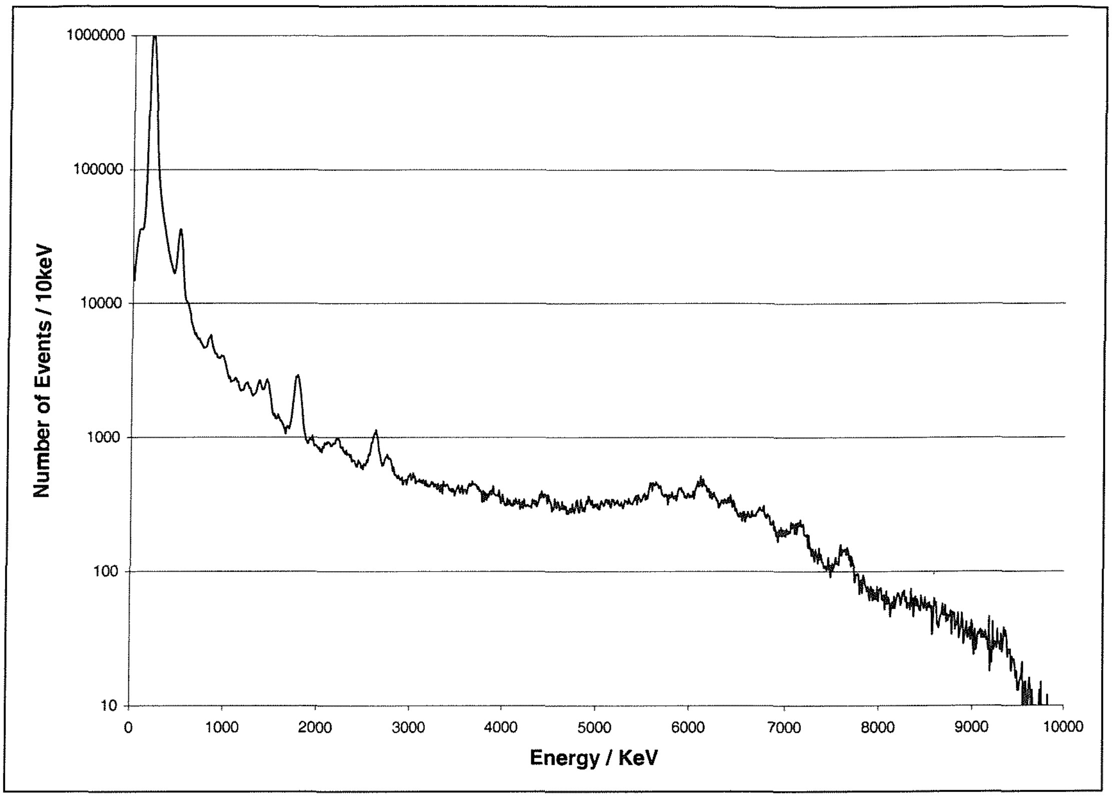

Figure 4.14 The response of a 4kg, 61 element, CsI(Tl)-photodiode array to 10^6 photons from the lunar surface

4.5.2 Coincidence Spectrometry

In the energy range from 300keV to 6 MeV, Compton scattering is the dominant interaction mechanism for gamma-rays interacting in CsI(Tl). Therefore it is likely that the number of crystals in which an energy deposit will occur, will be greater than one, if the total energy of the photon is deposited in the array. Any energy-loss event in which, only a single energy deposit occurs, is most likely to be the consequence of an interaction of a photon by the Compton scattering mechanism, where the secondary, scattered photon, has escaped from the sensitive medium. Thus, when performing coincidence spectrometry, only events in which there is more than one energy deposit, are recorded in the energy-loss spectrum. Comparing Figure 4.15 with Figure 4.14, it may be seen that that the features in the coincidence spectrum are better defined even though there are fewer events in the spectrum. This is a consequence of a reduction in the partial energy-loss component of the spectrum due to Compton-scattering in the detector. The photopeaks are therefore enhanced compared with the underlying background and therefore this mode of operation can be considered to be more sensitive.

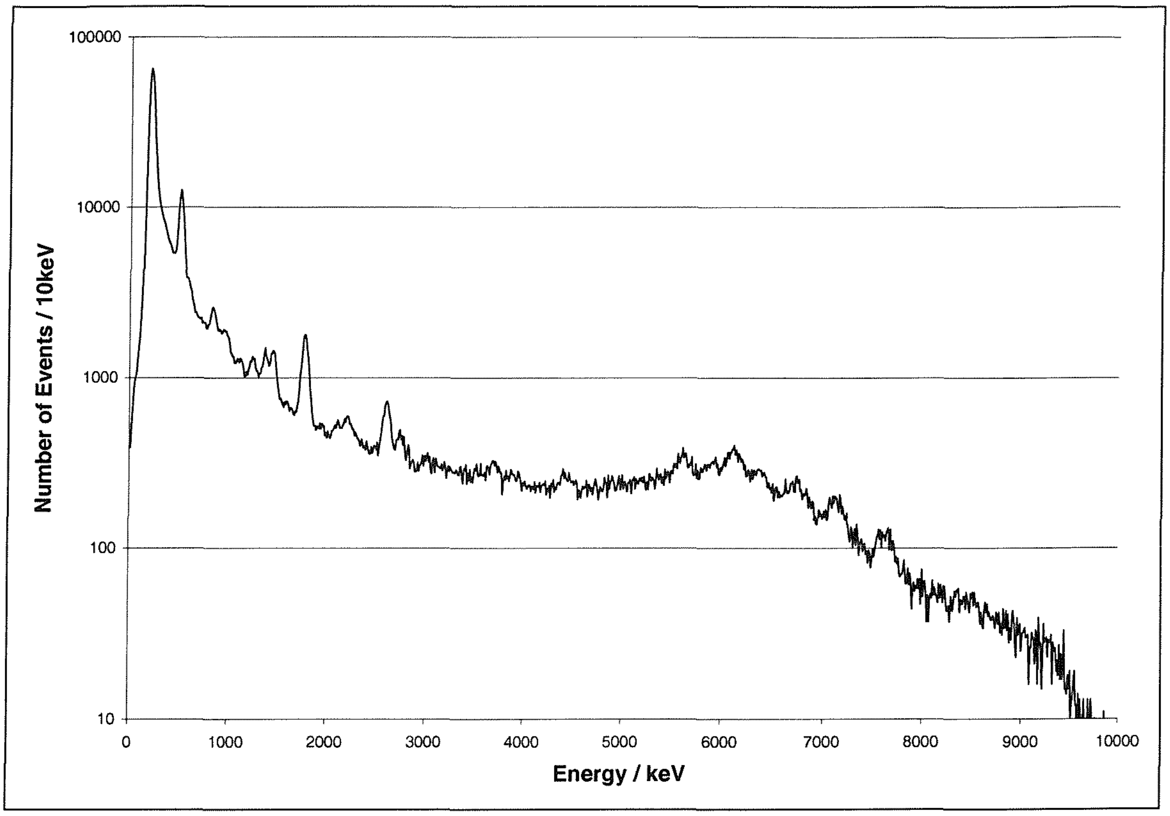

Figure 4.15 The coincidence event response of a 4kg, 61 element, CsI(Tl)-photodiode array to 10^6 photons from the lunar surface

Figure 4.16 shows a triple coincidence energy-loss spectrum resulting from 10^7 photons. This is approximately equivalent to 18.3 hours of observation. As may be seen, the requirement for 3 coincident events means that pair spectroscopy is an inefficient process but it does have the advantage that virtually every event is a full-energy absorption peak and therefore there is virtually no background noise and the escape peaks have been rejected. Due to the inefficiency of the process it would not be practical to try to use the technique to characterise small areas of a planet with limited data. However, when forming an overall picture of the planetary composition, this technique may provide information that could not be readily extracted by analysis of the simple summation spectrum.

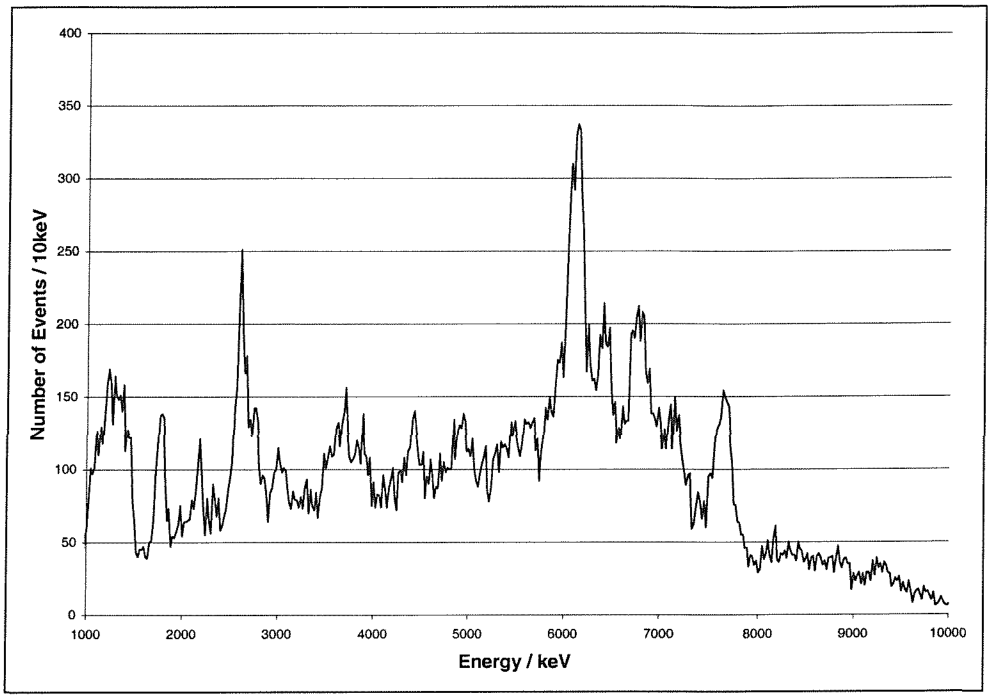

Figure 4.16 The recorded energy-loss spectrum from a 61 element, CsI(Tl)-photodiode array, to 10^7 photons, when operating in pair spectrometry mode

4.6 Conclusion

A CsI(Tl)-photodiode array, used for remote geochemical analysis, has been shown to have a superior energy resolution than a conventional scintillator-PMT spectrometer for the important energy range from 2 to 10MeV. The improvement in the energy-resolution, combined with the fact that a 8.6kg CsI(Tl)-photodiode spectrometer will have a greater mass of crystal, when compared to the same mass scintillator-PMT detector, will result in a CsI(Tl) detector having a superior sensitivity when used for remote geochemical analysis. In addition, due to the pixelated nature of the detector it is possible to analyse the data in simple summation, anti-coincidence or pair-production modes. These methods of analysis simplify the energy-loss spectrum but ultimately result in the rejection of many energy-loss events that contain information about the incident gamma ray spectrum. Therefore, to fully utilise the information contained in the total energy-loss spectrum, it would be better to deconvolve the incident spectrum in order to reconstruct the incident gamma-ray flux. The following chapters discuss some of the methods for the deconvolution of complex gamma ray spectra and present the deconvolved results from real and simulated data.

Chapter 5

5 A Preliminary Study of the Benefits of Spectral Deconvolution

5.1 Introduction

Whenever a measurement is made, there are associated systematic and random errors, which result in an uncertainty, in the absolute value of the parameters of the object under investigation. If the systematic errors of a measurement system are known, the systematic effects can be minimised by subtracting, or deconvolving their influence from the observed data. This problem of reconstructing an unknown distribution from a finite set of measurements occurs in many branches of science and consequently, many techniques have been developed to address this *inverse problem*.

The *inverse problem* is particularly relevant to scintillator gamma-ray detectors since the dominant source of ambiguity, in the observed spectrum, is related to the characteristic response of the detector. The amount of energy deposited in the sensitive medium, by an incident gamma-ray, varies depending on the type of interaction. This, combined with the limited energy-resolution of the detector, results in the observed energy-absorption spectrum being quite different from the incident gamma-ray spectrum. Thus, if it is possible to deconvolve the effect of the detector on the observed data, it will be possible to improve the sensitivity of the detector dramatically and make an accurate prediction of the gamma-ray flux, incident on the detector, that resulted in the observed energy-loss spectrum.

This chapter explains some of the principles of spectral deconvolution methods and demonstrates the improvement that may be achieved as a result of applying these techniques to a CsI(Tl)-photodiode gamma ray detector. It may be seen that, under certain circumstances, the deconvolved spectrum is so clear that it does away with the need for any additional data analysis techniques such as coincidence or pair-spectrometry.

5.2 A Review of the Method for the Analysis of the Apollo Data

Analysis of the gamma-ray spectra returned by the Apollo missions required sophisticated deconvolution [41]. The analysis was limited by the lack of computer processor power, knowledge of certain neutron-interaction cross sections and the neutron spectrum produced by intergalactic cosmic ray interactions with the lunar crust. Thus data from returned lunar soil samples was used to calibrate and validate the spectrometer data. The accuracy, with which neutron interaction cross-sections are known has improved in the last 25 years and, combined with the advancement in computer technology, has made it possible to deconvolve complex gamma-ray spectra without the aid of ground-truth data.

Following the success of the Apollo GRS instruments, many studies were made of the data, in order to interpret the chemical composition of the lunar surface. The analysis of the gamma-ray spectra was greatly aided by the laboratory chemical analysis of lunar anorthosite and chondrite materials returned by the Apollo 11, 12 and 14 missions. Knowledge of the chemical composition of the returned samples made it possible to calculate the gamma-ray flux that would result from neutron irradiation of these rock types [78] [41]. The model was derived by Reedy, Arnold and Trombka and hence was given the name RAT. The method for calculating the expected gamma-ray spectra was complex and considered the incident cosmic-ray flux, interaction mechanisms, interaction cross-sections, scattering of photons before emerging from the surface, detector sensitivity and resolution. The response of the detector was deconvolved using a singular value matrix inversion, which is described in detail in the following chapter. It must be remembered that computers were still relatively in their infancy at that time and hence deriving the spectra was a major task. In addition, the accurate prediction of the fluxes relied on accurate elemental cross-section data for neutron interactions, which are constantly being updated and improved.

Several analyses of the data returned from the Apollo missions were based on the RAT model. Due to the lack of computing power, the analysis of the data was very slow and results were being published for several years after the mission. Metzger et al calculated the Th, K, Fe, Mg and Ti from 28 selected regions on the lunar surface [46]. The experimental data had to be processed to eliminate parity errors and adjust for variations in the gain of the spectrometer. The data rates were corrected for solid angle to a constant height of 110km above the lunar surface. All data, obtained over each region to be analysed, were accumulated into a single master spectrum from which the background and spacecraft contributions could be subtracted. The method of analysis required 30 to 40 minutes of data to quantitatively analyse the selected elements. The most difficult part of the analysis was deriving the underlying continuum that does not contain any characteristic lines.

The analysis of the energy-loss spectrum was broken up into two phases. Firstly, following the removal of the continuum, only the spectrum from 5 to 9MeV was analysed. In this region only Fe, O, Si and Ti contribute significantly. The component intensities derived by matrix inversion were then subtracted from the spectrum and the difference spectrum in the lower energy region was then analysed using all the remaining components. The elements that were successfully analysed were grouped into two classes. The elemental concentrations of the natural radioactivities, K, Th, and U were derived from the decay scheme and knowledge of the detector, using theory and laboratory calibrations. The elements which depended on cosmic-ray excitation, O, Si, Fe, Mg and Ti, required input from nuclear and cosmic-ray physics, the combined accuracy of which was admitted to be "not very high" at the time of the deconvolution. This resulted in the absolute flux radiating from the planet deviating by ±25% from the values calculated by RAT. It was therefore felt that the neutron spectrum must be harder than that used in the model.

The spectrometer data was normalised using the "ground truth" data to confirm the orbital data at several points on the surface. However, the sites had to be carefully chosen to avoid any regions that showed large surface compositional variations over a short range. Eventually, the Fe, Mg and Ti elements were normalised using the Mare Tranquilatis ground truth data and the Descartes region as a check. However, even when using the most reliable ground-truth site there was a correction factor added to the Ti concentration since it was argued that the returned soil concentration could not be representative of the region for this element. Since the early interpretations of the Apollo data, several improved analyses have been made that include a more detailed consideration of factors such as the spacecraft activation background, electron bremsstrahlung in the detector, proton and neutron induced activity in the detector plus other background contributions [47] [48]

Considering the lack of computing power and nuclear interaction information, it is an achievement that the Apollo scientists managed to deconvolve the gamma-ray spectra. However, from the above discussion, one may see that without the ground-truth data it would not have been possible to accurately interpret the gamma-ray spectra returned from the Apollo missions. Such ground-truth data will almost certainly not be available for future missions to Mars, Mercury and the Asteroids. Therefore, the analysis of the data will need to be improved. Several factors should help improve the accuracy of the deconvolution process.

The primary and probably the most obvious factor, is the dramatic increase in computing power available to modern scientists. This not only allows large and bulky deconvolution methods to be utilised but also allows the response of the detector and the effect of the surrounding spacecraft to be simulated to aid in the reduction of background noise [75]. High-energy particle transport codes, such as the GEANT Monte Carlo code developed at CERN, can be used to simulate the transport of high energy particles in the detector and cosmic-rays in the planetary soil [76]. This information, could in theory allow the recorded energy-loss spectrum to be deconvolved to predict the surface composition that could have resulted in such a spectrum.

It is not only the advances in computer power that have allowed the development of reliable Monte-Carlo simulation codes. In fact, the computer is only a device for rapidly performing mathematical calculations. The accuracy of the simulations depends entirely on the quality of the nuclear data contained within the libraries of the code. This information has also improved over the last 25 years. The net result is that the response of a gamma-ray detector, can now be modelled in detail without constraints on the number of incident gamma-ray emission-lines that may be incident on the detector. One such method of unconstrained deconvolution is the *expectation maximisation* technique that is described below.

The Lunar Prospector, which was launched in January 1998 will be the first gamma-ray spectrometer, since the Apollo missions, to map the elemental composition of the Moon. Initial results have been presented on the distribution of thorium and potassium plus limited information on the distribution of iron. However, the detailed detector modelling and spectral fitting procedures required to convert the gamma-ray energy-loss spectra into absolute elemental abundance for all elements has not yet been carried out [79]. The detector design is not complicated and therefore the detailed detector response should be relatively simple to calculate using a Monte-Carlo simulation code. Therefore it could be expected that detailed, deconvolved elemental maps might be published in 1999.

5.3 Deconvolution of the Measured Energy-loss Spectra by Expectation Maximisation

The data acquired by a gamma-ray detector may be expressed in terms of a matrix multiplication as shown in Equation 6.1. The energy-loss spectrum is characterised by its intensity distribution O(x), corresponding to the observation of an incident spectrum I(x) through a gamma ray detector. Where (O) is the product of the incident flux (I) multiplied by the response of the detector (Q) plus an additive noise component (N).

The response matrix or Q-matrix provides a mapping between the incident photon energy and the observed photon energy according to the instrument response at that particular energy. The Q-matrix is a two dimensional array where each row is a vector describing the response of the system to a particular gamma-ray energy. The response of the spectrometer can be calculated using Monte-Carlo simulations of the detector to predict the response of the detector across a wide range of energies. In general, for unconstrained deconvolution, a response is needed for each channel in the energy-loss spectrum. Ultimately, it is the accuracy with which the response matrix models the real response of the detector, which will determine how accurately the energy-loss spectrum may be deconvolved. Any ambiguity between the modelled response and the real response may result in non-real features in the deconvolved spectrum or systematic errors, which may be determined by analysis of the residuals of the fitted spectrum.

$$\begin{bmatrix} O_1 \\ \cdot \\ \cdot \\ O_m \end{bmatrix} = \begin{bmatrix} Q_{11} & \cdot & \cdot & Q_{1n} \\ \cdot & \cdot & \cdot & \cdot \\ \cdot & \cdot & \cdot & \cdot \\ Q_{m1} & \cdot & \cdot & Q_{mn} \end{bmatrix} \times \begin{bmatrix} I_1 \\ \cdot \\ \cdot \\ I_n \end{bmatrix} + \begin{bmatrix} N_1 \\ \cdot \\ \cdot \\ N_m \end{bmatrix}$$

Equation 5.1 The relationship between the observed energy-loss spectrum and the incident spectrum as expressed in matrix form

The aim is to determine I(x) knowing O(x) and Q(x). This implies that some measure of the residuals, O - (I * Q), is to be minimised and hence find the solution with the highest probability or the maximum likelihood. For Poissonian distributed variables, Shepp and Vardi showed that the expectation-maximisation (EM) pair of iterative update steps, results in a strictly increasing likelihood unless the likelihood is already at a maximum thus the solution can be considered to be a maximum likelihood solution [80] .

$$I^{(n+1)} = I^{(n)}\left[\frac{O}{O^{(n)}} \times Q^{*}\right] \qquad \textit{Equation 6.2}$$

where:

$$O^{(n)} = Q \times I^{(n)} \qquad \textit{Equation 6.3}$$

and Q* is the transpose of the response matrix of the detector system.

Expressed in a stepwise manner:

- An initial guess is made for the input spectrum. In general, the starting point of the iterative procedure does not matter.
- This guess is multiplied by the response function.
- The spectrum that would result from the guess is compared as a ratio with the measured spectrum.

- The ratio of the guessed spectrum to the observed spectrum gives a weighting for each gamma-ray energy from which the next guess may be calculated.
- The next guess is formulated by multiplying the weighting factor for each energy, by the transpose of the response matrix.
- The initial guess is then updated by the result from step 4.
- The process is repeated until convergence is achieved and the χ^2 value remains constant.
- Where χ^2 is the sum of the square of the difference between the observed and the fitted spectrum and is usually expressed in terms of the standard deviation.

$$\chi^2 \equiv \sum_{i=1}^{N} \left(\frac{y_i - y(x_i; a_1 \ldots a_M)}{\sigma_i} \right)^2 \qquad \textit{Equation 5.2}$$

A maximum-likelihood estimate of the model parameters is obtained by minimising the quantity chi-square. If the response matrix Q, faithfully represents the response of the gamma ray spectrometer, it will be possible to deconvolve a complex energy-loss spectrum with an error that is set by statistical variations alone.

The goodness of fit may be measured by considering this chi-squared value. If the difference between the observed solution and the fitted solution is due entirely to Poissonian statistical fluctuations then the fitted data could be expected to vary from the measured data by plus or minus the random noise for each data point. The chi-squared value for the most likely solution should be approximately equal to N, where N is the number of degrees of freedom. The reduced chi-squared value is the chi-squared value divided by N and should be close to 1 for a good fit. If the reduced chi-squared value is greater than 1 it indicates less confidence in the solution (i.e. a poor fit), whilst a value less than 1 indicates that the solution has, at least in part, fitted the data to the random noise.

The solution of a maximum-likelihood fit is not unique but will represent one point on an N dimensional surface, which describes the solutions that result in a reduced chi-squared value of 1. It is realised that more specialist deconvolution methods may be applied by introducing a parameter that, once the maximum likelihood has been achieved, will select a particular unique solution from the N dimensional surface. Examples include selection criteria that give the smoothest solution (maximum entropy) or if desired, the maximum resolution between features in the spectrum. The benefit of these techniques is greatest, normally, when the signal to noise quality is low and depends on the particular scenario to be deconvolved and the aim of the analysis [81] [82]. It is not the aim of this chapter to determine the optimum deconvolution technique but instead to demonstrate the considerable benefits that may be achieved using the maximum-likelihood technique.

5.4 Validation of the Deconvolution Technique by Deconvolving a Simple Spectrum from a 1cm^3 CsI(Tl) Detector

The observation and subsequent deconvolution of a laboratory gamma-ray source, with a known energy and intensity, can be used to validate the deconvolution technique. If the strength of the source, the distance of the source from the detector and the cross-sectional area of the detector are known, it is possible to estimate the number of photons passing through the front face of the detector. If the deconvolution technique is correctly deconvolving the energy loss spectrum, it should not only predict the energy of the incident photons but also the number of photons incident on the detector.

5.4.1 Creating the Q-matrix for a 1cc CsI(Tl) Detector

The response of the 1cm^3 detector was simulated using the GEANT Monte-Carlo transport code. A response was simulated for all 512 energy channels using 5×10^5 photons for each simulation. Each channel had a 3.47keV width, to match the channel width of the spectra taken with a Canberra series20 portable MCA.

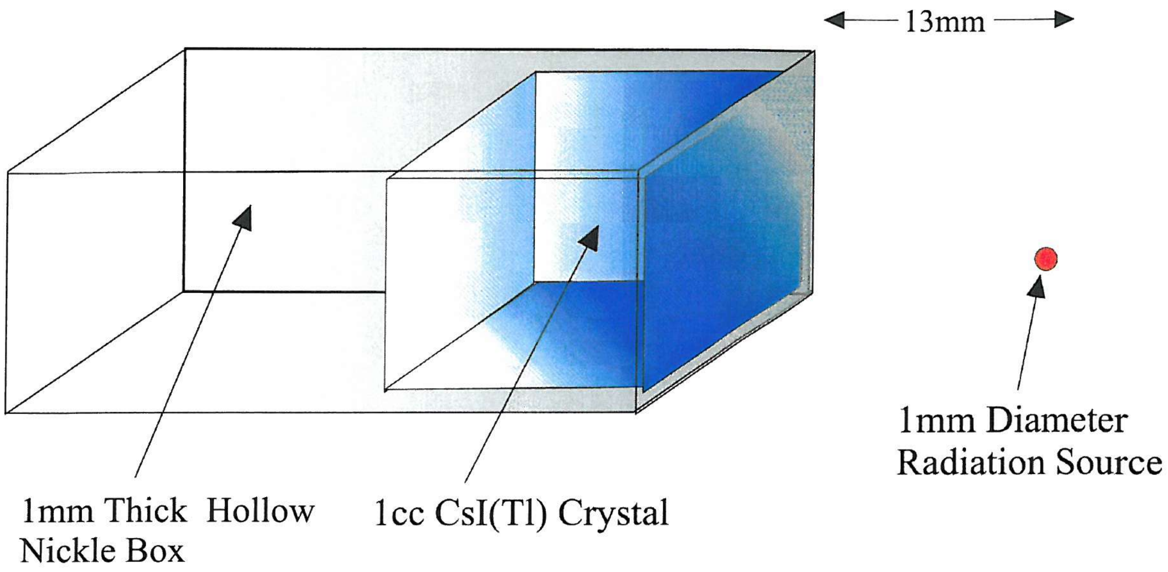

Figure 5.1 The simulated scenario for compiling the response function of the 1cc detector.

The energy resolution of the detector was measured using Cs^{137}, Co^{60} and Na^{22} laboratory sources. Equation 3.4 was fitted to the measured data points, using a Levenburg-Marquardt iterative routine, to derive the line of best fit, which was then used to determine the energy resolution of each of the simulated response functions. The response spectra were collated into a 512×512 array that formed the Q-matrix for the $1cm^3$ spectrometer. It may be noted that the simulation did not include the table or stand that held the equipment in place and therefore it is possible the Q-matrix will underestimate the number of scattered events arriving at the detector.

5.4.2 Deconvolution of the 1cc Spectrometer Spectra

Figure 5.2 shows a 10 second energy loss spectrum from a 1cc CsI(Tl) gamma detector observing a 6.7μCi Cs^{137} source and an 2.0μCi Na^{22} source placed 13mm from the front face of the detector. Clearly visible are the 511, 662 and 1275keV photopeaks as well as the Compton scattered events from each line. However, it may be seen that assessing the absolute flux incident on the detector for each gamma-ray emission line is difficult even for this relatively simple energy-loss spectrum.

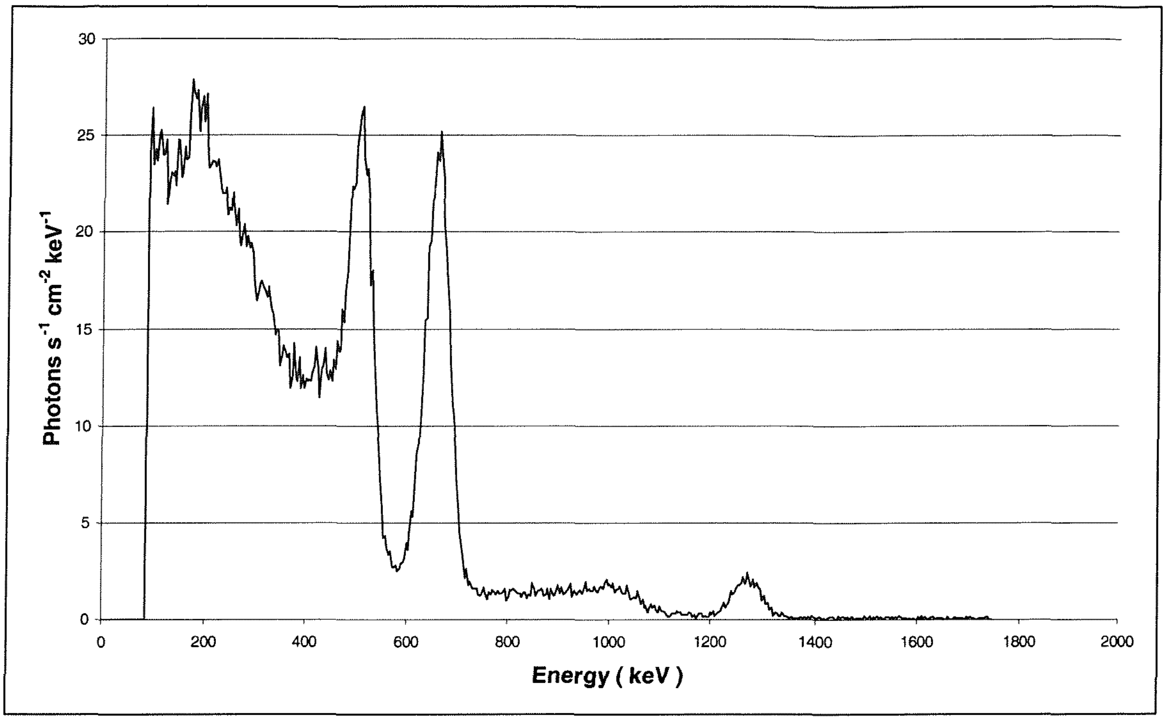

Figure 5.2 The energy-loss spectrum from a 10μCi ^{137}Cs and a 10μCi ^{22}Na source.

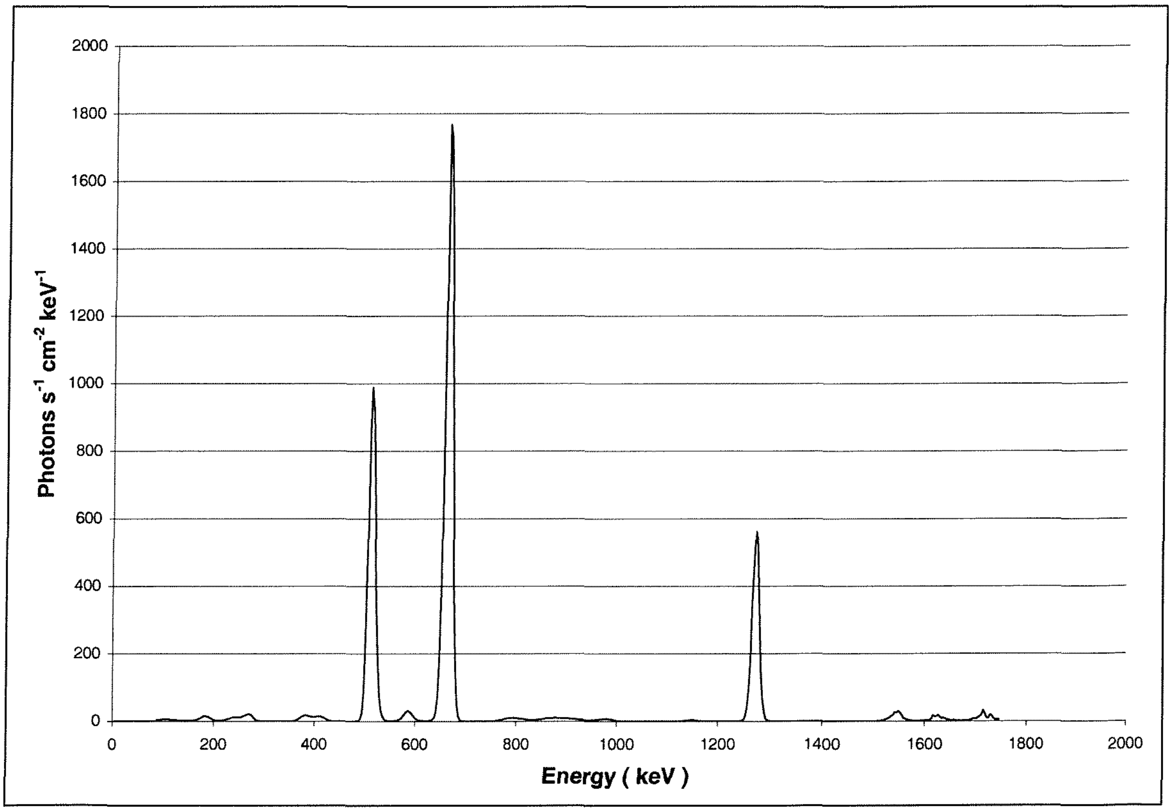

Figure 5.3 The deconvolved spectrum from a 1cm^3 CsI(Tl) detector observing a ^{22}Na and ^{137}Cs laboratory source.

5.4.3 The Deconvolved Spectrum

The deconvolved energy-loss spectrum is shown in Figure 5.3 and clearly shows the emission lines from the sources at 511, 662 and 1275keV and very few other features. The reduced chi-squared value for the fit to the Na^{22} and Cs^{137} spectrum is 1.006 and therefore can be considered to be a good fit. If the deconvolution has faithfully reconstructed the incident flux, the number of incident photons from each emission line should also correspond to the estimated flux passing through the front face of the detector.

The flux passing through the front face of the detector was estimated by taking into account the original strength of the source, the age of the source, the decay chain of the source and the source to detector distance. Table 5.1 shows the deconvolved intensity of each line compared to the calculated intensity from the known sources.

The ^{22}Na source was 6 years old, which would result in an activity of 2.022 μCi, which is equivalent to 75,000 disintegrations per second. The source was placed approximately 15mm from the front of the 1cm^3 detector (the ^{22}Na source was behind the ^{137}Cs source), which would result in approximately 2650 photons passing through the front face of the detector per second. For each decay there are two 511keV photons produced and therefore the predicted number of photons per second is doubled to 5300 photons per second.

The ^{137}Cs source was 17.5 years old, therefore the activity was 6.69μCi, which is the equivalent to 247,000 disintegrations per second. 94% of ^{137}Cs decays are via a ^{137}Bam state, which has a 90% probability of decaying with the emission of a 662keV photon. Thus 85% of decays result in a 662keV photon, which is the equivalent to 209,000 662keV photons per second. At a range of 13mm this would result in approximately 9800 photons per second.

It may be seen that the deconvolved and predicted fluxes are in fairly good agreement. The differences may be explained by very small inaccuracies in the source to detector distance or the crystal dimensions being slightly smaller than 1cm^3. With hindsight it would have been better to place the sources further away from the detector and make longer observations so that small variations in the source to detector distance would not result in large variations in the intensity. The discrepancies between the observed and the deconvolved flux for all three gamma-ray lines can be explained if the source to detector distance is 0.5mm longer than measured. This could be due to the crystal being set 0.5mm back from the front of the detector housing.

Energy / keV	Deconvolved Intensity (photons s^{-1} cm^{-2} keV^{-1})	Calculated Intensity (photons s^{-1} cm^{-2} keV^{-1})
511	5000	5300
662	9400	9800
1275	2600	2800

Table 5.1 The deconvolved and calculated flux through the front face of a 1cc CsI(Tl) detector

5.4.4 Analysis of the Residuals

By analysing the difference between the measured energy-loss spectrum and the fitted spectrum it is possible to see if the differences are due to systematic errors in the Q-matrix or due to statistical variations.

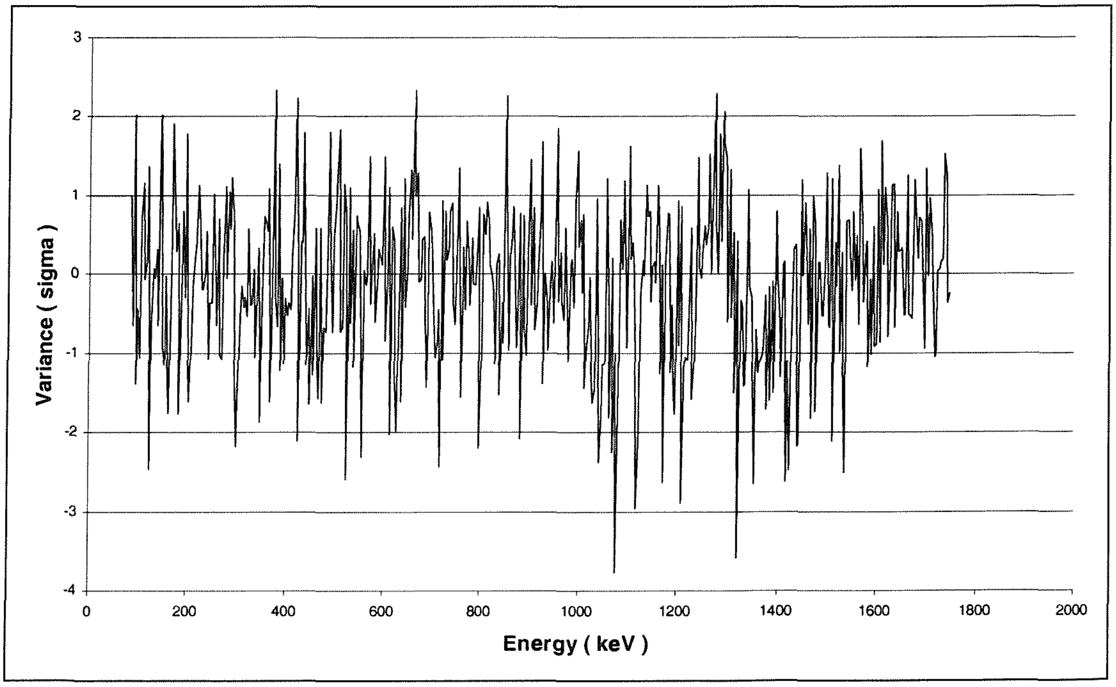

Figure 5.4 The residuals difference between the measured and the fitted spectra.

From Figure 5.4 it may be seen that the residuals generally lie between 0 and 2 sigma. There are some regions where the residuals appear to have a systematic feature such as the region around the 1275keV peak. This may be due to slight inaccuracies in the response model or systematic changes in the detector such as a slight gain drift.

5.4.5 Estimating the Error on the Deconvolved Spectrum

Determining the confidence limits on a set of fitted parameters, which have been determined by chi-squared minimisation, is quite technical and the explanation given here is a summary. For a full explanation refer to Numerical Recipes [83].

Imagine a conceptual scheme of an experiment that measures a set of parameters such as a gamma-ray spectrum. There is some underlying true set of parameters $\mathbf{a}_{true}$, which are only known to Mother Nature but hidden from the experimenter. These true parameters are statistically realised, along with random measurement errors, as a measured data set $D_{(0)}$. The data set is known to the experimenter. A model is then fitted to the data to give a set of parameters $\mathbf{a}_{(0)}$. Because the measurement has random errors, the data set $D_{(0)}$ is not a unique realisation of the true parameters $\mathbf{a}_{true}$, rather there are an infinite number of data sets that could have been the one measured but were not. Therefore each of the other theoretical data sets would have realised a slightly different set of fitted parameters $\mathbf{a}_{(1)}$, $\mathbf{a}_{(2)}$,..., respectively. These parameter sets $\mathbf{a}_{(i)}$ therefore occur with some probability distribution in M-dimensional space of all possible parameter sets $\mathbf{a}$. The actual measured data set $\mathbf{a}_{(0)}$ is just one member drawn from this distribution. Even more interesting would be the probability distribution of the difference $\mathbf{a}_{(i)}$-$\mathbf{a}_{true}$. This distribution has Mother Nature's true value at the origin and if this distribution were known it would provide the quantitative uncertainties in the experimental measurement $\mathbf{a}_{(0)}$. Therefore the aim is to estimate the probability distribution of $\mathbf{a}_{(i)}$-$\mathbf{a}_{true}$ without knowing $\mathbf{a}_{true}$ and without having an infinite number of data sets.

In general there is only one way to make this desired estimation. Assuming that our modelled set of parameters are close to the true values, we can calculate $\mathbf{a}_{(i)}$-$\mathbf{a}_{(0)}$. The distribution of the $\mathbf{a}_{(i)}$'s can be simulated by using computer-generated random numbers to generate many synthetic data sets from the original fitted parameters. Each set can then be analysed to obtain its fitted parameters and the distribution of these fitted parameters. The distribution is usually summarised in the form of confidence limits. A confidence region is a region in the M-dimensional parameter space within which there is a certain percentage probability that the true value lies.

The energy-loss spectrum from the Na^{22} and Cs^{137} sources was assumed to represent the true energy-loss distribution, incident on the detector. A randomisation program was applied to the spectra to apply random noise on each channel and then rebin the data. The new spectrum was then deconvolved using the expectation maximisation program. This process was repeated 30 times to give a distribution of the predicted flux for the 511keV, 662keV and 1275keV emission lines, the results of which are shown in Table 5.2.

Emission Line Energy (keV)	Mean Predicted Incident Flux (photons $s^{-1}cm^{-2}keV^{-1}$)	Standard Deviation	Percentage Standard Deviation
511	5080	62	1.2
662	9388	88	0.94
1275	2634	58	2.2

Table 5.2 The error in the deconvolved flux

The standard deviation on the deconvolved flux was calculated using .

$$S = \frac{\sqrt{\sum X_i^2 - n\overline{X}^2}}{n-1} \qquad \text{Equation 5.3}$$

It is not surprising that the error in the predicted flux is small since the statistics of the spectrum were very good. However, it is reassuring that the error on the deconvolution can be estimated, even though the iterative routine does not implicitly produce an error on the deconvolution. Also, the deconvolution process produces repeatable results for many spectra, which vary from the original spectrum by the addition of random noise.

5.5 Expectation Maximisation deconvolution of the 7 element Array Spectrum

The model for a 7-element array is slightly more complex than that of a simple 1cc detector. There is greater scope for discrepancies between the modelled response and the actual response since the model assumes each element of the array will behave in an identical manner whereas in reality there may be differences. However, the principle of the deconvolution method remains the same and one should be able to deconvolve an energy-loss spectrum from the 7-element array.

5.5.1 The Detector Response Model for the 7 Element Array

The quality of the detector response-matrix, or q-matrix as it is often called, will determine the number and size of any systematic defects in the deconvolved energy-loss spectrum. The GEANT Monte-Carlo simulation software was used to compile the response of the 7-element detector, at 20keV energy intervals, from 0 to 8MeV. The software model of the gamma-ray detector included the individual crystals and the housing of the detector. The detector was assumed to be illuminated by a parallel flux of gamma rays, through the front face of the detector. This is similar to the geometry of the flux expected to emerge from the neutron tank. However, the gamma-rays entering the front face of the detector will not be perfectly parallel but will have a distribution which is somewhere in between a point source and a parallel source. The detector was approximately 30cm from the neutron source. This may result in slight inaccuracies in the response matrix. The ideal situation would be to model the geometry of the detector and the source. However, since the distribution of the source of gamma-rays is not known a compromise was needed.

The output from the GEANT Monte-Carlo code does not include the energy resolution of the detector in the response function. This is overlaid separately using an equation to determine the energy resolution as a function of gamma-ray energy. The energy resolution of the detector was measured using standard laboratory gamma-ray sources such as Cs^{137}, Na^{22}, Co^{60} and the principal lines emerging from the neutron tank due to hydrogen and carbon de-excitation. The function that describes the energy resolution relationship was derived by performing a least squares fit of the measured energy resolution of the detector as shown in chapter 4.

5.5.2 Deconvolution of the Energy-loss Spectrum from the Neutron Tank

The gamma-ray spectrum emerging from the water tank, containing the Am-Be neutron source, was recorded by the 7 element array and deconvolved using the expectation maximisation routine. The recorded and fitted energy-loss spectrum are shown in Figure 5.5, from which it may be seen that the data and the fit are a very good match. The 2.22 and 4.44MeV emission lines from hydrogen and carbon dominate the deconvolved spectrum shown in Figure 5.6. The deconvolved energy resolution of 2.22MeV photopeak is approximately 2.7% FWHM compared to 4.5% for the raw energy-loss spectrum. The deconvolved energy resolution of the 4.44MeV photopeak is 3.1% FWHM, of which 2.4% is due to the Doppler broadening of the emission line and < 2% due to the energy resolution of the deconvolved gamma-ray spectrum.

The two lines are superimposed on a continuum, which is the result of forward Compton scattering photons, in the water, surrounding the neutron source. It may also be seen that the escape peaks from hydrogen and carbon are not completely deconvolved back into the photopeaks. This may be due to the actual crystal geometry being slightly different to that assumed for the simulation of the response matrix. In addition, the flux from the decay of carbon is Doppler broadened. This effect is not accounted for by the response matrix and therefore cannot be deconvolved from the energy-loss spectrum.

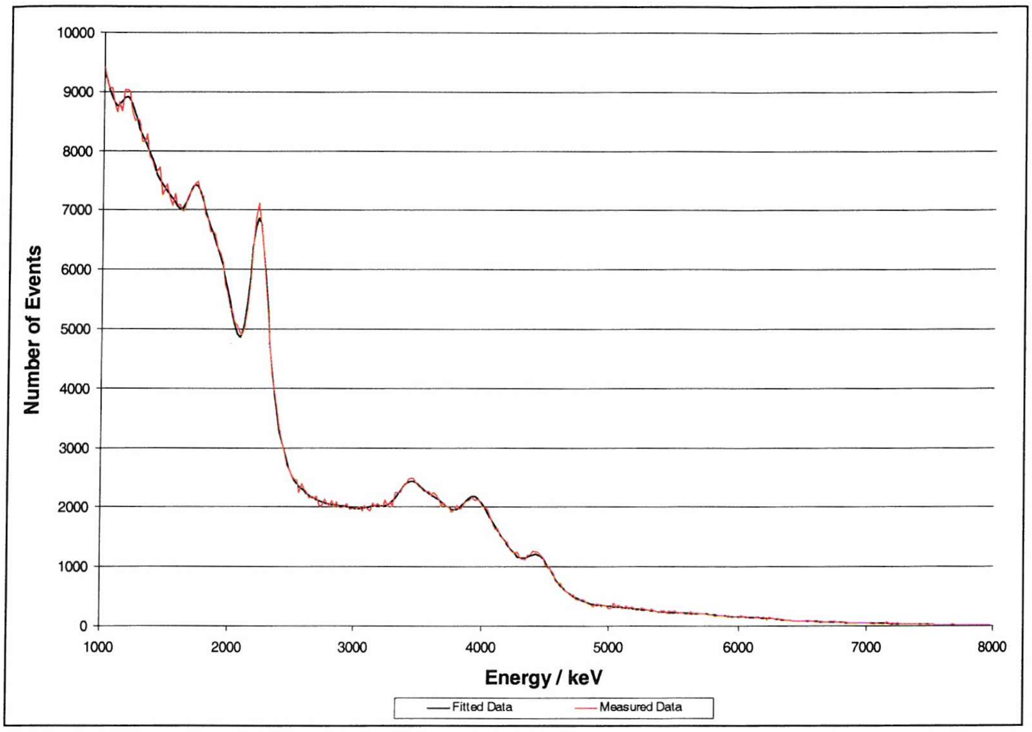

Figure 5.5 The energy-loss spectrum and the fitted data from the Am-Be neutron source tank.

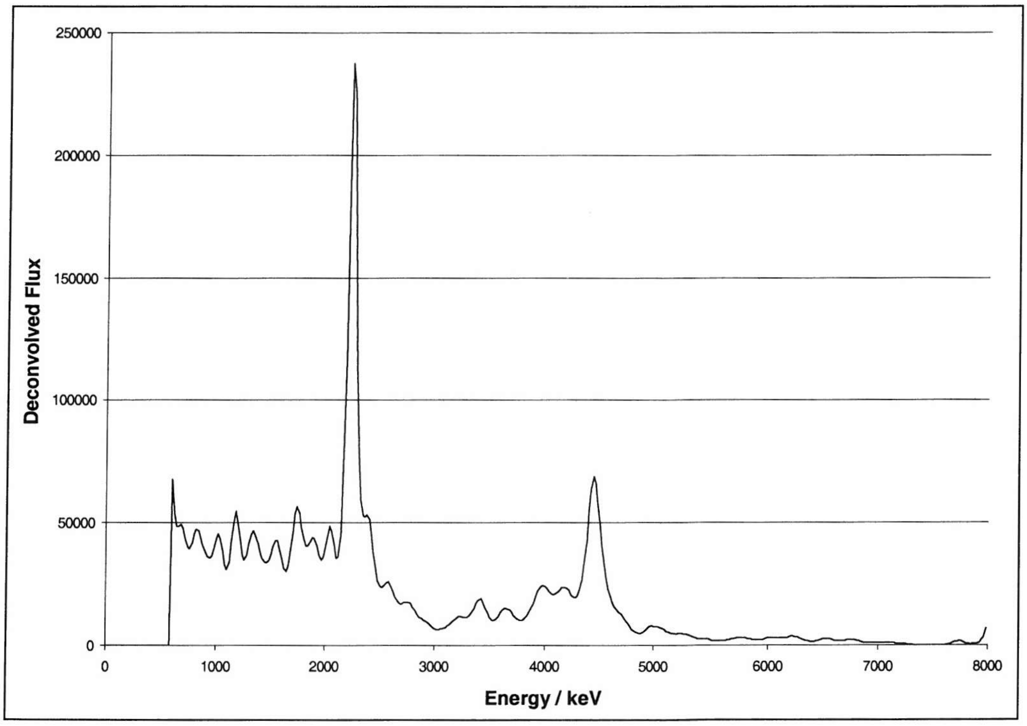

Figure 5.6 The deconvolved incident spectrum from the Am-Be neutron source tank.

5.5.3 Analysis of the Residuals

The residuals between the fitted and the real spectrum are shown in *Figure 5.7.* It may be seen that the residuals generally lie in the range from 0 to 2 sigma. However, there are some systematic errors, which tend to be in the region of the photopeaks. This may be due to a slight inaccuracy in the energy resolution assumed for the response function, a slightly non-Gaussian photopeak response or small variations in the size of the crystals of the detector. The systematic error at 4.44MeV is probably due to the Doppler broadened carbon photopeak not having a Gaussian shape. The large systematic error above 7.5MeV is due to the existence of higher energy emission lines that are not modelled and hence cannot be fitted.

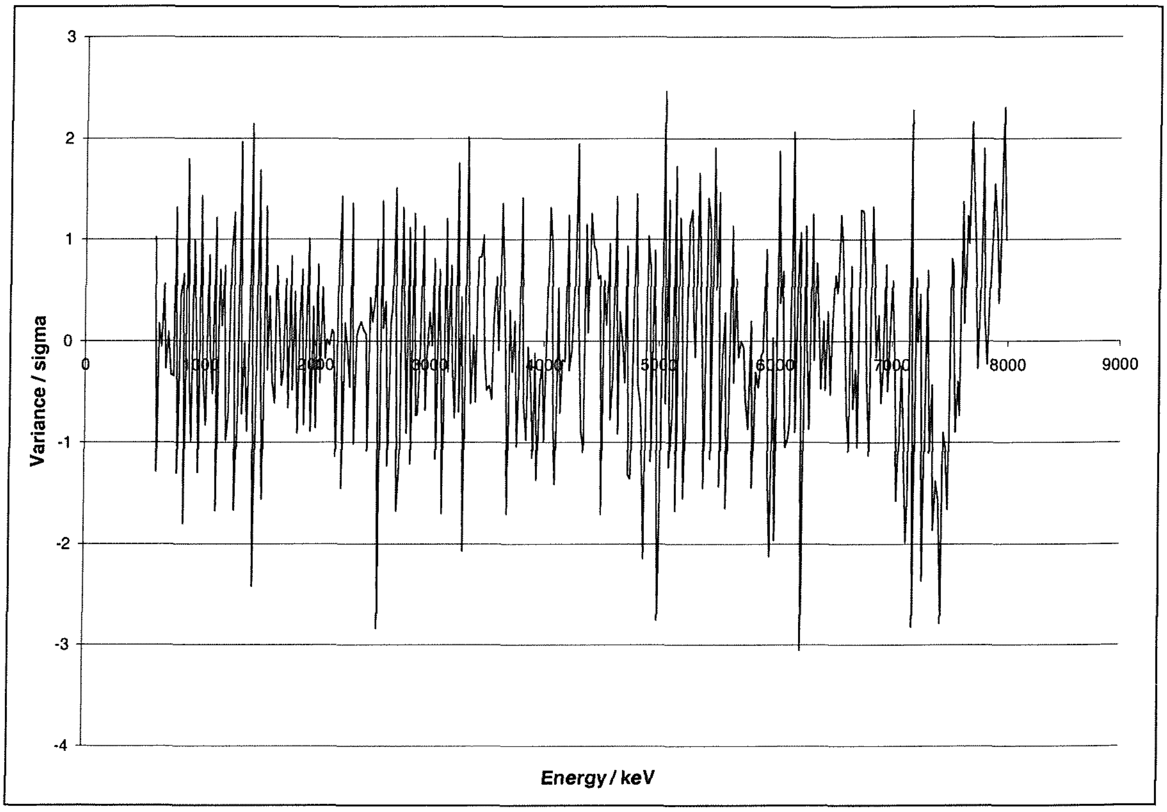

Figure 5.7 The residuals from the deconvolution of the neutron tank spectrum.

Even though the deconvolution of the energy-loss spectrum has resulted in a good fit and the residuals do not show any significant systematic errors, it does not necessarily mean that the deconvolved spectrum is absolutely correct. For example if the response matrix were incorrect, it could result in imaginary features in the deconvolved spectrum that are necessary to produce a good fit to the data. We know that emission lines at 2.22 and 4.44Mev should dominate the spectrum emerging from the neutron tank. In addition, it may be expected that there would be an underlying continuum, as a result of gamma-rays scattering in the water surrounding the neutron source, before they emerge from the tank. Therefore the deconvolved spectrum in Figure 5.6 appears to agree with this expectation. The two predicted emission lines are centred at 2.22 and 4.44MeV respectively and there is an underlying continuum, which is particularly evident in the region between 1 and 2 MeV.

5.5.4 Error Analysis

The error on the deconvolved flux was calculated using the same method as described for the 1cc CsI(Tl) spectrometer. However, because of the underlying background, the error was calculated on the FWHM of the photopeaks to avoid any uncertainty of the edge of the peak. The predicted flux and error are shown in Table 5.2. Again it may be seen that the deconvolution program produces consistent results and the estimated error on the predicted flux is small due to the good photon-statistics.

Emission Line Energy (keV)	Mean Predicted Flux in the FWHM	Standard Deviation	Percentage Standard Deviation
2220	886000	10000	1.2
4440	441000	9000	1.9

Table 5.3 The error on the 7 element array deconvolved flux.

5.6 Conclusions

This chapter has explained and demonstrated the potential benefits of deconvolution techniques such as the maximum expectation routine. Validation of the deconvolution technique was provided using a simple 1cc CsI(Tl) detector and laboratory gamma-ray sources. The energy-loss spectra from the known strength laboratory gamma-ray sources, Cs^{137} and Na^{22}, were recorded by a 1cc CsI(Tl) crystal. The deconvolved and the calculated flux incident on the front face of the detector were in good agreement. The differences being as a consequence of slight errors in the source-to-detector distance. The errors on the deconvolved predicted flux values were calculated and found to be small because of the good gamma-ray counting statistics.

The same technique was used to deconvolve the energy-loss spectrum, recorded by the 7 element CsI(Tl) array, of an Am-Be neutron source immersed in a water tank. The deconvolved spectrum clearly shows the two dominant gamma-ray lines, at 2.22 and 4.44MeV, superimposed on a continuum, which is due to photons scattering in the water tank before emerging from the top surface and entering the detector. Again the error on the deconvolution was found to be small.

The deconvolution process also gives the detectors an improved pseudo energy-resolution. The 1cc detector energy resolution was improved from 8.3% FWHM at 662keV in the raw spectrum to 2.5% FWHM in the deconvolved spectrum. The energy resolution of the 2.22MeV gamma-ray line recorded by the 7 element array improved from 4.5% FWHM in the raw spectrum to 2.5% in the deconvolved spectrum. The 4.44MeV line is difficult to assess because of the Doppler broadening associated with the emission line. However, the energy-resolution of the line in the deconvolved spectrum is 3.1% FWHM, of which approximately 2.4% is due to Doppler broadening and $< 2\%$ due to the energy resolution.

Previously, when considering the optimisation of the dimensions of gamma-ray detectors, an emphasis was placed on maximising the photofraction. It may be concluded from the work in this chapter that, if the response matrix is a faithful representation of the detector response, it may no longer be necessary to maximise the photofraction since partial energy-loss events could be deconvolved to accurately reconstruct the photopeak location and intensity. Therefore, the most important criterion is to maximise the number of energy-loss events whether they are partial or photopeak events. Assuming a detector of restricted mass, this conclusion would suggest that a thin, large area detector would provide a greater sensitivity than a detector designed to produce a high photofraction. In reality, the deconvolution routine may not be able to converge to a solution for a spectrum in which there are few features such as photopeaks. This problem of optimising the detector thickness when deconvolution techniques are available is examined in the following chapter.

Chapter 6

6 Consideration of the Geometry of the Spectrometer when Applying Deconvolution Techniques

6.1 Introduction

The use of sophisticated deconvolution techniques allows the information contained within the partial energy-loss component of the spectrum to be used to reconstruct the incident flux as demonstrated in Chapter 5. The question therefore arises " To what degree can the photofraction be sacrificed, in favour of increasing the number of energy-loss events, whilst maintaining the ability to faithfully reconstruct the incident spectrum". Clearly, this could potentially increase the sensitivity of the spectrometer to incident gamma-rays.

A decrease in photofraction will result in a greater contribution to the error of the deconvolved spectrum, due to statistical fluctuations in the observed spectrum. However, this may be offset by the increase in the number of photons observed when using a large area, thin detector. To gain an understanding of this effect, the response of three depths of CsI(Tl) detector, each with mass 0.5kg, which corresponds to the mass of the 7 element array, have been simulated using a trichromatic flux. The three spectra are then deconvolved and the error on the reconstructed flux analysed. The results of the analysis have been used to reassess the design of a 4kg CsI(Tl) array for remote geochemical analysis.

6.2 Constrained Spectral Deconvolution by Singular Value Decomposition (SVD)

Calculating the error on a deconvolved parameter using the expectation maximisation technique described in the previous chapter is not simple. However, the matrix inversion technique called singular value decomposition intrinsically produces the error on each fitted parameter and hence this technique may be used to analyse the optimum detector depth when using deconvolution techniques.

SVD routine was not used in the previous chapter due to anticipated problems with the routine when trying to invert the response matrix. The potential problem may arise if two functions, or two different combinations of functions produce a fit to the data set, then the response matrix will be unable to distinguish between the two equations and will become singular. In the case of spectral deconvolution, this might be thought of as trying to fit two almost identical spectral response-functions to an energy-loss spectrum. Due to the similarity of the two functions there will exist several solutions to the problem and hence there will be no unique solution. In the case of many similar functions, there may be more than one combination of functions that fit the data and again the matrix becomes singular. This chapter only considers a response matrix with three very different response functions and therefore degeneracy should not be a problem.

Singular Value Decomposition is a powerful set of mathematical techniques for dealing with sets of equations or matrices that are singular or very close to singular and is the method of choice for solving most linear least squares problems. SVD methods are based on the theorem that any M×N matrix **A**, whose number of rows M, is greater or equal to its number of columns N, can be written as the product of an M×N column-orthogonal matrix **U**, an N×N diagonal matrix **W** with positive or zero elements, and the transpose of an N×N orthogonal matrix **V**.

$$\begin{bmatrix} \\ \mathrm{A} \\ \\ \end{bmatrix} = \begin{bmatrix} \\ \mathrm{U} \\ \\ \end{bmatrix} \cdot \begin{bmatrix} w_1 & & \\ & \cdots & \\ & & w_N \end{bmatrix} \cdot \begin{bmatrix} \\ \mathrm{V}^{\mathrm{T}} \\ \end{bmatrix}$$

Equation 6.1 Singular Value Decomposition of an M×N Matrix

Hence to find the inverse of matrix **A**;

$$\mathrm{A}^{-1} = V \cdot \left[diag\left(1/w_j \right) \right] \cdot \mathrm{U}^{\mathrm{T}}$$

Equation 6.2 To calculate the inverse of a matrix

The only thing that can go wrong with this construction is if one of the w_j's is zero. If more than one of the w_j's are zero, or very close to zero, the matrix is said to be more singular. Therefore by using SVD it is clear where the problem lies when finding the inverse of a singular matrix. If the matrix is singular and we wish to minimise the solution, then replace $1/w_j$ with zero if $w_j = 0$. Effectively, this is the same as ignoring the equation that is causing the singularity and therefore, if a matrix is degenerate i.e. has many singularities (many similar responses), the technique may produce erroneous results.

For the spectral deconvolution of an unknown spectrum, the matrix **A** would contain, of the order of 500 response functions, each one varying only slightly from the next. Therefore it may be envisaged that, in this scenario the number of singularities would be many and therefore the solution of this technique may be meaningless if a solution can be reached at all. Therefore the non-linear, *expectation maximisation* technique was used to deconvolve the real energy-loss spectra from the 7-element array as demonstrated in the previous chapter.

In this chapter, the simulated response of 3 different geometry detectors, to a trichromatic flux, is considered. Since the incident spectrum is known and can be designed so that the response of the detector, to each line, is very different, then it is convenient to use the SVD technique. In addition when a fit has been obtained using SVD, the errors on the fit are more readily calculated, than in the case of non-linear iterative routines.

The columns of the matrix **V** are an orthonormal set of M vectors, which are the principal axes of the $\Delta\chi^2$ = constant ellipsoid. The lengths of these axes are inversely proportional to the corresponding singular values $w_1 \ldots w_M$. the boundaries of the ellipsoid are given by:

$$\Delta\chi^2 = \omega_1^2 \left(V_{(1)} \cdot \delta a\right)^2 + \cdots + \omega_M^2 \left(V_{(M)} \cdot \delta a\right)^2 \qquad \textit{Equation 6. 3}$$

Where δa is a change in a parameter a.

The formula for the covariance matrix[C] is:

$$C_{jk} = \sum_{i=1}^{M} \frac{1}{\omega_i^2} V_{ji} V_{ki} \qquad \textit{Equation 6. 4}$$

The error on the solution is the square root of the covariance for that vector or response function [83].

6.3 Deconvolution of the Simulated Response of the Detectors, to a Trichromatic flux

The three detector geometries are based on the use of hexagonal CsI(Tl) crystals with a 2cm AF dimension. A complete array of crystals may be made from 7, 19 or 37 elements. Thus the three array geometry's that have been simulated are:

- 7 elements with a depth of 5cm
- 19 elements with a depth of 1.84cm
- 37 elements with a depth of 0.95cm

The response of the detectors was simulated at 1.0, 4.44 and 6.13MeV, using the GEANT Monte-Carlo package. The response was calculated assuming the flux to be uniform, parallel and incident on the front face of the detector. The energy resolution of the detectors was assumed to be the same as that measured for the 7-element array described in Chapter 4. The response spectra were then compiled into a response matrix for each detector. The flux consisted of an equal number of 1, 4.44 and 6.13 MeV photons. The total flux incident onto the front face of the 5cm deep detector was 3×10^6 photons, this corresponds to a total flux of 8.14×10^6 photons incident on the 1.94cm deep detector and 15.86×10^6 photons incident on the 0.94cm deep detector. The simulated energy-loss spectra and the fitted energy-loss spectra from the 5cm, 1.84cm and 0.94cm depth detectors are shown in Figure 6.1, Figure 6.2 and Figure 6.3 respectively.

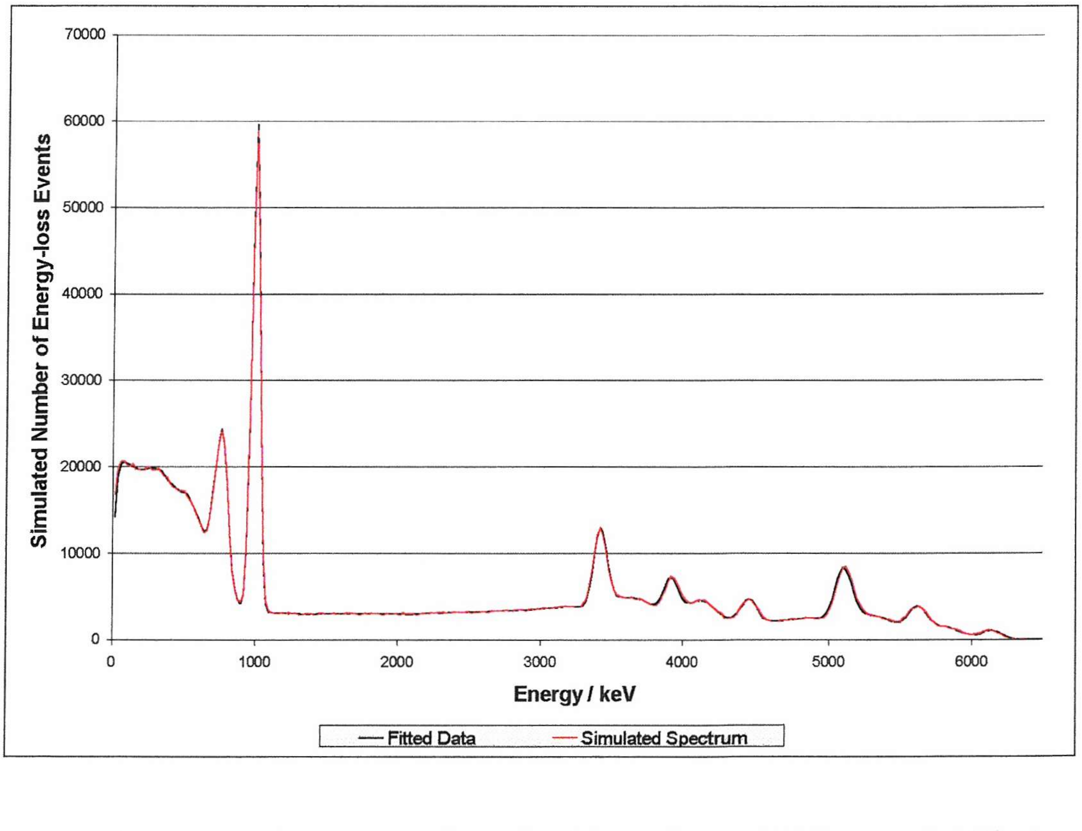

Figure 6.1 The Simulated Response of a 0.5kg, 0.94cm Deep. 37 Element, CsI(Tl)-Array to a trichromatic Flux of 1MeV, 4.44MeV and 6.13MeV photons.

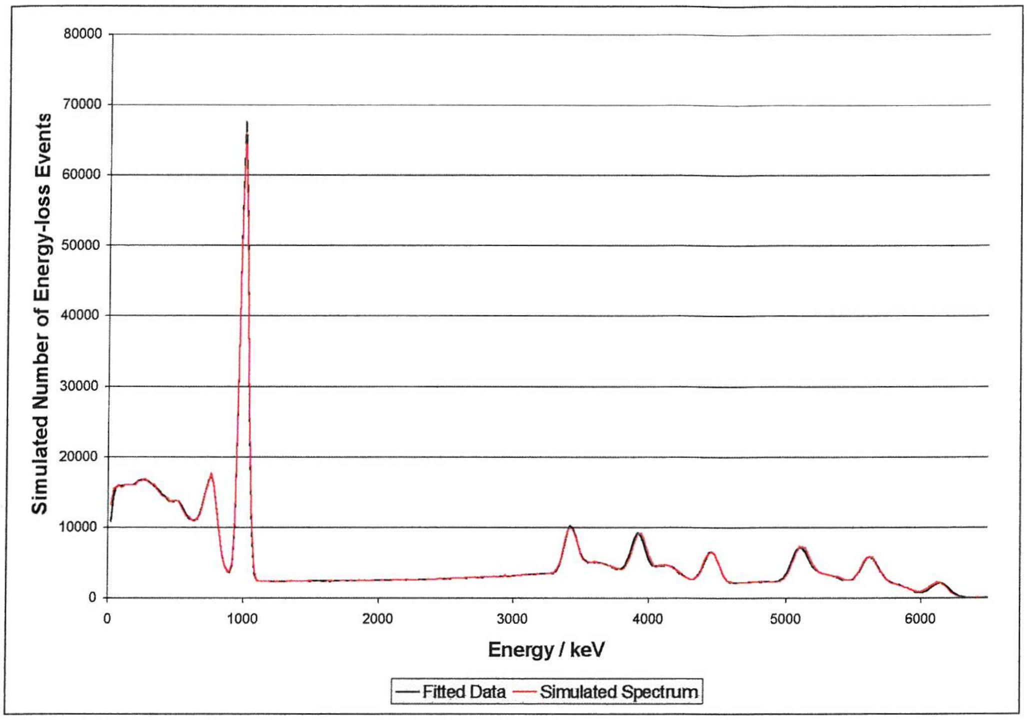

Figure 6.2 The Simulated Response of a 0.5kg, 1.84cm Deep. 19 Element, CsI(Tl)-Array to a trichromatic Flux of 1MeV 4.44MeV and 6.13MeV photons.

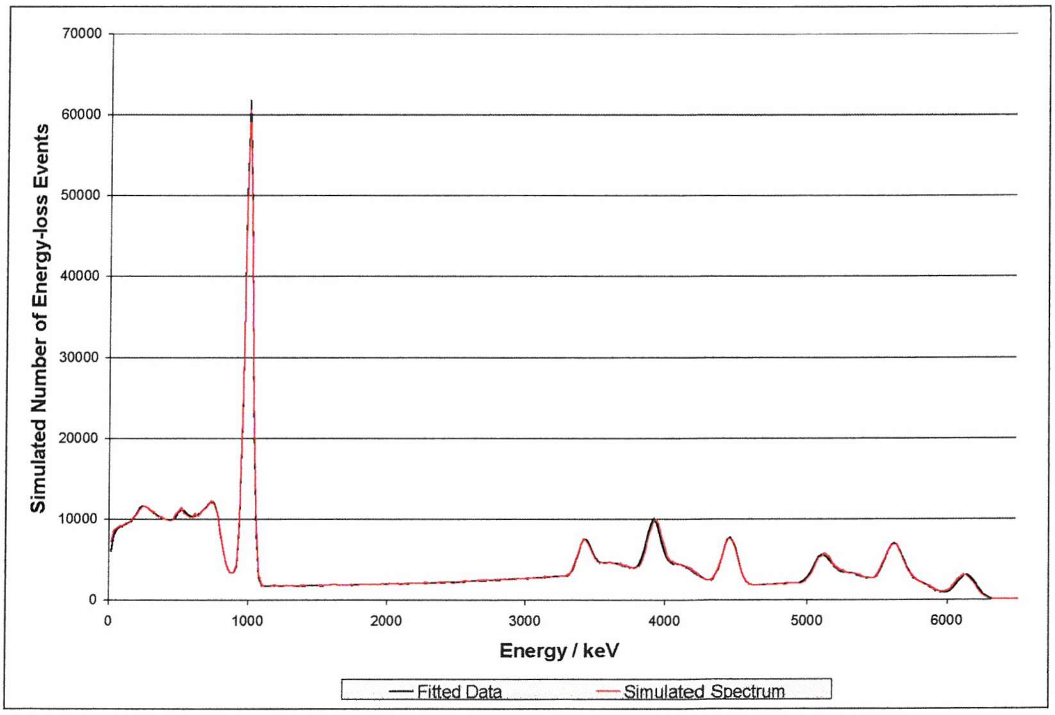

Figure 6.3 The Simulated Response of a 0.5kg, 5cm Deep. 7 Element, CsI(Tl)-Array to a trichromatic Flux of 1MeV, 4.44MeV and 6.13MeV photons

The response and the energy-loss spectrum, for each detector, are generated from the same computer model and therefore there can be no systematic errors associated with the fitting routine. Thus the only differences between the energy-loss spectra and the fitted spectra are due to statistical variations in the number of energy-loss events occurring in each channel. Likewise the error associated with the predicted flux is solely due to statistical variations.

As may be expected, the routine deconvolves the simulated energy-loss spectra, leaving residuals that arise as a consequence of statistical variations in the recorded spectrum. However, it is not the actual value of the deconvolution that demonstrates the sensitivity of the detector, rather it is the error on the predicted value that leads to the conclusion as to which detector is the more sensitive. Table 6.1 is a summary of the deconvolution results, which are shown graphically in Figure 6.4 From the results of the simulations it is fairly obvious and not surprising that the sensitivity of the detector decreases with increasing photon energy. However, it may also be seen, from the 1MeV and 4.44MeV flux, that the standard error is lower for a broad thin detector and hence the sensitivity is higher.

Detector Depth	5cm deep detector 1×10^6 photons		1.84cm deep detector 2.7×10^6 photons		0.94cm deep detector 5.29×10^6 photons	
Energy	Predicted Flux	Error (%) 1 S.D.	Predicted Flux	Error (%) 1 S.D.	Predicted Flux	Error (%) 1 S.D.
1.00MeV	1001672	0.138	2707936	0.124	5301210	0.1186
4.443MeV	999145	0.161	2699417	0.154	5294897	0.1525
6.129MeV	999145	0.236	2697426	0.241	5283521	0.2553

Table 6.1 The standard error on the SVD fit to the simulated spectra

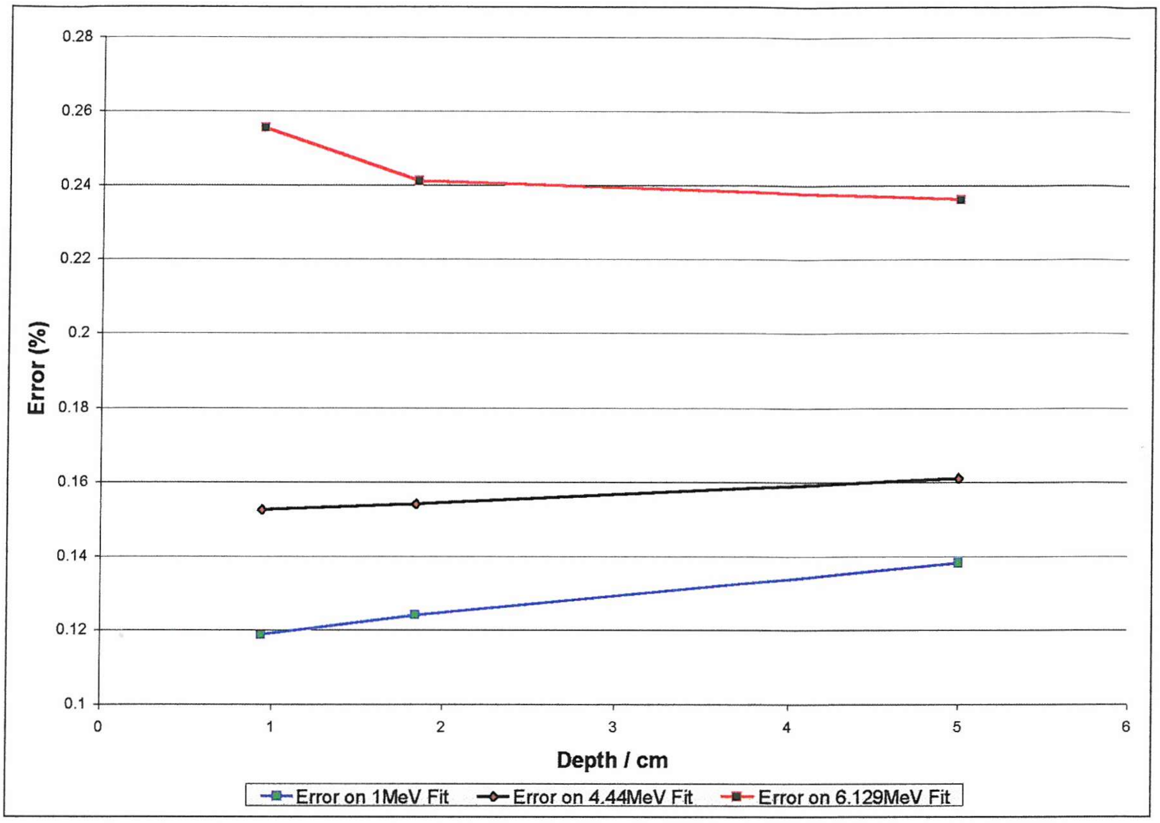

Figure 6.4 The Error on the Predicted Flux for Each Detector

Detector Depth	Number of Energy-loss Events above 4.6MeV
0.94cm	217429
1.84cm	243575
5cm	246804

Table 6.2 The number of energy-loss events above 4.6MeV

The slope of the 1MeV error line is steeper than that for the 4MeV line and therefore leads to the logical conclusion that for lower energy photons the effect of making the detector broad and flat is comparatively greater than for higher energy lines. This is in agreement with the findings of Armantrout et al. [66] who considered the effect for photons at 511keV.

The error in the deconvolution of the 6.13MeV line is increased for the thinner detector and thus the sensitivity has decreased. This may be due to the fact that the spectrum above 4.6MeV is solely due to the energy-loss events from the 6.13MeV line and therefore there is no additive statistical noise from other gamma ray lines. Thus a detector that has a higher proportion of gamma ray events in this region will have a lower error on the reconstructed flux. The 5cm detector has 13.5% more energy-loss events in the region from 4.6MeV to 6.2MeV, compared to the 0.94cm detector, which supports this theory. In addition it may be noted that the increase in the error between the 5cm detector and the 1.84cm detector, is not as great as the increase between the 1.84cm detector and the 0.94cm detector, again this could be explained by the number of events occurring above 4.6MeV. The sudden decrease, in the number of events occurring above 4.6MeV, for the 0.94cm detector, may be due to the escape of Compton recoil electrons from the crystal due to the depth of the detector being comparable to the path length of an electron of several MeV in CsI(Tl).

6.4 Reassessment of the Design of the CsI(Tl)-photodiode Array

The analysis described in section 6.4 leads to the conclusion that for a 1MeV gamma-ray line, a thin, large area detector, will provide a higher sensitivity to a normally incident flux than an equivalent mass detector with a greater depth and smaller area. Taking this conclusion to the extreme, it could be envisaged that an extremely thin detector of very large area could be constructed to provide the best sensitivity for a given mass. This assumption however relies on the response function for the detector being perfect and hence the error on the reconstructed spectrum being entirely due to statistical noise. In reality, this will not be possible and systematic effects will also be included in the confidence limits for the reconstructed spectrum. In addition, the lack of any features in the response of the detector will result in a high degree of degeneracy, between the various response spectra. There will therefore be an optimum depth which is a balance between having a high event rate and a reasonable photofraction, which will provide a response function with some features, that will aid in the reconstruction of the incident spectrum. The previous section assumed that all three detectors had the same energy resolution as the 5cm deep, 7-element array. This will not be the case and the shorter array will in fact have a better energy resolution due to a smaller aspect ratio, which in turn will result in a smaller variation in the transfer-variance of the detector. This factor will improve the sensitivity of the thin, large area array and should be taken into account when deciding on an optimum design. Practical construction considerations must also be taken into account when deciding on the optimum design. A very large area detector will require many more pixels. For example a 4kg mass of CsI(Tl) would consist of 61×5cm long crystals or 91×3.25cm long crystals or 127×2.33cm long crystals. Thus the complexity of making the array increases as the depth decreases.

6.5 Conclusions

It may be concluded that, for a detector with a perfect response function, the most sensitive geometry will be when the area is maximised and the depth is kept to a minimum. In reality, it will not be possible to produce a perfect response function and therefore the depth of an optimised detector will depend on the practical constraints. For a CsI(Tl) array it may be concluded that the maximum depth required is 5cm since it has been shown in the preceding chapters that it is entirely feasible to deconvolve the emission spectrum from a small array of such crystals. The new VA-TA ASIC [84] will make the construction of a large array more feasible since the front-end readout electronics can be incorporated onto a single electronic circuit board thus making the detector very compact. Therefore the construction of 91 or 127 element arrays should not pose a significant technical challenge. The ultimate deciding factor will be the accuracy with which, a complex energy-loss spectrum can be deconvolved. If the response matrix is close to ideal then, as demonstrated above, the detector can be made relatively thin and therefore an 8.6kg CsI(Tl) detector might consist of 127, 2.33cm long elements. However, a complex lunar energy-loss spectrum from such a thin array would become devoid of any features and hence may become difficult to deconvolve unless the response function was near perfect.

Consideration of the Geometry of the Spectrometer when Applying Deconvolution Techniques

Systematic differences between the response function and the real detector response cannot be modelled using a computer simulation. The only way of determining the overall effect of systematic errors will be to construct 3 prototype detectors and deconvolve complex energy-loss spectra from each detector. Such tests could be performed using a particle accelerator and a large soil target that would produce a gamma-ray spectrum similar to that observed to radiate from the lunar surface [1]. In general, it may be envisaged that a detector having a depth of only 1 to 3 cm depth of CsI(Tl) will produce a flat, featureless spectrum that will be difficult to deconvolve. Also it may be argued that to use more than 5cm depth is a waste of material since a 5cm depth detector produces a spectrum that contains sufficient features that may be deconvolved using iterative deconvolution routines.

Chapter 7

7 Radiation Depth Measurements and Deconvolution

7.1 Introduction

When measuring the radioactive contamination of soil, it is important to know the depth distribution of the contamination in order to calculate the levels of contamination present, the mechanisms by which the contamination has been transported and the rate at which the radioactive material is being dispersed [85]. It is not, in general, practical to survey a large area by taking samples back to a laboratory for analysis so it is necessary to devise a field instrument that can provide the information required, over a large area, in a reasonable time scale. A technique has been developed at the Kurchatov Institute, Moscow, for the in situ measurement of ^{137}Cs deposits in the contaminated region around the Chernobyl site [86]. This short chapter describes the Russian technique and considers if the technique may be improved by the application of the expectation maximisation deconvolution routine.

7.2 Depth Measurements using a Collimated 2" NaI(Tl)-PMT Spectrometer

To measure radionuclide soil contamination, using a gamma-ray spectrometer, it must be set up at a fixed position relative to the ground with a fixed field of view. The count rate of the detector, in the photopeak, will determine the activity of unscattered radiation. This may be the basis for deposit determination when radionuclides are concentrated in the top thin soil layer. However, in a real situation, radionuclides penetrate the soil resulting in an increase in scattered radiation and a decrease in the unscattered radiation. Thus using this approach it is impossible to define the degree of contamination without knowledge of the vertical distribution in the soil.

To measure the ^{137}Cs deposit taking into account its penetration depth in the soil it is necessary to determine the count-rate in the energy region 400-560keV and in the energy region 600-720keV. The region 600-720keV corresponds to the photopeak region of the spectrum and decreases with increasing mass of material between the source and the detector. In the region 400-560keV, two processes affect the intensity of the flux. Firstly, there will be a contribution arising from partial energy-loss events in the sensitive medium of the detector, this contribution will decrease for increasing depth of penetration corresponding to the decrease in the number of photons incident on the detector. Secondly, there will be a contribution from photons, which are scattered through a small angle, in the soil, before emerging from the surface, this component will increase with increasing depth of source. Therefore, the depth dependence of these two regions of the energy-loss spectrum is different and can be used to determine the depth of the contamination. The optimum boundaries of the energy range in the Compton part of spectrum (400-560keV) were determined on the basis of a numerical Monte-Carlo calculation and experimental modelling with a uniformly distributed ^{137}Cs source [87]. Once the depth of contamination is known the intensity of the source can be calculated using knowledge of the attenuation of 662keV photons in the soil and the response of the detector [88].

7.3 Depth Measurements Using a 1cc CsI(Tl)-photodiode Spectrometer

The spectral effects of varying depths of radioactive contamination have been simulated in the laboratory using a 10μCi laboratory ^{137}Cs radiation source with varying thickness of overlaying material between the source and the CsI(Tl) spectrometer [89]. Figure 7.1 shows the variation in the energy-loss spectra spectra with varying depth of water. Fresh water has a density of 1gm/cc so the conversion from mm of water to gms/cm^2 is very simple so that 54mm of water is 5.4gms/cm^2 of material between the source and the detector.

It may be seen in Figure 7.2 that the relationship between the ratio of the two regions of interest and the depth of material between the source and the detector is linear. This ratio therefore provides a relationship between the observed energy-loss spectrum and the depth of the radiation source that is independent of the source intensity. This relationship has been successfully used to map large areas of contaminated soil in the region of Chernobyl [90]. As may be seen, the measured points do not deviate significantly from the linear trend line. Therefore, in this scenario, the depth of the source could be located to within 3 to 4mm assuming the relationship $y=0.0544x + 0.6558$.

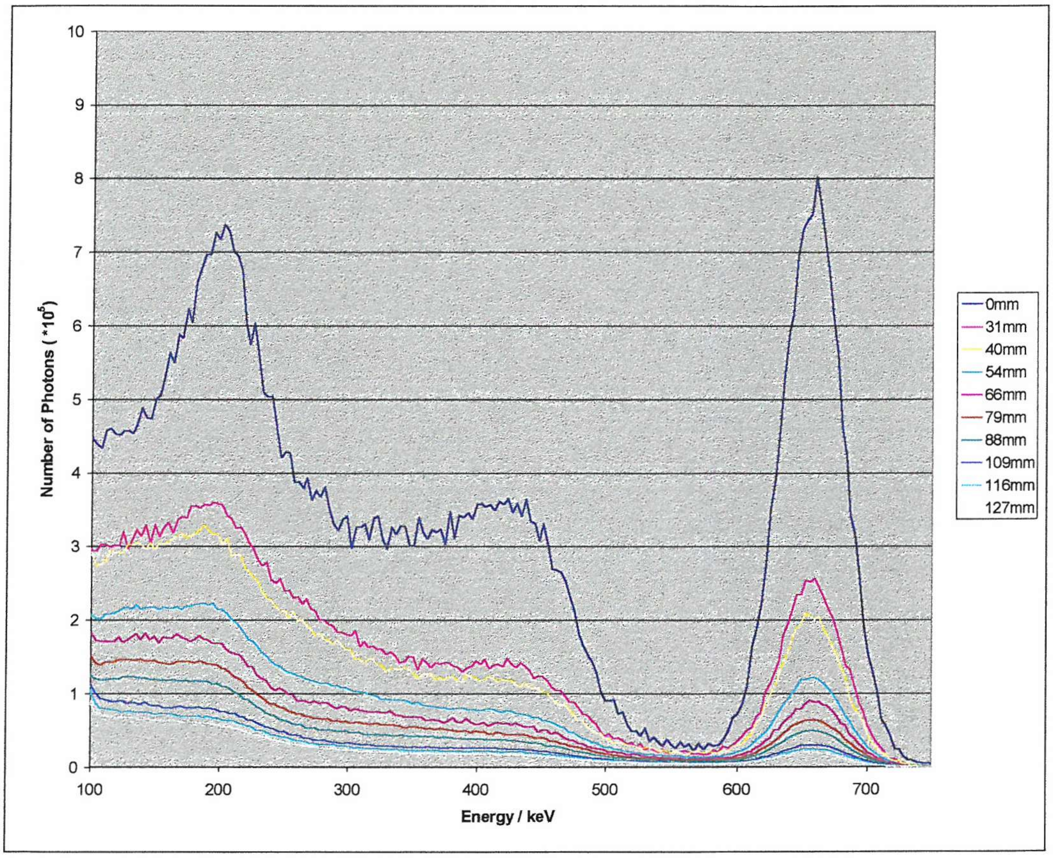

Figure 7.1 The Energy-loss Spectra from a CsI(Tl) Spectrometer Observing a Cs137 Source with Varying Depths of Water between the Source and Detector.

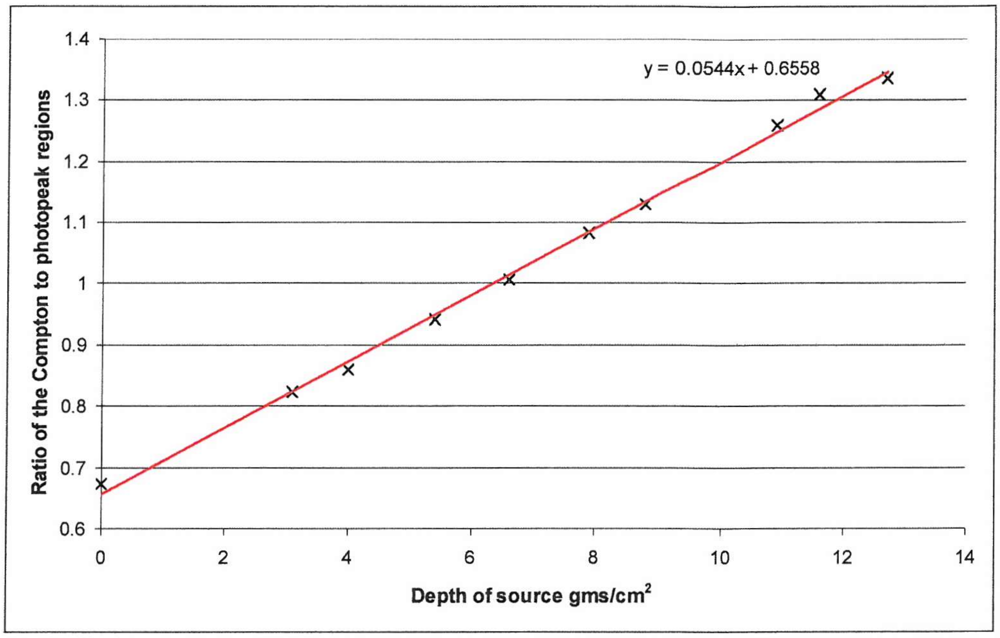

Figure 7.2 The ratio of the number of counts in the energy region 400-560keV to the number of counts in the energy region 600-720keV for varying depths of water.

7.4 Deconvolution of the Cs^{137} Spectra

The measured spectra were deconvolved using the expectation maximisation iterative least squares fitting routine. The aim of the deconvolution was to try to improve the contrast between the spectra, especially in the region from 400 to 600keV and to deconvolve the absolute flux incident on the detector. First examination of the deconvolved spectrum in Figure 7.3 shows a satisfactory solution, where the predicted number of events incident on the detector approximates, to the number of events expected, when considering the strength of the source and its distance from the detector. Also the ratio of the number of scattered to unscattered photons produces a linear relationship as shown in Figure 7.4, with smaller deviations than in the case of the raw spectra. However, closer inspection of the deconvolved spectrum reveals features in the energy region between 100-600keV that cannot be reasonably accounted for by consideration of the scattering of photons in the water, especially the feature in the energy region 470-600keV. These features are almost certainly due to small differences between the simulated response function and the real response of the detector. This may be due to differences between the simulated geometry of the apparatus and the real geometry, small imperfections in the performance of the detector, such as gain drift, or could be due to small inaccuracies in the particle transport libraries used to predict the behaviour of high-energy particles. Therefore to overcome these differences would require making the simulated response and the detector response exactly the same, as task that may not be possible in practice.

It may be concluded that deconvolution of these spectra provides no advantage for the purpose of producing the linear relationship between the scattered and unscattered flux, from which the radiation-source depth may be determined. However, difficulties will arise when there is more than one source, of different intensities at varying depths. In this scenario the spectrum may become difficult to interpret and it is this case that a deconvolution routine may prove useful.

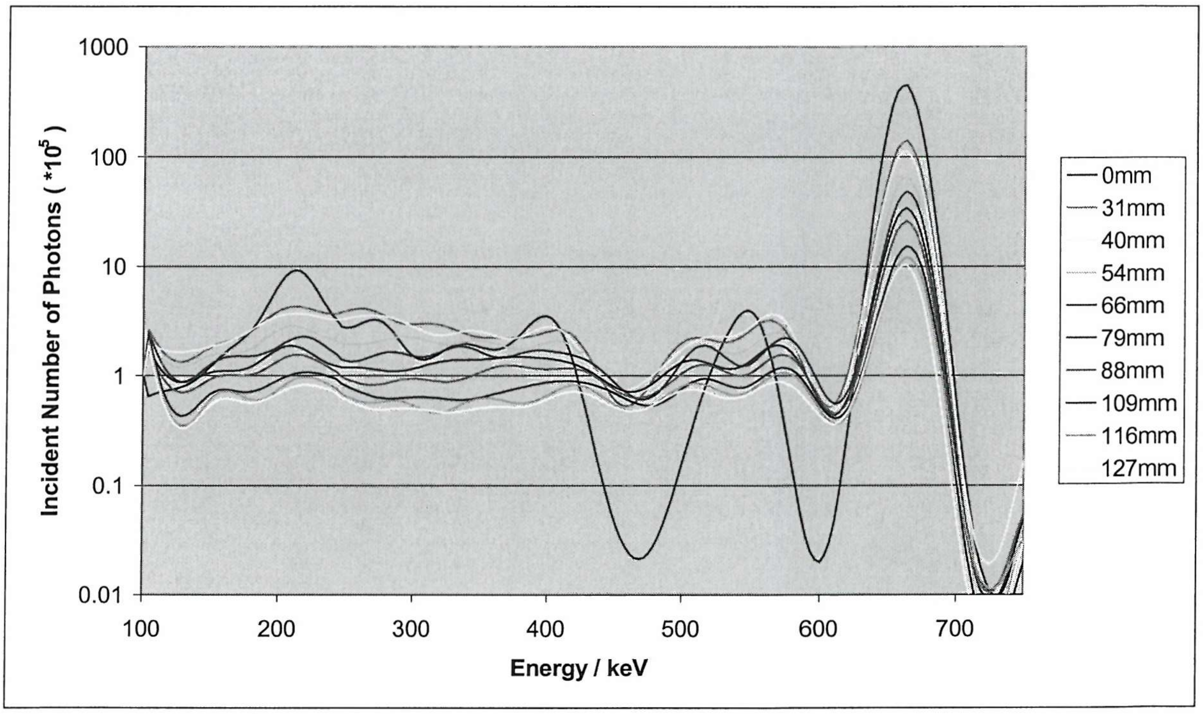

Figure 7.3 Deconvolved Energy-Loss Spectrum from a CsI(Tl) Spectrometer Observing a Cs^{137} Gamma-ray source with Varying depth of Water between the Detector and the Source.

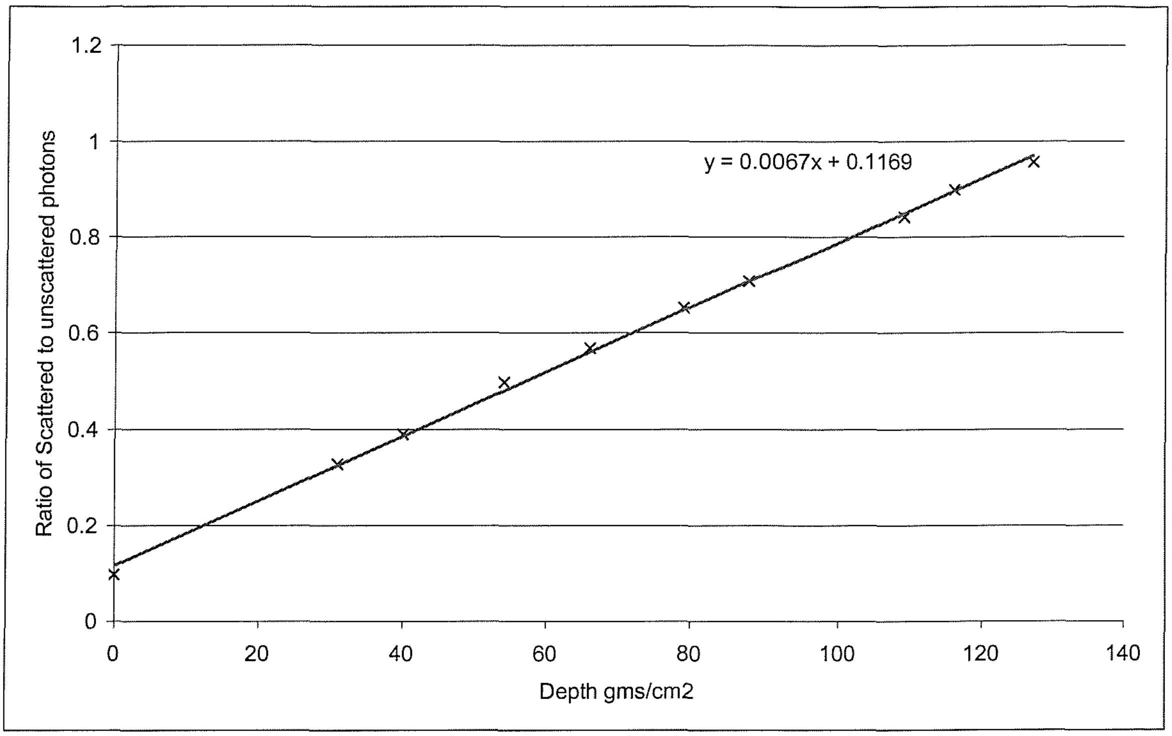

Figure 7.4 The deconvolved ratio of the number of scattered photons to unscattered photons incident on the detector for varying depths of water.

7.5 Further Work and Future Developments

The mass of material between a radiation source and a gamma-ray detector may be determined using the technique outlined above. However, this process may become difficult when many sources are present having a range of intensities and depth distributions. It is in this scenario that it is envisaged that an iterative routine may be used to deconvolve the depth and distribution of the radiation sources. The response function for the deconvolution process may be compiled from measured calibration spectra such as those shown in Figure 7.1. The routine could then determine the number, intensity and distribution of radiation sources by iteratively varying these factors until it achieved a maximum likelihood fit to the observed spectrum. To complete the information required to determine the radiation contamination concentration profile, the mass of material between the detector and the source would need to be converted into a depth profile. To do this, the density of the soil would need to be measured. However, the density of the soil will only vary with water concentration, therefore to measure the density of the soil would require a knowledge of the soil type and the water concentration in the soil.

7.6 Conclusion

This chapter has shown that the expectation-maximisation deconvolution routine is useful for determining the flux incident on a gamma-ray detector when measuring a radiation source with varying depths of water between the source and detector. It has also shown that there is a linear relationship between the predicted, scattered and unscattered flux, for varying depths of water. However, it may be argued that the relationship derived from the raw data provides the same amount of depth information as the relationship derived from the deconvolved spectrum and therefore there are no significant benefits when determining the depth of a single source. In addition, some artefacts appeared in the deconvolved spectrum due to small differences between the simulated response and the real detector response. It is believed that the features did not greatly affect the overall number of events in the deconvolved spectrum but may require more investigation in the future.

Finally, it has been considered that a deconvolution routine may be used to deconvolve the complex spectra, recorded as a result of observing many radiation sources, with varying intensity and spatial distribution. The beauty of this technique would be that it would not require any special equipment but may be used with a fairly simple CsI(Tl)-photodiode spectrometer. Calculation of a new response function could also result in the technique being applied to the most commonly used 2" and 3" NaI(Tl)-PMT spectrometers.

Chapter 8

8 A Large Area CsI(Tl)-photodiode Array for Explosives Detection

8.1 Introduction

The previous chapters have detailed the design, construction and testing of a small CsI(Tl)photodiode array for remote geochemical analysis from an orbiting satellite. However, the technology developed for planetary science may be applied to terrestrial applications such as remote detection of explosives by neutron activation analysis. This chapter outlines a design for a large area, position-sensitive gamma-ray spectrometer for use in imaging explosive materials. The multi-element detector system, when used in conjunction with a coded-aperture mask, would be able to provide a "multi-colour" image of a scene when illuminated by a neutron source. The feasibility of using such a system to identify the unique elemental composition and location of explosive materials is discussed.

Due to the ease with which illicit materials can be concealed within shipping containers and the difficulty of manual inspection, a need has arisen for a fast, non-invasive method for the detection of these hidden substances. Several techniques have been proposed, based on the neutron irradiation of the container and examination of the resultant gamma-ray spectrum [90]. Due to the penetrating nature of neutrons, they can probe up to 2 to 3 meters into the container and the resultant gamma-ray spectrum provides the specificity necessary for the identification of the elemental composition of the materials within the cargo. The elemental composition of many of the particularly sensitive contraband materials differs markedly from the broad range of materials found in legitimate cargo. For example, the common feature of many explosive materials is a low C/N ratio combined with a similarly low C/O ratio [91]. The instrumental challenge is therefore to create an image of the contents of the container, with both a spatial and energy-resolution, sufficient for the detection of the hidden materials, within a realistic observation time. This paper aims to show that the combination of a large CsI(Tl)-photodiode array with a coded mask, and a pulsed neutron source, would provide sufficient spectral and spatial resolution to identify relatively small quantities of explosive, hidden within a cargo container.

A source of fast neutrons produced, for example, using a sealed, low-voltage D-T source, will generate typically 10^{11} neutrons/s over 4π steradians at an energy of 14.3 MeV [92]. Such a neutron beam is able to penetrate into a cargo container, producing unique gamma-ray signatures that are able to emerge from deep within the cargo. Initially, prompt gamma-rays are generated through inelastic scattering off the target nuclei then, as the neutrons thermalise, capture gamma-rays are produced followed by delayed gamma-ray emission from longer-lived activated nuclei. The development of the pulsed fast-neutron activation technique [93] enables one to separate the gamma-ray spectra resulting from these distinct emission processes simply by time-tagging the data. In some applications the time of arrival of the initial prompt gamma-ray signals has been used to find the depth of the interaction within the container and so provide some crude tomographic information.

In one example of the fast-neutron screening technique, the gamma-ray detectors are collimated to view the emission from different regions within the container, where the fan-beam of neutrons illuminates the cargo. The third dimension in the image is provided by the slow motion of the container through the beam. In this chapter, the feasibility is considered, of using two orthogonal, large coded-aperture gamma-cameras, capable of operating in the range between 2 and 12 MeV, to provide multi-colour 3-D images of a $30m^3$ volume within the container. Such a development should provide an improvement over the spatial resolution of existing techniques and should also speed-up the scanning process by widening the neutron beam and so avoiding the losses inherent in the current neutron-collimator design.

8.2 The Proposed Imaging Spectrometer

Most of the gamma-ray spectrometers described in the literature for large-scale neutron activation applications are based on the use of either sodium iodide scintillators or cooled germanium semiconductor detectors. Even though cooled germanium detectors have a much better energy resolution, the scintillator option is much more practical for field operations in which many collimated detectors are needed or fast timing is a requirement, as in Pulsed Fast Neutron Activation Analysis (PFNAA). In both of these detector options the energy-loss spectrum is complicated by the escape peaks, which arise as a consequence of the pair-creation and subsequent positron-annihilation processes. It is not practical to minimise this by enlarging the sensor in these two most common detector options. It is therefore proposed to use a multi-element, caesium iodide, scintillation counter in which the individual elements are viewed by large-area photodiodes. This combination of higher stopping power, better scintillation efficiency and higher quantum efficiency, along with the ease of tessellation of the detection elements, to form a large area array, provides us with a marked improvement over the use of conventional sodium iodide detectors. The ability to use such a position-sensitive array in an imaging system provides a more marked advantage. Such a large detector array combined with a coded- mask enables one to design a large aperture imaging system able to provide good angular resolution. For this application, gamma-ray emissions will be imaged in the range from 2 to 12 MeV so the crystal array needs to be designed to maximise the number of full-energy deposit events. However, in order to maintain a good light-collection efficiency and hence energy-resolution, the aspect ratio of the CsI(Tl) crystals should not exceed 3 to 1. That is, the length of the crystal should not exceed three times the width. Thus the dimension chosen for each of the hexagonal detector elements was 10cm long by 3.5cm across flats.

8.3 Read-out System

Recent developments in the design of multi-channel, low-noise, readout systems for an array of scintillation detectors, now makes it feasible to envisage the use of a detector array incorporating a few hundred elements. The outline design for the imaging system described in this chapter is based on the use of the recently developed VA-TA multi-channel amplifier chip manufactured by IDEAS [84]. This device is a self-triggered 32-

channel pre-amplifier, shaping-amplifier and sample-and-hold circuit. It has an input rms noise level of 40+12e/pF and a shaping-time of between 1 and 3 μs. The chip also provides a fast analogue sum of all 32 channels so that one can apply an energy-threshold requirement before reading out the analogue shift-register which has stored the individual energy deposits in a region of the array. A similar 64 channel chip has been packaged, which provides the choice of either serial or parallel outputs, and this is working well. It is expected to fabricate the electronics for the proposed imager in a similar way using the new VLSI circuit. With this circuit, it will be possible to identify the prompt gamma-rays from those, which arrive later, after thermalisation and neutron capture. The control logic needed to provide the necessary delay between the trigger-signal and the application of the hold signal together with the read-out pulse sequence will be provided within a single additional chip.

8.4 Simulation of the Gamma-ray Spectrum from a Fertiliser Bomb

A 14.3MeV monochromatic flux of neutrons was assumed to illuminate a 30 m^3 volume within a cargo container. Placed within this container was $0.22m^3$ (≈400kg) of ammonium nitrate, the principal constituent from which a fertiliser bomb may be made, this is shown in Figure 8.1. A Monte Carlo neutron-transport, code was used to predict the total emergent gamma-ray spectrum shown in Figure 8.2. The strength of the main gamma-ray features are listed in Table 8.1. The emerging spectrum has been divided into the fast neutron flux arriving within 4μs and the thermal neutron flux arriving after 4μs. These are shown in Figure 8.3and Figure 8.4.

Examination of the thermal neutron flux spectrum shows that it includes a very strong hydrogen line at 2.22 MeV and two pairs of nitrogen emission lines at approximately 5.2 MeV and 5.5 MeV. Using a CsI(Tl)-photodiode array, it is possible to achieve an energy resolution of ≈3% at 5MeV, which is sufficient to resolve this pair of lines. If both these lines are detected, it is a clear indication of a localised concentration of nitrogen within the cargo. In order to observe the presence of oxygen it is necessary to examine the fast neutron-induced gamma-ray spectrum. The characteristic strong oxygen line can be seen at 6.129 MeV. It should be noted that because of the design of the imaging detector, there is very little confusion between the escape gamma-ray features in the oxygen spectrum and the nitrogen feature at 5.5 MeV.

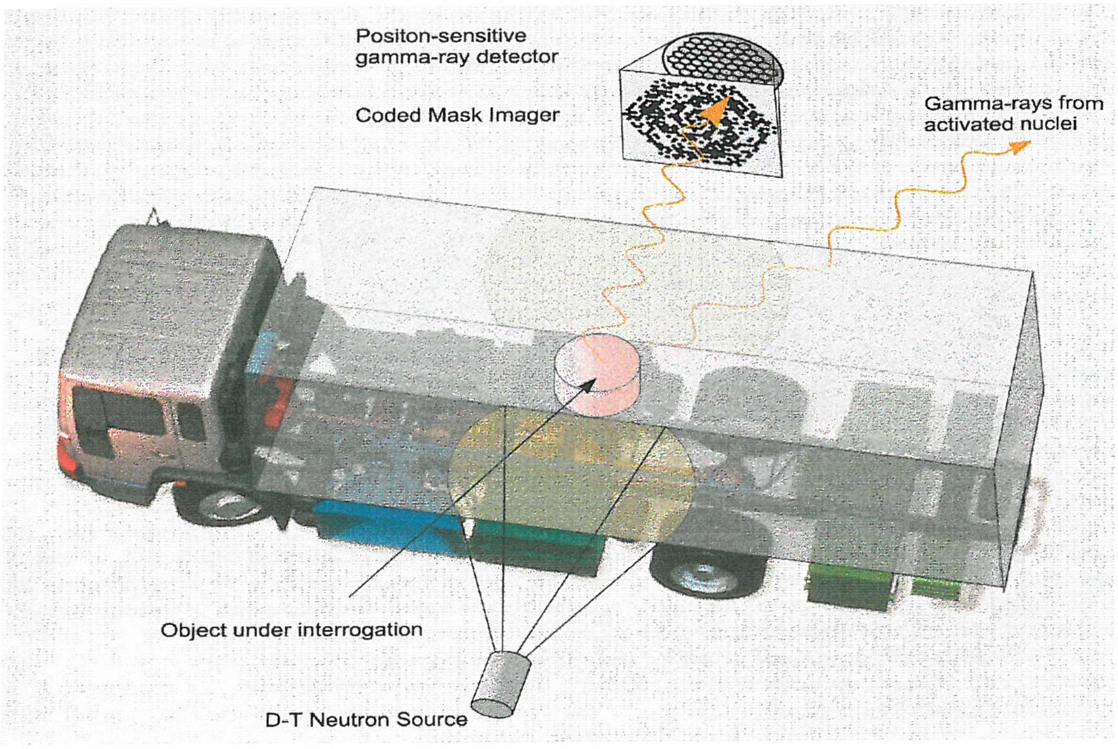

Figure 8.1 The Simulated Scenario for Concealed Explosives Detection

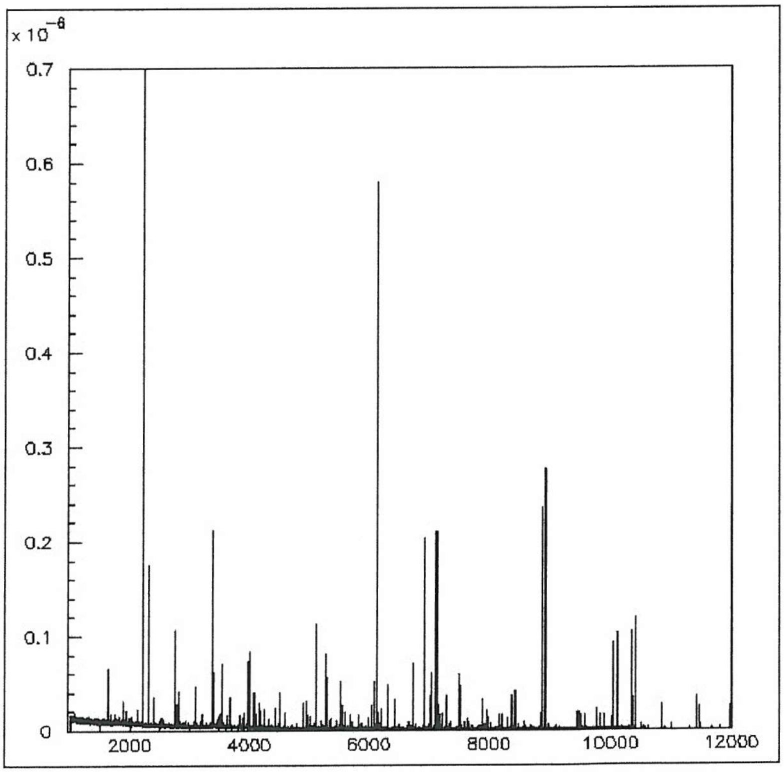

Figure 8.2 The total flux radiating from the explosive. The energy is in keV. The flux is per activating neutron

Element	Mechanism	Energy keV	Flux per neutron
Hydrogen	Thermal Capture	2220	1.8×10^{-5}
Oxygen	Fast Scattering	6129	6×10^{-6}
Nitrogen	Thermal Capture	5269	8.3×10^{-7}
Nitrogen	Thermal Capture	5279	5.8×10^{-7}
Nitrogen	Thermal Capture	5533	5.3×10^{-7}
Nitrogen	Thermal Capture	5562	2.8×10^{-7}
Nitrogen	Thermal Capture	10829	2.8×10^{-7}

Table 8.1 The major lines from the activated explosive

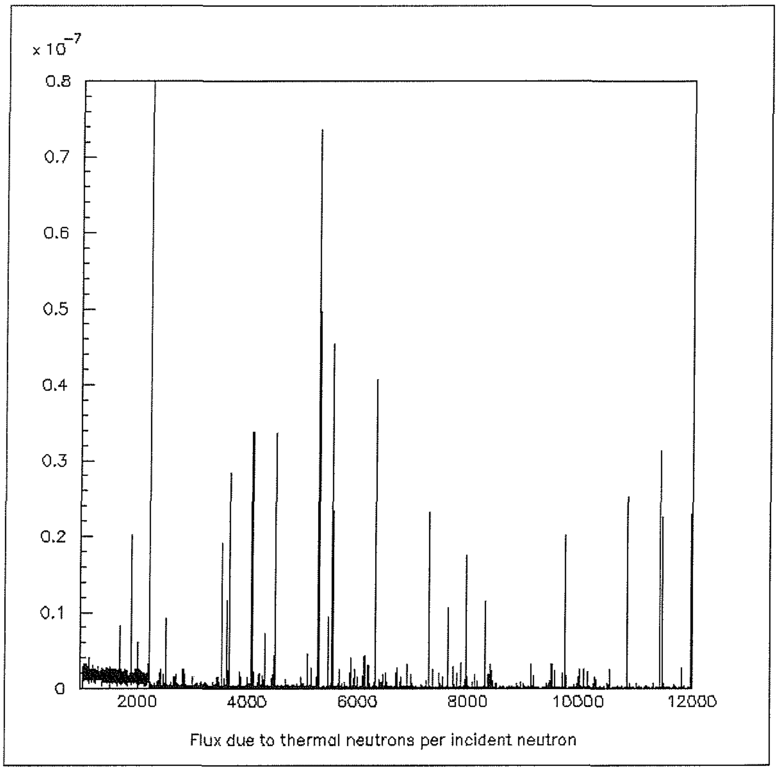

Figure 8.3 The flux due to thermal activation. The energy is in keV. The flux is per incident neutron

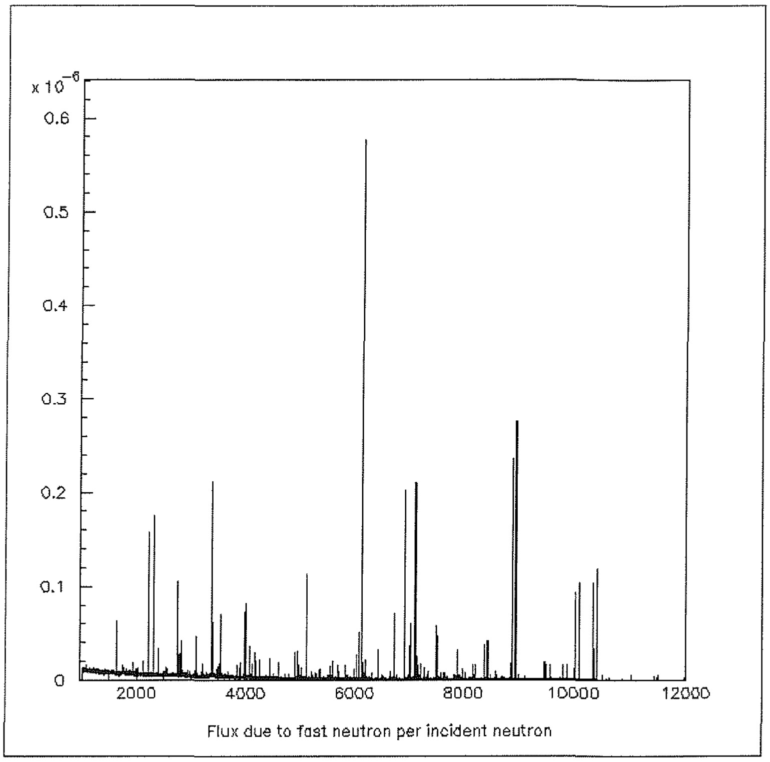

Figure 8.4 The flux due to fast neutron activation. The energy is in keV. The flux is per incident neutron.

8.5 Sensitivity Estimates

In order to estimate the sensitivity of the imager, we have assumed the use of a neutron source emitting 10^{10} neutrons per steradian per second for an exposure period of 30 seconds. A 271-element hexagonal detector array having an area of close to 3500 cm^2 and placed behind a coded-mask at a distance of 3m, was used in these simulations. Figure 8. shows the expected energy-loss spectrum from the thermal capture gamma-rays for a 30 second illumination of the explosive. The hydrogen and nitrogen features are clearly resolved. The oxygen feature at 6.129 MeV is clearly resolved in the prompt-neutron spectrum, Figure 8.6, after only a few seconds.

8.6 The Imaging Performance

Possibly the most important feature of this system, is its ability to image relatively small volumes within the scene under observation. Coded-aperture imaging systems may be based on the use of either a rectangular pixelated detector array or on ones having hexagonal symmetry. The optimum image quality is achieved by choosing the appropriate combination of uniformly-redundant coded mask with a suitably proportioned detection plane. For example, a 271 hexagonal detection elements arranged in a close-packed array is appropriate for use with a 1027 element hexagonal URA mask. An imager, based on a 271 elements array, viewing a 3x3m area at a distance of 3m would be able to provide an intrinsic spatial resolution of about 15 cm. In this case, the coded-mask would be located 58.6 cm in front of the detection plane. The sensitivity of the imager depends directly on the depth of modulation imposed by the mask elements on the incident photon beam. A 20 mm thick tungsten alloy mask attenuates approximately 80% of the incident photons at 6MeV

By setting an energy window around the important emission lines, it is possible to image the scene in different 'colours' and then to pay particular interest to those regions having a particularly suspicious elemental ratio. Clearly, the number of events detected within the H,O and N regions of the energy-loss spectrum do not themselves provide the relative elemental abundance's. This information would need to be deconvolved from the detector response and the neutron reaction cross-sections to provide the corrected ratios. This will provide a powerful method for detecting the presence of a wide range of illicit materials.

Figure 8.7, Figure 8.8 and Figure 8.9 show three images derived from the N, O and H emission lines. It can be seen that the images coincide and occupy a similar region of space. The image derived using the strong feature corresponding to hydrogen shows that the explosive occupies an area of approximately 4×4 pixels which corresponds to an area of 60x60 cm at the scene, which closely matches the size of the explosive charge. Whilst the coded-aperture imaging technique can, under certain circumstances, provide depth of focus information, for this application, a second orthogonal imager would probably provide the best quality information.

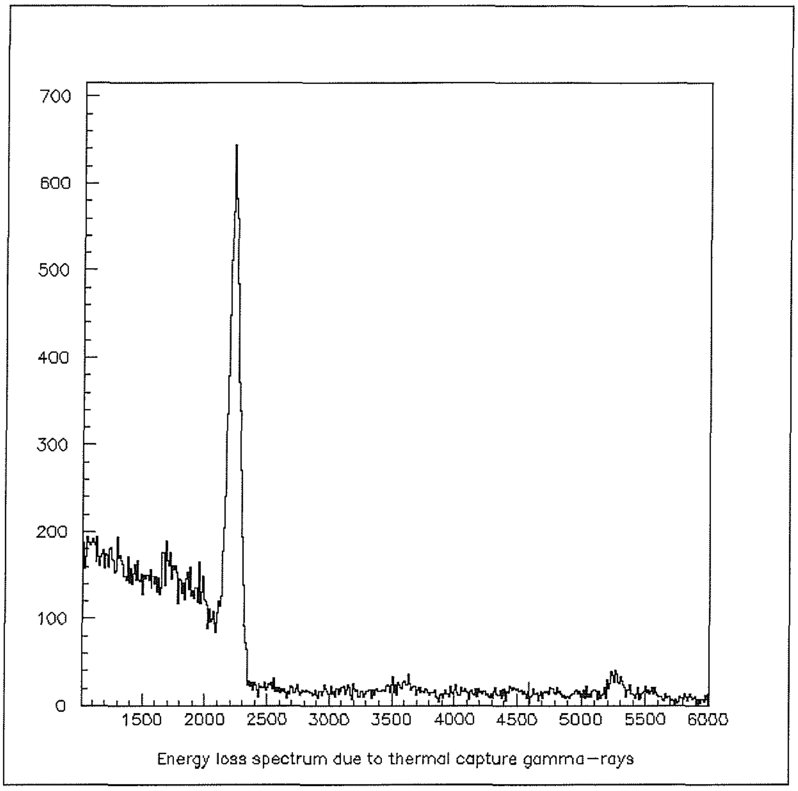

Figure 8.5 The energy-loss spectra from thermal neutron activation.

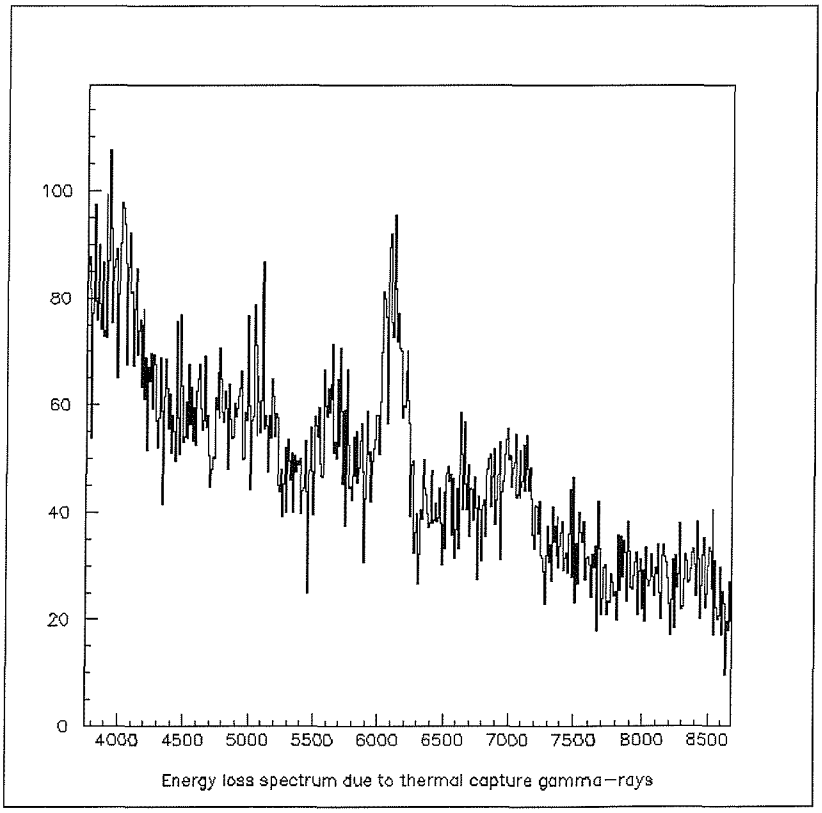

Figure 8.6 The oxygen photopeak from the fast neutron activation.

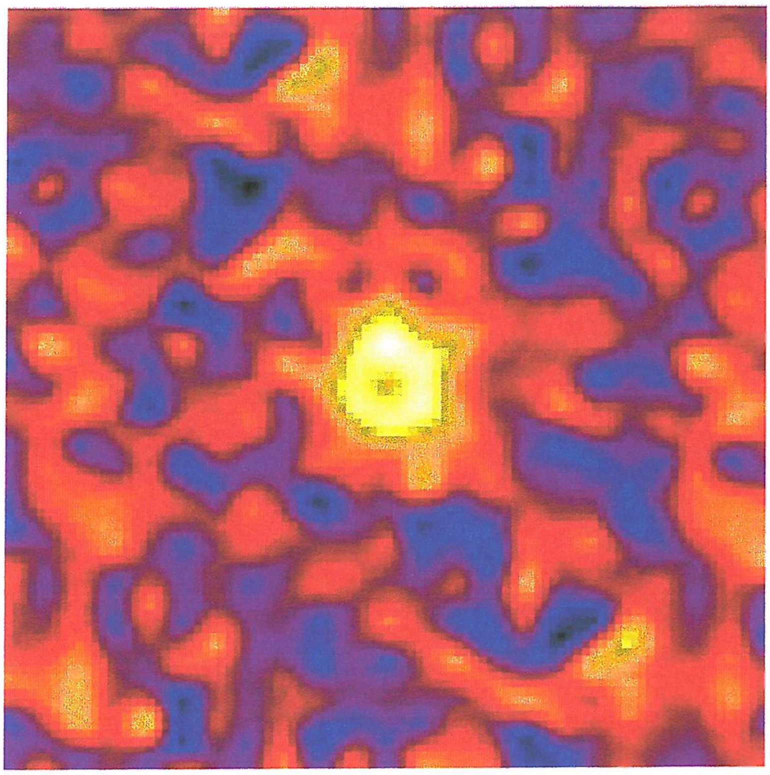

Figure 8.7 Showing the origin of the nitrogen photopeak

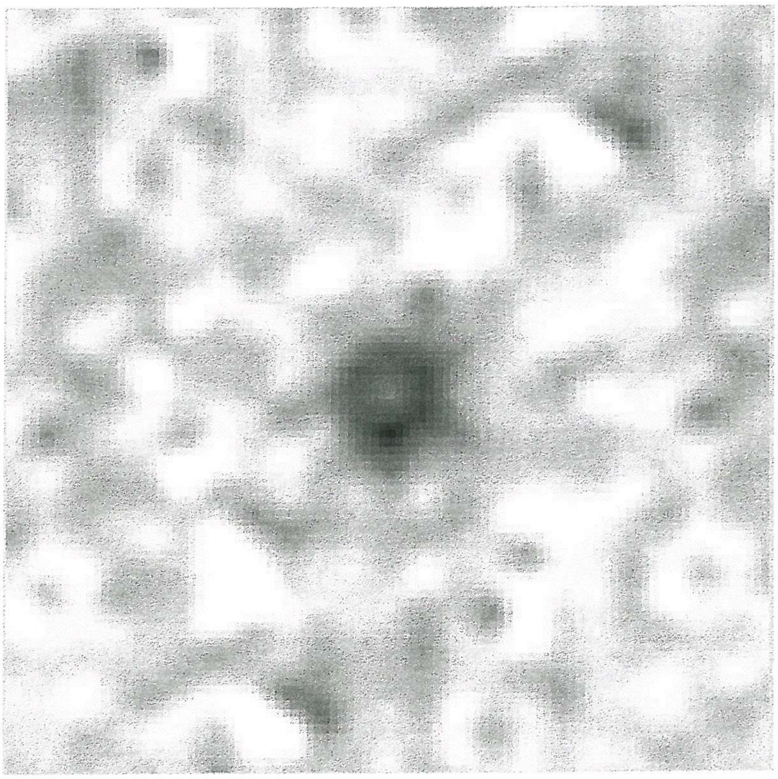

Figure 8.8 Showing the origin of the oxygen photopeak

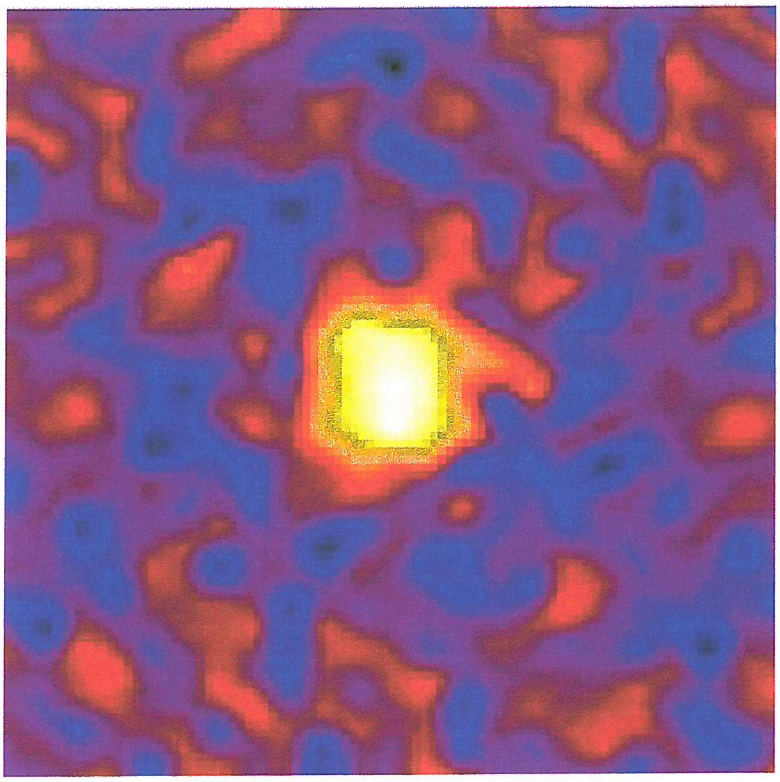

Figure 8.9 Showing the origin of the hydrogen photopeak

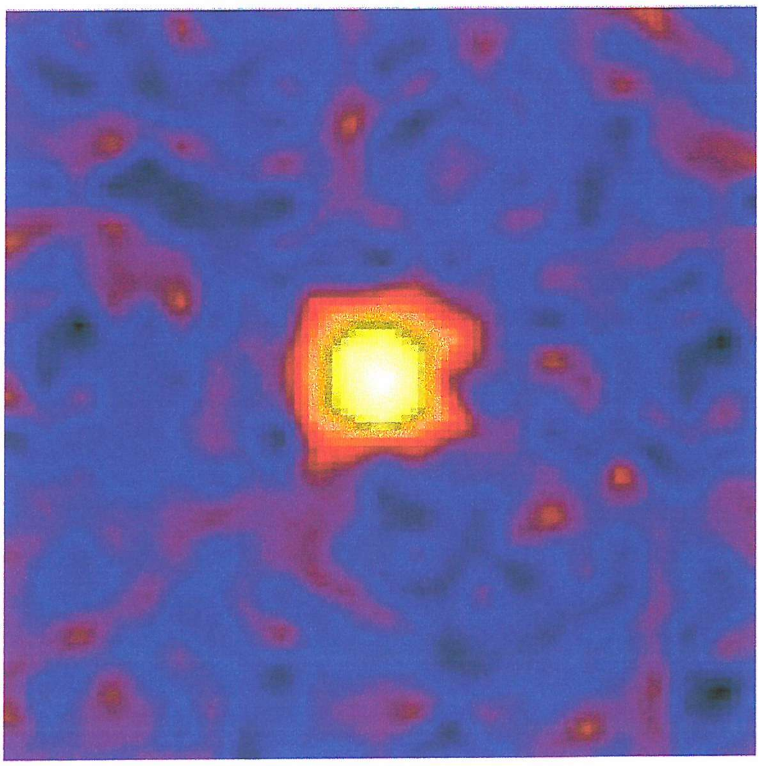

Figure 8.10 The Origin of the gamma rays generated by thermal neutron capture

8.7 Conclusions

It is recognised that the simulations described in this chapter are somewhat simplistic since no efforts have been made to conceal the explosive by the addition of other materials around the bomb. However, what has been demonstrated is that a large area CsI(Tl)-photodiode array coupled with a coded aperture mask has the potential to provide a sensitive, fast and effective method for the inspection of large cargo containers using neutron activation techniques. Further work could involve investigating the effect of placing a similar volume of ammonium nitrate in shipping containers filled with various concealing materials such as vegetables, scrap metal or sand. In addition, analysis of smaller containers such as suitcase sized objects, could be investigated since the probability of success is greater for smaller containers.

Bibliography

1. Bruckner, J., Masarik, J.; Planetary gamma-ray spectroscopy of the surface of Mercury, Planetary Space Science, Vol. 45, No.1, pp. 39-48, 1997.

2. Boynton, W.V. et al; Science Applications of the Mars Observer Gamma-ray Spectrometer. Journal of Geophysical Research-Planets, Vol. 97, No.E5, pp. 7681-7698, 1992.

3. Laplace, P.S., Exposition du System du Monde, English Translation by H.H Harte 1830, The System of the World, Dublin: Dublin University Press.

4. Cameron, A.G.W.; Origin of the Solar System, *Annual Review of Astrophysics and Astronomy*, 26, 441-72, 1988.

5. Henry, G.W, et al, Properties of Sun-like Stars with Planets: 51 Pegasi, 47 Ursae Majoris, 70 Viriginis and HD 114762, *The Astrophysical Journal*, 474, 503-510, 1997.

6. Cochran, W.D., Hatzes, A.P.; The discovery of a planetary companion to 16 Cygni B, The Astrophysical Journal, 483, 457-463, 1997.

7. Noyes, R.W. et al, A planet orbiting the star Coronae Borealis, *The Astrophysical Journal*, 483, L111-L114, 1997.

8. Wetherill, G.W.; Ways that our Solar System Helps us Understand the Formation of Other Planetary Systems and Ways that it Doesn't, *Astrophysics and Space Science*, Vol. 241, 25-34, 1996.

9. Lissauer, J.J, Planet Formation, *Annual Review of Astronomy and Astrophysics*, 31, 129-174, 1993.

10. Bush, S.G., Fruitful Encounters, The origin of the solar system from Chamberlin to Apollo, *Cambridge University Press*, pp.173, 1996. ISBN. 0-521-55214-1.

11. Hoyle, F.; On the origin of the Solar Nebula, *Q.J.Royal Astronomical Society*, Vol 1, 28-55.

12. Trombka, J.I.; Compositional mapping with the NEAR X-ray/gamma ray Spectrometer, *Journal of Geophysical Research*, Vol. 102, No. e10, Pages 23,729-23,750, 1997.

13. Gast, P.W.; Limitations on the composition of the upper mantle, *Journal of Geophysical Research*, 65, 1287-97, 1960.

14. Cameron, A.G.W.; *Ap. J. Lett.* 299: L83.

15. Stephenson, D.J.; *Icarus*, Vol 62, 4, 1985.

16. Sabu, D.D., & Manuel, O.K.; Xenon record of the early Solar system. *Nature*, 262, 28-32, 1976.

17. Cameron, A.G.W. & Truman, J.W.; The supernova trigger for the formation of the Solar System. *Icarus*, 30, 447-61, 1977.

18. Herbst, W. & Assousa, G.E.; Observational evidence for supernova induced star formation in Canis Major RI. *Astrophys. J.*, 217, 473-87, 1977.

19. Mahoney, W.A. et al; Diffuse galactic gamma-ray line emission from nucleosynthetic 60Fe, 26Al and 22Na: Preliminary results from HEAO-3, *Astrophys. J.*, 262, 742-8, 1984.

20. Clayton, D. D.; 26Al in the interstellar medium. *Astrophys. J.*, 280, 144-149, 1984.

21. Chamberlin, T.C.; The origin of the ocean basins and the planetessimal hypothesis, *Science*, 17, 300-301, 1903.

22. Russell, H.N.; Astronomical Books, (Review of the two solar families by T.C. Chamberlin), Saturday review of literature, 6, No. 1 (July 27, 1929), 7.

23. Anders, E; Meteorites and the Early history of the Solar System. in Origin of the Solar System (proceedings of conference held in 1962), ed. R. Jastrow & A.G.W.Cameron, pp95-142. New York: Academic Press (pub 1963).

24. Weidenschilling, S.J., Donn, B., Meakin, P.; Physics of Planetesimal formation, In *The Formation and Evolution of Planetary Systems* (H.A.Weaver and L.Danly, Eds), Cambridge University Press, Cambridge.

25. Cuzzi, J.N., Dobrolovolskis, A.R., Champney, J.; Particle Gas Dynamics in the Midplane of a Protoplanetary Nebula, *Icarus*, Vol. 106, pp. 102-134.

26. Reedy, R.C.; Planetary Gamma-ray Spectroscopy., Proceedings of the Lunar and Planetary Science Conference 9th, pp 2961-2984, 1978.

27. Rava, B, Hapke, B; An Analysis of the Mariner-10 Colour Ratio Map of Mercury, *Icarus*, Vol. 71, No. 3, pp. 397-429.

28. Balogh, A.; Mercury: The Planet and its Magnetosphere, Planetary Space Science, Vol 45, No. 1, pp1-2, 1997.

29. Bruckner, J., Masarik, J.; Planetary gamma-ray spectroscopy of the surface of Mercury, Planetary Space Science, Vol. 45, No.1, pp. 39-48, 1997.

30. Vilas, F.; Mercury, Vilas, F., Chapman, C.R., and Matthews, M.S., ed, University of Arizona Press, Tuscon, 1988.

31. Strom, R.G.; Mercury: An Overview, Advances in Space Research, Vol.19, No.10, pp. 1471-1485, 1997. And references therein.

32. Lewis, J.S.; Mercury. ed. Vilas, F., Chapman, C.R., Matthews, M.S., University of Arizona Press, Tuscon, pp. 651-666, 1988.

33. Huntress, W.T.; NASA's Strategy for Mars Exploration in the 1990's and Beyond. Advances in Space Research, Vol. 17, No. 12, pp. (12)7-(12)14, 1996.

34. Albee, A.L.; Mars Observer Mission. *Journal of Geophysical Research*, Vol. 97, No. E5, pp 7665-7680, 1992.

35. Urey, H.C.; The Origin and Nature of the Moon, *Endeavou*r, Vol. 19, pp. 87-99.

36. Orowan, E.; Density of the Moon and Nucleation of Planets, *Nature*, Vol. 222, pp 867, 1969.

37. O'Keefe, J.A.; The Origin of the Moon, Journal of Geophysical Research, Vol. 75, pp. 6565-74.

38. Cameron, A.G.W.; The Origin of the Moon and the Single Impact Hypothesis V, *Icarus*, Vol. 126, pp 126-137, 1997.

39. Taylor, S.R.; Lunar Science Institute Newsletter, Vol. 1, No. 4. 1969.

40. Lawrence, D.J., et al.; Global Elemental Maps of the Moon: The Lunar Prospector Gamma-ray Spectrometer, *Science*, Vol 281, pp 1484-1489, 1998.

41. Reedy, R.C. et al.; Expected gamma-ray emission from the lunar surface as a function of chemical composition, *Journal of Geophysics Research*, Vol.78, pp5847-5866, 1973.

42. Trombka, J.I., et al.; Analysis of Phobos Mission gamma-ray spectra from Mars. *In Proc. 22nd Lunar and Planetary Science Conference*, Lunar and Planetary Institute, Houston, 23-29, 1992.

43. Mitrofanov, I.G., et al.; High precision gamma-ray spectrometer PGS for Russian interplanetary mission to Mars, *Advances in Space Research*, Vol. 17, No. 12, pp(12)51-(12)59, 1996.

44. Hubbard, G.S., et al.; The Lunar Prospector discovery mission: mission and measurement description, *IEEE Transactions on Nuclear Science*, Vol. 45, No. 3, 1998.

45. Harrington, T.M., et al.; The Apollo Gamma-ray Spectrometer, *Nuclear Instrumentation and Methods*, Vol. 118, pp 401-411, 1974.

46. Metzger, A.E., et al.; Element Concentrations from Lunar Orbital Gamma-ray Measurements, *Proceedings of the Fifth Lunar Conference (Supplement 5, Geochimica et Cosmochimica Acta.)*, Vol. 2, pp. 1067-1078, 1974.

47. Bielefeld, M.J., et al.; Surface Chemistry of Selected Lunar Regions, *Proceedings of the 7th Lunar and Planetary Science Conference*, pp. 2661-2676, 1976.

48. Metzger, A.E., et al.; Thorium concentrations in the Lunar Surface. Regional Values and Crustal Content, , *Proceedings of the 8th Lunar and Planetary Science Conference*, pp 949-999, 1977.

49. Binder, A.B.; Lunar Prospector: Overview, *Science*, Vol. 281, 4th September 1998.

50. Lawrence, D.J., et al.; Global Elemental Maps of the Moon: The Lunar Prospector Gamma-ray Spectrometer, *Science*, Vol. 281, pp. 1484-1489, 1998.

51. Russell, C. T.; Forward, *Space Science Reviews*, Vol. 82, 1-2, 1997.

52. Cheng, A.F.; Near Earth Asteroid Rendezvous: Mission Overview, *Space Science Reviews*, Vol. 82, 3-29, *1997*.

53. Gold sten, J.O., et al.; The X-ray/gamma-ray spectrometer on the Near Earth Asteroid Rendezvous Mission, *Space Science Reviews*, Vol. 82, pp. 169-216, 1997.

54. Bruckner, J., et al; Radiation damage in germanium detectors : Implications for the gamma-ray spectrometer of the Mars Observer spacecraft, *Lunar and Planetary Science XXI*, 137-138, 1990.

55. Surkov, Yu.A., et al.; Determination of the Elemental Composition of Martian Rocks from Phobos 2, *Nature*, Vol. 341, pp. 598-600, 1989.

56. Masarik, J., Reedy, R.C.; Gamma-ray Production and Transport in Mars, *Journal of Geophysical Research*, Vol. 101, No. E8, pp. 18,891-18,912, 1996.

57. Langevin, Y.;The regolith of Mercury: Present Knowledge and Implications for the Mercury Orbiter Mission, *Planetary Space Science*, Vol. 45, No. 1, pp. 31-37, 1997

58. Carter, T.; The development of small CsI(Tl)-photodiode detectors for gamma-ray astronomy, Southampton University Thesis, May 1995.

59. Dorenbos, P. et al. Non-proportionality in the Scintillation Response and Energy Resolution Obtainable with Scintillation Crystals, *IEEE Transactions on Nuclear Science,* Vol 42, No 6, pp2190- 2202, 1995.

60. Mengesha, W., Taulbee, T.D., Rooney, B.D., Valentine, J.D.; Light Yield Nonproportionality of CsI(Tl), CsI(Na) and YAP, *IEEE Transactions on Nuclear Science*, Vol.45, No. 3, pp. 456-461, 1998.

61. Murray, R.B., and Meyer, A., Scintillation Response of Activated Inorganic Crystals to Various Charged Particles, *Phys. Rev.* Vol122, pp815, 1961

62. Valentine, J.D., Rooney, B.D, Li, J.; The Light Yield Nonproportionality Component of Scintillator Energy Resolution, *IEEE Nuclear Science Symposium,* Nov 11-14, 1997.

63. DeSalvo, R.; Why people like the hybrid photodiode, *Nuclear Instruments and Methods in Physics Research A*, Vol. 387, pp 92-96, 1997.

64. Brose, J., Dahlinger, G., Schubert, K.R.; Properties of CsI(Tl) crystals and their optimisation for calorimetry for high energy photons, Nuclear Instruments in Physics Research A, Vol. 417, pp 311-324, 1998.

65. Knoll, G.F.; Radiation Detection and Measurement, Second Edition, pp 53, *Wiley.* ISBN:- 0-471-81504-7.

66. Armantrout, G.A. et al. Sensitivity Problems in Biological Counting, *IEEE Trans of Nuclear. Science.* 1972(1) pp 107

67. Hubbard, G.S. ; Binder, A.B. ; Feldman, W. ; The Lunar Prospector Discovery Mission: Mission and Measurement Description, *IEEE Transactions on Nuclear Science,*Vol 45, No.3 1998.

68. Wormald, M.R.; Pair Spectrometer NaI(Tl) Array for Neutron-Induced Prompt Gamma-ray Analysis, Nucl. Geophys., Vol. 3, No. 4, pp. 373-380, 1989.

69. Jupp, I.D.; The Optimisation of Discrete Pixel Coded Aperture Telescopes, Southampton University Thesis, September 1996.

70. Bergson-Willis, s., et al.; INTEGRAL, Report on the phase A study, SCI(93)1 April 1993.

71. Bird, A.J. CsI(Tl) Detector Elements for the INTEGRAL Project. *Final report on Phase A studies*. October 1993.

72. Vijaya, A.D., Kumar, A.; The neutron Spectrum of Am-Be Neutron Sources, *Nuclear Instruments and Methods*, Vol. 111, pp 435-440, 1973.

73. Knoll, G.F.; Radiation Detection and Measurement, Second Edition, pp 730-731, *Wiley*. ISBN:- 0-471-81504-7.

74. Reedy, R.C.; Nuclide Production by Primary Cosmic-ray Protons, *Journal of Geophysical Research*, Vol. 92, E697-E702, 1987.

75. Green, A.R., Lei, F., Bird, A.J., Dean, A.J.; Performance Modelling of the Integral payload, Proceedings 2nd INTEGRAL workshop, ESA SP-382, 1997.

76. GEANT, Detector description and simulation tool, CERN, Geneva, Switzerland, 1993.

77. Private communication with Dr D Ramsden, Physics Department, Southampton University, UK.

78. Reedy, R.C., Arnold, J.R.; Interaction of Solar and Galactic Cosmic-ray Particles with the Moon, Journal of Geophysical Research, Vol. 77, No. 4, pp. 537-555, 1972.

79. Lawrence, D.J., et al.; Global Elemental Maps of the Moon: The Lunar Prospector Gamma-ray Spectrometer, Science, Vol. 281, pp. 1484-1489, 1998.

80. Shepp, L.A and Vardi, Y., IEEE Trans. Med Imag., MI-1, 113, 1982

81. Bouchet, L.; A comparative study of deconvolution methods for gamma-ray spectra, Astronomy and Astrophysics supplement series, Vol. 113, pp 167-183, 1995.

82. Daniell, G.J.; Image restoration and processing methods, Nuclear Instruments and Methods in Physics Research, Vol. 221, pp 67-71, 1984.

83. Press, W.H., et al.; Numerical Recipes, Cambridge University Press. ISBN 0-521-30811-9

84. Integrated Detectors and Electronics A/s, Veritasveien 9, N-1322, Hovik, Norway.

85. A.N.Sudarkin, O.P.Ivanov, V.E. Stepanov and L.I.Urutskoev, Conference Records of IEEE NSS/MIC'97, Albuquerque NM, November 1997.

86. A.V.Chesnokov, V.I.Fedin, A.P.Govorun et al, Appl. Radiat. Isot. Vol. 48, no. 9, pp.1265-1272, 1997.

87. A.N.Sudarkin, O.P.Ivanov, V.E.Stepanov, et al, IEEE Trans. Nucl. Sci., vol. 43, no. 4, pp. 2427-2433, August, 1996.

88. A.V.Chesnokov, S.M.Ignatov, V.N.Potapov, et al, NIM A 401 (1997) 414-420.

89. Hunter, S.; Remote geochemical analysis of planetary surfaces using gamma-rays, Masters thesis, Physics and Astronomy Department, University of Southampton, UK.

90. Gozani, T.; Nuclear based techniques for cargo inspection- A Review, Proceedings of the contraband and cargo inspection technology international symposium, - The White House Office of National Drug Control Policy, 1992, p9.

91. Vourvopoulos, G.; Techniques for detecting explosives and contraband, Chemistry and Industry , April 1994, p298.

92. A-711 Generator made by MF Physics Corp, 5074 List Drive, Colorado Springs 80919.

93. Hurwitz, M.J., et al; Detection of illicit drugs in cargo containers using pulsed fast neutron analysis, Proceedings of the contraband and cargo inspection technology international symposium, - The White House Office of National Drug Control Policy, 1992, p29.